A&A 493, 339–373 (2009)
DOI: 10.1051/0004-6361:200810534

Astronomy & Astrophysics

The XMM-Newton serendipitous survey⋆,⋆⋆

V. The Second XMM-Newton serendipitous source catalogue

M. G. Watson[1], A. C. Schröder[1], D. Fyfe[1], C. G. Page[1], G. Lamer[2], S. Mateos[1], J. Pye[1], M. Sakano[1], S. Rosen[1], J. Ballet[3], X. Barcons[4], D. Barret[5], T. Boller[6], H. Brunner[6], M. Brusa[6], A. Caccianiga[7], F. J. Carrera[4], M. Ceballos[4], R. Della Ceca[7], M. Denby[1], G. Denkinson[1], S. Dupuy[5], S. Farrell[5], F. Fraschetti[3], M. J. Freyberg[6], P. Guillout[9], V. Hambaryan[2,16], T. Maccacaro[15], B. Mathiesen[3], R. McMahon[8], L. Michel[9], C. Motch[9], J. P. Osborne[1], M. Page[10], M. W. Pakull[9], W. Pietsch[6], R. Saxton[11], A. Schwope[2], P. Severgnini[7], M. Simpson[1], G. Sironi[1,7], G. Stewart[1], I. M. Stewart[1,13], A.-M. Stobbart[1], J. Tedds[1], R. Warwick[1], N. Webb[5], R. West[1], D. Worrall[12], and W. Yuan[8,14]

[1] Department of Physics & Astronomy, University of Leicester, Leicester, LE1 7RH, UK
e-mail: mgw@star.le.ac.uk
[2] Astrophysikalisches Institut Potsdam (AIP), An der Sternwarte 16, 14482 Potsdam, Germany
[3] AIM, DSM/IRFU/SAp, CEA Saclay, 91191 Gif-sur-Yvette, France
[4] Instituto de Fisica de Cantabria (CSIC-UC), Avenida de los Castros, 39005 Santander, Spain
[5] CNRS, Université Paul Sabatier & Observatoire Midi-Pyrénées, 9 avenue du Colonel Roche, 31400 Toulouse, France
[6] Max-Planck-Institut für Extraterrestrische Physik, Giessenbachstraße 1, 85748 Garching, Germany
[7] INAF – Osservatorio Astronomico di Brera, via Brera 28, 20121 Milan, Italy
[8] Institute of Astronomy, Madingley Road, Cambridge CB3 0HA, UK
[9] Observatoire Astronomique, UMR 7550 CNRS, Université Louis Pasteur, 11 rue de l'Université, 67000 Strasbourg, France
[10] Mullard Space Science Laboratory, University College London, Holmbury St. Mary, Dorking, Surrey RH5 6NT, UK
[11] ESA/ESAC, Apartado 78, 28691 Villanueva de la Cañada, Madrid, Spain
[12] H.H. Wills Physics Laboratory, University of Bristol, Tyndall Avenue, Bristol BS8 1TL, UK
[13] Jodrell Bank Centre for Astrophysics, University of Manchester, Oxford Road, Manchester M13 9PL, UK
[14] National Astronomical Observatories of China/Yunnan Observatory, Phoenix Hill, PO Box 110, Kunming, Yunnan, PR China
[15] INAF – Headquarters, via del Parco Mellini 84, 00136 Rome, Italy
[16] Astrophysikalisches Institut und Universitäts-Sternwarte, Friedrich-Schiller-Universität Jena, Schillergässchen 3, 07745 Jena, Germany

Received 7 July 2008 / Accepted 14 October 2008

ABSTRACT

Aims. Pointed observations with XMM-Newton provide the basis for creating catalogues of X-ray sources detected serendipitously in each field. This paper describes the creation and characteristics of the 2XMM catalogue.
Methods. The 2XMM catalogue has been compiled from a new processing of the XMM-Newton EPIC camera data. The main features of the processing pipeline are described in detail.
Results. The catalogue, the largest ever made at X-ray wavelengths, contains 246 897 detections drawn from 3491 public XMM-Newton observations over a 7-year interval, which relate to 191 870 unique sources. The catalogue fields cover a sky area of more than 500 deg^2. The non-overlapping sky area is ~360 deg^2 (~1% of the sky) as many regions of the sky are observed more than once by XMM-Newton. The catalogue probes a large sky area at the flux limit where the bulk of the objects that contribute to the X-ray background lie and provides a major resource for generating large, well-defined X-ray selected source samples, studying the X-ray source population and identifying rare object types. The main characteristics of the catalogue are presented, including its photometric and astrometric properties

Key words. X-rays: general – catalogs – surveys

1. Introduction

Surveys play a key role in X-ray astronomy, as they do in other wavebands, providing the basic observational data for characterising the underlying source populations. *Serendipitous* X-ray sky surveys, based on the field data from individual pointed observations, take advantage of the relatively wide field of view afforded by typical X-ray instrumentation. Such surveys have been pursued with most X-ray astronomy satellites since the Einstein Observatory. The resulting serendipitous source catalogues (e.g., EMSS: Gioia et al. 1990; Stocke et al. 1991; WGACAT: White et al. 1994; ROSAT 2RXP: Voges et al. 1999; ROSAT 1RXH: ROSAT Team 2000; ASCA AMSS: Ueda et al. 2005) have been the basis for numerous studies and have made a significant contribution to our knowledge of the X-ray sky and our understanding of the nature of the various Galactic and extragalactic source populations.

⋆ Based on observations obtained with XMM-Newton, an ESA science mission with instruments and contributions directly funded by ESA Member States and NASA.
⋆⋆ The catalogue and full Tables D.1 and D.2 are available in electronic form at the CDS via anonymous ftp to cdsarc.u-strasbg.fr (130.79.128.5) or via http://cdsweb.u-strasbg.fr/cgi-bin/qcat?J/A+A/493/339

The XMM-Newton observatory provides unrivalled capabilities for serendipitous X-ray surveys by virtue of the large field of view of the EPIC cameras and the high throughput afforded by the heavily nested telescope modules. This capability guarantees that each XMM-Newton observation provides a significant harvest of serendipitous X-ray sources in addition to data on the original target. In addition, the extended energy range of XMM-Newton (~0.2−12 keV) means that XMM-Newton detects significant numbers of obscured and hard-spectrum objects that are absent in many earlier soft X-ray surveys.

This paper describes the Second XMM-Newton Serendipitous Source Catalogue (2XMM) which has been created from the serendipitous EPIC data from from 3491 XMM-Newton pointed observations made over a ~7-year interval since launch in 1999. The XMM-Newton serendipitous source catalogues are produced by the XMM-Newton Survey Science Centre (SSC), an international consortium of ten European institutions, led by the University of Leicester, as a formal project activity performed on behalf of ESA. The catalogues are based on the EPIC source lists produced by the scientific pipe-line used by the SSC for the processing of all the XMM-Newton data. The first serendipitous source catalogue, 1XMM, was released in 2003 (Watson et al. 2003; XMM-SSC 2003). The current 2XMM catalogue incorporates a wide range of improvements to the data processing, uses the most up-to-date instrument calibrations and includes a large number of new parameters. In parallel, the 2XMM catalogue processing also produces a number of additional data products, for example time-series and spectra for the brighter individual X-ray sources. A pre-release version of the current catalogue, 2XMMp (XMM-SSC 2006), was made public in 2006. This included ~65% of the fields and ~75% of the sky area covered by 2XMM, while ~88% of all 2XMMp sources appear in the 2XMM catalogue. Around 56% of all 2XMM sources already have an entry in the 2XMMp catalogue.

The 2XMM catalogue provides an unsurpassed sky area for serendipitous science and reaches a flux limit corresponding to the dominant extragalactic source contribution to the cosmic X-ray background. The catalogue is part of a wider project to explore the source populations in the XMM-Newton serendipitous survey (the XID project; Watson et al. 2001, 2003) through optical identification of well-defined samples of serendipitous sources (e.g., Barcons et al. 2002, 2007; Della Ceca et al. 2004; Caccianiga et al. 2008; Motch et al. 2002; Schwope et al. 2004; Page et al. 2007; Yuan et al. 2003; Dietrich et al. 2006). Indeed these identification programs were effectively based on less mature versions of the XMM-Newton catalogue data processing. XMM-Newton serendipitous survey results have also been used to study various statistical properties of the populations such as X-ray spectral characteristics, source counts, angular clustering, and luminosity functions (Severgnini et al. 2003; Mateos et al. 2005; Carrera et al. 2007; Caccianiga et al. 2007; Mateos et al. 2008; Della Ceca et al. 2008; Ebrero et al. 2008). Other projects based on XMM-Newton serendipitous data include the HELLAS2XMM survey (Baldi et al. 2002; Cocchia et al. 2007).

The 2XMM serendipitous catalogue described here is complementary to "planned" XMM-Newton surveys which provide coverage of much smaller sky areas, but often with higher sensitivity, thus exploring the fainter end of the X-ray source population. The deepest such surveys, such as the Lockman Hole (Hasinger et al. 2001; Brunner et al. 2008) and the CDF-S (Streblyanska et al. 2004), cover essentially only a single XMM-Newton field of view, have total integration times ~300−1000 ks and reach fluxes ~few $\times 10^{-16}$ erg cm^{-2} s^{-1}, close to the confusion limit. XMM-Newton has also carried out contiguous surveys of various depths covering much larger sky areas utilising mosaics of overlapping pointed observations to achieve the required sensitivity and sky coverage. Currently the largest contiguous XMM-Newton survey is the XMM-LSS (Pierre et al. 2007) covering ~5 deg^2 with typical exposure time 10−20 ks per observation. Other medium-deep surveys of 1−2 deg^2 regions include the SXDS (~1.1 deg^2, 50−100 ks exposures; Ueda et al. 2008), the COSMOS surveys (~2 deg^2, ~80 ks exposures; e.g., Cappelluti et al. 2007; Hasinger et al. 2007), and the Marano field survey (Krumpe et al. 2007). These larger area surveys typically reach limiting fluxes of 10^{-14} to $<10^{-15}$ erg cm^{-2} s^{-1}.

We also note that Chandra observations have been used to compile a serendipitous catalogue including ~7000 point sources (the ChaMP catalogue; Kim et al. 2007) and plans are underway to compile a serendipitous catalogue from all suitable Chandra observations (Fabbiano et al. 2007).

The paper is organised as follows. Section 2 introduces the XMM-Newton observatory. Section 3 presents the XMM-Newton observations used to create the catalogue and the characteristics of the fields. Section 4 outlines the XMM-Newton data processing framework and provides a more detailed account of the EPIC data processing, focusing in particular on source detection and parameterisation, astrometric corrections and flux computation. Section 5 provides an account of the automatic extraction of time-series and spectra for the brighter sources, while Sect. 6 outlines the external catalogue cross-correlation undertaken. Section 7 describes the quality evaluation undertaken and some recommendations on how to extract useful sub-samples from the catalogue. Section 8 describes additional processing and other steps taken to compile the catalogue including the identification of unique sources. The main properties and characterisation of the catalogue is presented in Sect. 9. Section 10 summarises access to the catalogue and plans for future updates to 2XMM, and Sect. 11 gives a summary.

2. XMM-Newton observatory

To provide the essential context for this paper, the main features of the XMM-Newton observatory are summarised here, with particular emphasis on the EPIC X-ray cameras from which the catalogue is derived.

The XMM-Newton observatory (Jansen et al. 2001), launched in December 1999, carries three co-aligned grazing-incidence X-ray telescopes, each comprising 58 nested Wolter-I mirror shells with a focal length of 7.5 m. One of these telescopes focuses X-rays directly on to an EPIC (European Photon Imaging Camera) pn CCD imaging camera (Strüder et al. 2001). The other two feed two EPIC MOS CCD imaging cameras (Turner et al. 2001) but in these telescopes about half the X-rays are diverted, by reflection grating arrays (RGA), to the reflection grating spectrometers (RGS; den Herder et al. 2001) which provide high resolution ($\lambda/\Delta\lambda \approx 100-800$) X-ray spectroscopy in the 0.33−2.5 keV range. The EPIC cameras acquire data in the 0.1−15 keV range with a field of view (FOV) ~30 arcmin diameter and an on-axis spatial resolution ~5 arcsec *FWHM* (MOS being slightly better than pn). The physical pixel sizes for the pn and MOS cameras is equivalent to ~1 and ~4 arcsec, respectively. The on-axis effective area for the pn camera is approximately 1400 cm^2 at 1.5 keV and 600 cm^2 at 8 keV while corresponding MOS effective areas are about 550 cm^2 and 100 cm^2, respectively. The energy resolution for the pn camera is ~120 eV at 1.5 keV and ~160 eV at 6 keV (*FWHM*), while for the MOS camera it is ~90 eV and ~135 eV, respectively.

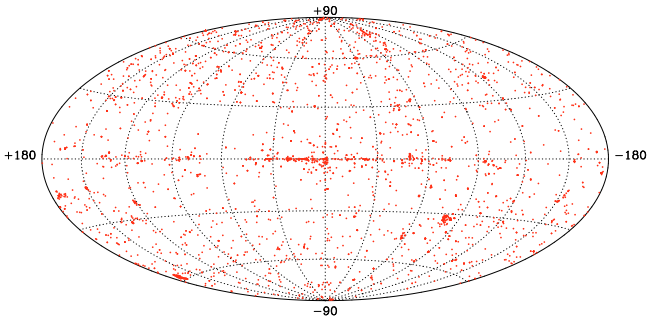

Fig. 1. Hammer-Aitoff equal area projection in Galactic coordinates of the 3491 2XMM fields.

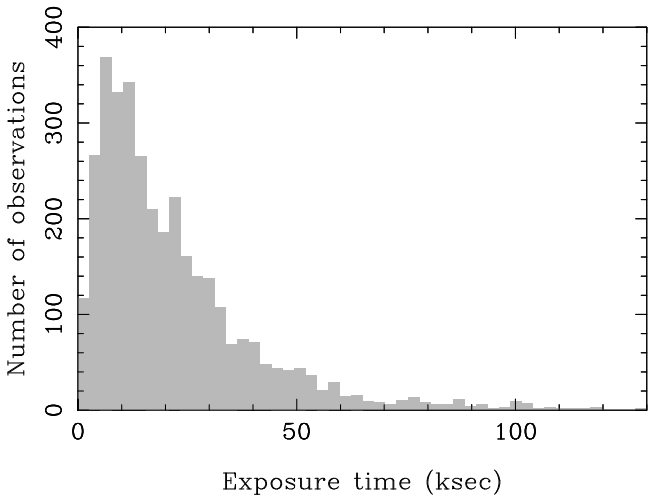

Fig. 2. Distribution of total good exposure time (after event filtering) for the observations included in the 2XMM catalogue (for each observation the maximum time of all three cameras per observation was used).

The EPIC cameras can be used in a variety of different modes and with several filters (see Sect. 3.1). In addition to the X-ray telescopes, XMM-Newton carries a co-aligned, 30 cm diameter Optical Monitor (OM) telescope (Mason et al. 2001) which provides an imaging capability in three broad-band ultra-violet filters and three optical filters, spanning 1800 Å to 6000 Å; two additional grism filters permit low dispersion ultra-violet and optical-band spectroscopy. The construction of a separate catalogue of OM sources is in preparation.

A number of specific features of XMM-Newton and the EPIC cameras which are referred to repeatedly in this paper are collected together and summarised in Appendix A together with the relevant nomenclature.

3. Catalogue observations

3.1. Data selection

XMM-Newton observations[1] were selected for inclusion in the 2XMM catalogue pipeline simply on the basis of their public availability and their suitability for serendipitous science. In practice this meant that all observations that had a public release date prior to 2007 May 01 were eligible. A total of 3491 XMM-Newton observations (listed in Appendix B) were included in the catalogue; their sky distribution is shown in Fig. 1. Only a few observations (83) were omitted, typically because a valid ODF[2] was not available or because of a few unresolved processing problems. The field of view (FOV) of an XMM-Newton observation (the three EPIC cameras combined) has a radius ∼15 arcmin. The XMM-Newton observations selected for the 2XMM catalogue cover only ∼1% of the sky (see Sect. 9.2 for a more detailed discussion). Certain sky regions have contiguous multi-FOV spatial coverage, but the largest such region is currently <10 deg^2.

By definition the catalogue observations do not form a homogeneous set of data. The observations selected have, for example, a wide sky distribution (see Fig. 1, where ∼65% are at Galactic latitude $|b| > 20°$), a broad range of integration times (Fig. 2) and astrophysical content (Sect. 3.2), as well as a mixture of EPIC observing modes and filters, as follows.

The EPIC cameras are operated in several modes of data acquisition. In full-frame and extended full-frame modes the full detector area is exposed, while for the EPIC pn large window mode only half of the detector is read out. A single CCD is used for small window, timing and burst mode (not used for source detection). In the case of MOS the outer ring of 6 CCDs *always* remain in standard imaging mode while the central MOS CCD can be operated separately: in partial window modes only part of the central CCD is read out, and in fast uncompressed and compressed modes the central CCD is in timing mode and produces no imaging data. In the MOS refreshed frame store mode the central CCD has a different frame time and the CCD is not used for source detection. Table 1 lists all the EPIC camera modes of observations incorporated in the catalogue, while Fig. 3 shows their sky footprints.

Table 1. Data modes of XMM-Newton exposures included in the 2XMM catalogue.

Abbr.	Designation	Description
MOS cameras:		
PFW	Prime Full Window	covering full FOV
PPW2	Prime Partial W2	small central window
PPW3	Prime Partial W3	large central window
PPW4	Prime Partial W4	small central window
PPW5	Prime Partial W5	large central window
FU	Fast Uncompressed	central CCD in timing mode
RFS	Prime Partial RFS	central CCD with different frame time ("Refreshed Frame Store")
pn camera:		
PFWE	Prime Full Window Extended	covering full FOV
PFW	Prime Full Window	covering full FOV
PLW	Prime Large Window	half the height of PFW/PFWE

Each XMM-Newton camera can be used with a different filter: Thick, Medium, Thin, and Open, the choice depending on the degree of optical blocking[3] desired. Table 2 gives an overview of the data modes and filter settings used for the 2XMM observations. No Open filter exposures passed the selection criteria (cf. Sect. 4.1), while about 20% of pn observations are taken in timing, burst, or small window mode.

[1] An observation is defined as a single science pointing at a fixed celestial target which may consist of several exposures with the XMM-Newton instruments.

[2] The Observation Data File is a collection of standard FITS format raw data files created from the satellite telemetry.

[3] See Appendix A.

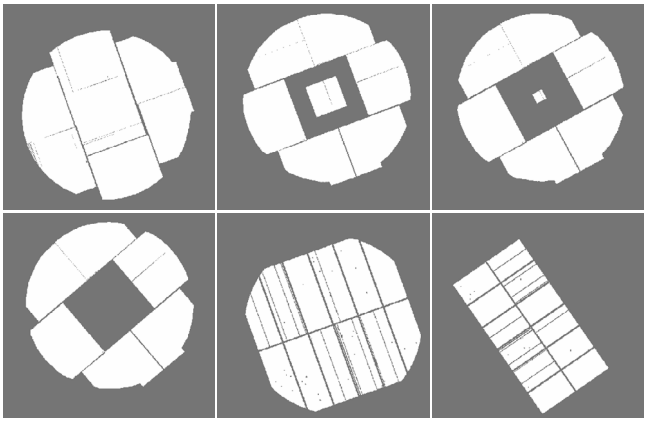

Fig. 3. Typical sky footprints of the different observing modes (the FOV is ~30′). Noticeable are the CCD gaps as well as columns and rows excluded in the filtering process. *Top row*: MOS full window mode; MOS partial window W3 or W5 mode; MOS partial window W2 or W4 mode. *Bottom row*: MOS fast uncompressed, fast compressed, or RFS mode; pn full window mode; pn large window mode.

Table 2. Characteristics of the 3491 XMM-Newton observations included in the 2XMM catalogue.

Camera	Modes			Filters			Total
	full[a]	window[b]	other[c]	thin	medium	thick	
pn	2441	233	–	1233	1259	182	2674
MOS1	2560	605	219	1314	1772	298	3384
MOS2	2612	655	127	1314	1777	303	3394

[a] PFWE and PFW modes; [b] pn PLW mode and any of the various MOS PPW modes; [c] other MOS modes (FU, RFS).

3.2. Target classification and field characteristics

The 2XMM catalogue is intended to be a catalogue of serendipitous sources. The observations from which it has been compiled, however, are pointed observations which typically contain one or more target objects chosen by the original observers, so the catalogue contains a small fraction of targets which are by definition not serendipitous. More generally, the fields from which the 2XMM catalogue is compiled may also not be representative of the overall X-ray sky.

To avoid potential selection bias in the use of the catalogue, an analysis to identify the target or targets of each XMM-Newton observation has been carried out. Additionally, an attempt has been made to classify each target or the nature of the field observed; this provides additional information which can be important in characterising their usefulness (or otherwise) for serendipitous science. In practice the task of identifying and classifying the observation target is to some extent subjective and likely to be incomplete (only the investigators of that observation know all the details). Here, the main results of the exercise are summarised. A more detailed description is given in Appendix C.

- Of the total 3491 observations included in 2XMM, the target could be unambiguously resolved in terms of its coordinates and classification in the vast majority of cases (~98%);
- in the full set of targets, ~50% are classified as spatially unresolved objects, ~10% as extended objects with small angular extent (<3′), ~22% as larger extended objects, and around 15% can be considered to have no discrete target leaving only ~2% of unknown or problematic cases (see Table C.1);
- around 10% of observations were obtained for calibration purposes; around 3% of targets are "targets of opportunity";
- anticipating the discussion in Sect. 9.1, around 2/3 of the intended targets are unambiguously identified in their XMM-Newton observations.

Figure 4 illustrates the wide variety in field content (images are usually combinations of pn and MOS total-band images that include out-of-FOV areas). Panel (a) shows typical XMM-Newton observations which may be considered representative of most of the observations used for the catalogue. Panel (b) shows the variety of astrophysical content; in many of these cases the source detection is affected by a dominant bright point or extended source, or by crowding in high density regions. Lastly panel (c) illustrates various instrumental or detector artefacts which, although relatively rare, cause significant source detection issues. The most common of these, affecting ~6% of the observations each, are the OOT events and X-ray scattering off the RGA (see Appendix A for terminology). Both effects occur for all sources but only become significant for the brightest objects where they may cause spurious detections and background subtraction problems (as OOT events of piled-up sources are not represented properly in the background maps). The rarer problems (also illustrated in panel (c)) are:

- pileup[4], which can make the centroiding of a source difficult, resulting in off-centre detections as well as spurious extended source detection;
- the shadows from the mirror spider can be visible in the PSF[4] wings of the very brightest sources and affect the background maps, that is, the source parameters in these areas are uncertain;
- due to the nature of the background maps (spline maps, see Sect. 4.4.2), sharp edges, caused, for example, by noisy CCDs, can not be represented well and cause spurious detections. Note that this problem can affect the parameters of real sources as well;
- finally, the telescope baffles allow photons from a narrow annular region of sky outside the nominal FOV to reach the detectors via a single reflection, instead of the two reflections required for correct focusing. Bright X-ray objects in this annular region can give rise to bright arcs in the image, as shown in panel (v), which typically produce numerous spurious detections.

4. Data processing

The SSC operates a data-processing system on behalf of ESA for the processing of XMM-Newton pointed observations. The system, which can be considered as a "pipeline", uses the XMM-Newton Science Analysis Software (SAS[5]) to generate high-level science products from ODFs. These science products are made available to the principal investigator and ultimately the astronomy community through the XMM Science Archive (XSA; Arviset et al. 2007). In October 2006, the SSC began to reprocess every available pointed-observation data-set from the start of the mission. The aim was to create a uniform set of science products using an up-to-date SAS and a constant set of XMM-Newton calibration files[6] (the appropriate subset of

[4] See Appendix A.

[5] The description and documentation are available on-line at the ESAC web site http://xmm2.esac.esa.int/sas/

[6] As available on 2006 July 02 plus three additional calibration files for MOS2 and RGS1.

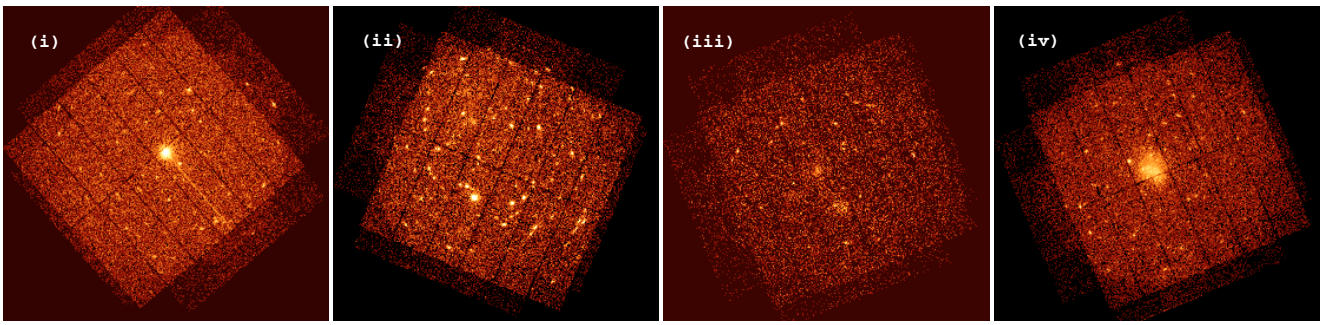

Fig. 4. a) Examples of typical 2XMM EPIC images (north is up). *From left to right*: (i) medium bright point source; (ii) deep field observation; (iii) shallow field observation with small extended sources; (iv) distant galaxy cluster.

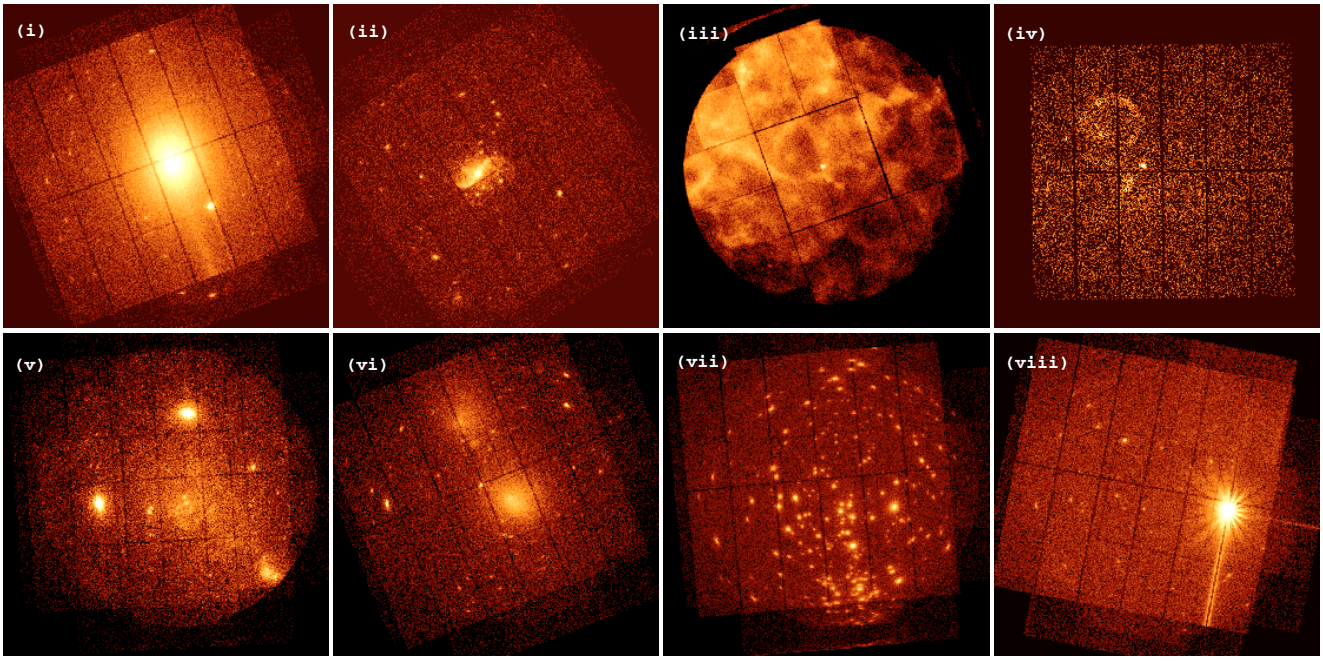

Fig. 4. b) Examples of variation in astrophysical content of 2XMM observations (*north is up*); in most of these extreme cases the source detection is problematic. *Top row, from left to right*: (i) bright extended emission from a galaxy cluster; (ii) emission from a spiral galaxy which includes point sources and extended emission; (iii) very bright extended emission from a SNR; (iv) filamentary diffuse emission. *Second row*: (v) complex field near the Galactic Centre with diffuse and compact extended emission; (vi) two medium-sized galaxy clusters; (vii) complex field of a star cluster; (viii) bright point source, off-centre.

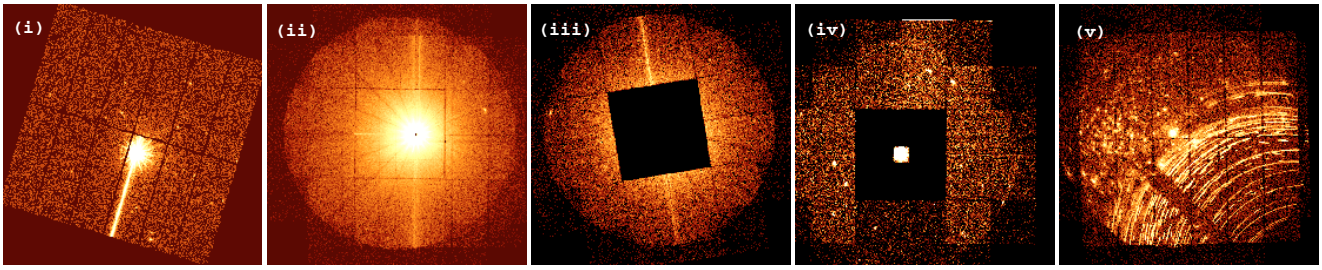

Fig. 4. c) Examples of instrumental artefacts causing spurious source detection (*north is up*). *From left to right*: (i) bright source with pileup and OOT events; (ii) very bright point source showing obvious pileup, shadows from the mirror spider, and scattered light from the RGA; (iii) the PSF wings of a bright source spread beyond the unused central CCD causing a brightening of the edges on the surrounding CCDs (which may not be well represented in the background map); (iv) obvious noisy CCDs for MOS1 (CCD#4) and for MOS2 (CCD#5) *to the top right*; (v) numerous and bright single reflections from a bright point source outside the FOV, with a star cluster *to the left*. See Appendix A for terminology.

calibration files for any given observation was selected based on the observation date). Of 5628 available observations, 5484 were successfully processed. These included public as well as (at that time) proprietary datasets (the data selection for 2XMM observations is discussed in Sect. 3.1). The complete results of the processing have been made available through the XSA. The new system incorporated significant processing improvements in terms of the quality and number of products, as described below. The remainder of this section details those aspects of the

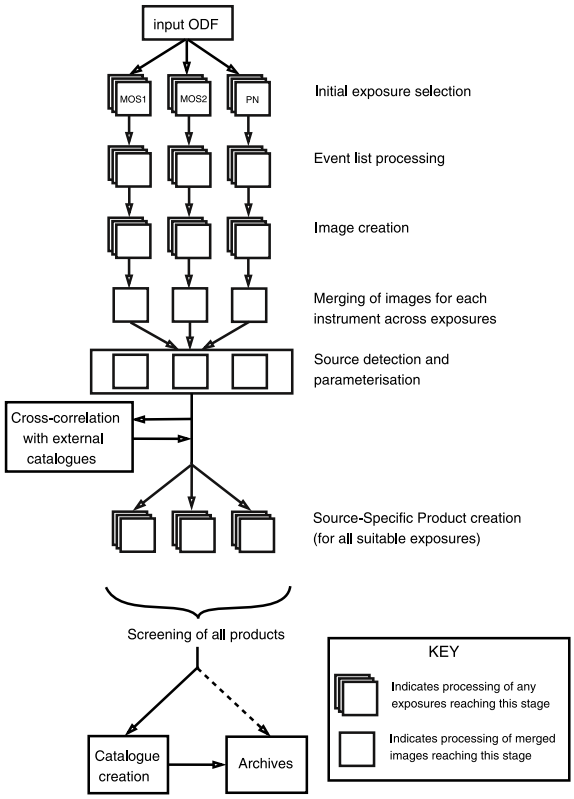

Fig. 5. A simplified schematic of the processing flow for EPIC image data. Early processing steps treat the data from each instrument and exposure separately. Source detection and parameterisation are performed simultaneously on one image from each energy band from each instrument. Source-specific products can be made, subsequently, from any suitable exposures in the observation. Observation-level, exposure-level and source-specific products are screened before archiving and use in making the catalogue.

EPIC processing system which are pertinent to the creation of the 2XMM catalogue.

The main steps in the data-processing sequence are: production of calibrated detector events from the ODF science frames; identification of the appropriate low-background time intervals using a threshold optimised for point-source detection; identification of "useful" exposures (taking account of exposure time, instrument mode, etc.); generation of multi-energy-band X-ray images and exposure maps from the calibrated events; source detection and parameterisation; cross-correlation of the source list with a variety of archival catalogues, image databases and other archival resources; creation of binned data products; application of automatic and visual screening procedures to check for any problems in the data products. This description and the schematic flowchart in Fig. 5 provide a rather simplified view of the actual data-processing system. They, and the further detail that follows, are focused on those aspects that are important for an insight into the analysis processes that the EPIC data have undergone to generate the data products. A complete description of the data-processing system and its implementation are outside the scope of this paper.

The criteria employed to select exposures for initial processing and those to be used for subsequent source detection and source-product generation are explained further in Sect. 4.1 but are briefly introduced here. Several suitability tests were applied during processing to limit source detection and source-specific product creation to imaging exposures of suitable quality, mainly by (a) restricting the merging of exposures (and hence source detection) to imaging exposures with a minimum of good-quality exposure time, and (b) limiting the extraction of source-specific products to suitably bright sources.

4.1. Selection of exposures

Most XMM-Newton observations comprise a single exposure with each of the cameras, although a significant number of observations are missing exposures in one or more of the three cameras for a variety of operational and observational reasons. To avoid generating data products of little or no scientific use, exposures for each observation were initially selected for pipeline processing when:

1. the exposure duration was >1000 s;
2. the exposure was taken through a scientifically useful filter. In practice this requirement rejected all exposures for which the filter position was closed, calibration, or undefined. The possible filters are Medium, Thick, Thin1, Thin2 (pn only), and Open.

After event-list processing (Sect. 4.3), exposures were selected for image creation according to the following criteria:

3. the quality checks during the event-list processing had been successful;
4. the exposure had been taken in a mode which could usefully be processed by the source detection stage, cf. Table 1. The pn burst, timing, and small window modes were rejected (the effective FOV in the latter mode is small, i.e., $258'' \times 262''$, making the background fitting stage of the source detection problematic). For the MOS, all modes, including the outer CCD imaging component of modes where the central CCD was windowed, missing (non-imaging modes), or modified (Refreshed Frame Store mode), were included.

A further set of criteria selected the appropriate images for the detection stage (cf. Sect. 4.4) which ensured that only high quality images were used:

5. background filtering (see Sect. 4.3) must have been successfully applied. Cases where the sum of high background GTIs[7] was less than 1000 s were rejected as unusable. Without background filtering the source detection is usually of limited value due to the much higher net background;
6. each of the five images of an exposure (in the energy bands 1−5, see Table 3) had to contain at least one pixel per image with more than one event. This further avoided low exposure images being used;
7. the image must have been in a data mode useful for source detection (this excluded modes only used for engineering test purposes);
8. where more than one exposure with a particular camera passed the above selection criteria, those exposures with the same filter and data mode were merged and then only the exposure group with the maximum net exposure time was chosen for use in the source detection stage.

4.2. Event-list processing

Event-list processing was performed on all initially selected exposures. A number of checks and corrections were applied to the

[7] see Appendix A.

Table 3. Energy bands used in 2XMM processing.

Band number	Energy band (keV)	Notes
1	0.2–0.5	
2	0.5–1.0	
3	1.0–2.0	
4	2.0–4.5	
5	4.5–12.0	
6	0.5–2.0	"soft band"
7	2.0–12.0	"hard band"
8	0.2–12.0	"total band"
9	0.5–4.5	"XID band"

event lists of the individual CCDs before they were merged into a single event list per exposure. Once merged, a further set of checks and corrections was performed. At each stage of the processing, a quality assessment of the event lists decided whether to continue the processing. The main steps in processing the event lists were as follows.

- The CCD event lists were first examined separately on a frame by frame basis: corrections were applied to account for telemetry dropouts; gain and charge transfer inefficiency (CTI) corrections were made; a GTI list for each CCD was created; frames identified as bad and events belonging to them were flagged; event patterns[8] were identified; events were flagged if they met criteria such as being close to a bad pixel or edge of the CCD, which were important to later processing (standard #XMMEA_EM for MOS and #XMMEA_EP for pn); invalid events were identified and discarded; events caused by CCD bad pixels were identified and removed; the fraction of the detector area in which events could not have been detected due to cosmic-ray events was recorded for each frame; events caused by CCD bad pixels as well as cosmic-ray events were identified and removed; EPIC MOS CCDs operating in low-gain mode were discarded from the event lists.
- At the point where the event lists from individual CCDs were merged into exposure event lists, the event positions were converted from CCD pixel coordinates to the detector (`CAMCOORD2`) and sky coordinate systems. This step includes a randomisation within each CCD pixel to eliminate Moiré effects. The MOS camera event times were also randomised within the frame time, to avoid a strong Fourier peak at the frame period and to avoid possible beat effects with other instrumental frequencies. Time randomisation was not performed on pn event lists as the frame time is much shorter than for the MOS.

In addition, the spacecraft attitude file was examined for periods of the observation when the spacecraft pointing direction varied by less than 3 arcmin from the median of the pointing measurements for the observation. The 3-arcmin limit was imposed to avoid degradation of the effective PSF [9] which could arise from co-adding data with different off-axis angles and to avoid a potentially large (but probably low exposure) extension of the observed sky field. These attitude GTIs were then further restricted for each camera to cover only that part of the observation when the camera was active.

[8] See Appendix A.
[9] See Appendix A.

4.3. Creation of multi-band images and exposure maps

Periods of high background (mostly due to so-called "soft proton" flares) can significantly reduce the sensitivity of source detection. Since events caused by such flares are usually much harder than events arising from typical X-ray sources, background variation can be disentangled from possible time variation of the sources in the field by monitoring events at energies higher than the 12 keV upper boundary to the "science band", beyond which point contributions from cosmic X-ray sources are rarely significant. A time series of such events, including most of the FOV, was constructed for each exposure. This event rate was used as a proxy for the science-band background rate.

The generation of the background time-series differed in detail between pn and MOS cameras, in particular in terms of the events used to form the time-series. The MOS high-energy background time-series were produced from single-pixel events with energies above 14 keV from the imaging CCDs. The background GTIs were taken to be those time intervals of more than 100 s in duration with a count rate of less than 2 ct ks^{-1} $arcmin^{-2}$. The pn high-energy background time-series were produced in the 7.0−15 keV energy range. The background GTIs were taken to be those time intervals of more than 100 s in duration with a count rate of less than 10 ct ks^{-1} $arcmin^{-2}$.

These threshold count rates were chosen as a good compromise between reducing background and preserving exposure for detecting point sources in the relatively short exposures which make up the bulk of the XMM-Newton observations. For comparison, the average quiet level in the MOS cameras, for example, is ∼0.5 ct ks^{-1} $arcmin^{-2}$.

For all exposures in imaging mode, images were created for energy bands 1−5, as listed in Table 3, from selected events filtered by event-list, attitude, and high background GTIs (except where the sum of all high background GTIs was less than 1000 s in which case no background filtering was applied). Note that the event-list GTIs are CCD dependent and the resulting image can have a different exposure time in each CCD. The events for pn images were selected by pattern ≤ 4 (for band 1 a stricter requirement of pattern = 0 was adopted) and a cut in CCD coordinates ($Y > 12$) to reduce bright low-energy edges. Events on CCD columns suffering a particularly large energy scale offset as well as events outside the FOV were excluded. For MOS images events with pattern ≤12 were selected and events outside the FOV were excluded. The images are tangent-plane projections of celestial coordinates and have dimensions of 648 × 648 image pixels, with a pixel size of 4″ × 4″.

Exposure maps represent the GTI-filtered on-time multiplied by the (spatially dependent) vignetting function, adjusted to reflect telescope and instrumental throughput efficiency. They were created for each EPIC exposure in imaging mode in energy bands 1−5 using the calibration information on mirror vignetting, detector quantum efficiency, and filter transmission. The exposure maps were corrected for bad pixels, bad columns and CCD gaps (cf. Fig. 3) as well as being multiplied by an OOT factor which is 0.9411 for pn full frame modes, 0.97815 for pn extended full frame modes, and 1.0 for all other pn and MOS modes.

4.4. Source detection and parameterisation

The fundamental inputs to the 2XMM catalogue are the measured source parameters which were extracted from the EPIC image data by the multi-step source detection procedure outlined below. Each step was carried out simultaneously on each image

of the five individual bands, 1−5, and of the three cameras. Note that the source counts and rates derived here refer to the fully integrated PSF.

As a first step, a detection mask was made for each camera. This defines the area of the detector which is suitable for source detection. Only those CCDs where the unvignetted exposure map values were at least 50% of the maximum exposure map value were used for source detection.

4.4.1. Sliding-box source detection – local mode

An initial source list was made using a "box detection" algorithm. This slides a search box ($20'' \times 20''$) across the image defined by the detection mask. The size of the box comprises ~50% of the encircled energy fraction of the on-axis[10] PSF. In its first application ("local mode") the algorithm derived a local background from a frame ($8''$ wide) immediately surrounding the search box. In each of the five bands from each of the three cameras, the probability, $P_\Gamma(k, x)$, and corresponding likelihood, L_i, were computed from the null hypothesis that the measured counts k or more in the search box result from a Poissonian fluctuation in the estimated background level, x, i.e.:

$$L = -\ln P_\Gamma(k, x),$$

where P_Γ is the incomplete Gamma function:

$$P_\Gamma(k, x) = \frac{1}{\Gamma(k)} \int_0^x \mathrm{e}^{-t} t^{k-1} \mathrm{d}t,$$

and

$$\Gamma(k) = \int_0^\infty \mathrm{e}^{-t} t^{k-1} \mathrm{d}t.$$

The sum of N independent likelihoods, after multiplication by 2, is expected to have, in the limit of large N, the same probability distribution as χ^2 for N degrees of freedom (Cash 1979). For this reason the total-band EPIC box-detect likelihood was calculated by summing the band-specific likelihoods in this way and inserting the result in the standard formula for the probability for χ^2 to equal or exceed the measured value in the null hypothesis, i.e.,

$$L \approx -\ln(1 - P_\Gamma(N, L')) \quad \text{with} \quad L' = \sum_{i=1}^{N} L_i, \tag{1}$$

where N is the number of energy bands and cameras involved. All sources with a total-band EPIC likelihood above 5 were included in the output list.

4.4.2. Sliding-box source detection – map mode

After the first pass to detect sources, a background map was created for each camera and energy band. Using a cut-out radius dependent on source brightness in each band (specifically the radius where the source counts per unit area fell below 0.002 ct arcsec^{-2}), areas of the image where sources had been detected were blanked out. A 12×12-node spline surface was fitted to the resulting source-free image to calculate a smoothed background map for the entire image. For the pn images the contribution of OOT events was also modelled into the background maps.

[10] The encircled energy fraction does not strongly depend on off-axis angle.

A second box-source-detection pass was carried out, creating a new source list, this time using the spline background maps ("map mode") which increased the source detection sensitivity compared to the local-mode detection step. The box size was again set to $20'' \times 20''$. Source counts were corrected for the part of the PSF falling outside the detection box. Only sources with a total-band EPIC likelihood, cf. Eq. (1), above 5 were included in this map-mode source list.

4.4.3. Source parameter estimation by maximum likelihood fitting

A maximum likelihood fitting procedure was then applied to the sources emerging from the map-mode detection stage to calculate source parameters in each input image. This was accomplished by fitting a model to the distribution of counts over a circular area of radius $60''$. The energy-dependent model value, e_i, in pixel, i, is given by

$$e_i = b_i + \alpha S_i \tag{2}$$

where b_i is the background, derived from the background map, S_i is the source profile (i.e. the PSF, convolved with the source extent model (Sect. 4.4.4)) and α is a scalar multiplier of the source profile.

For each source, the fitting procedure minimised the C-statistic (Cash 1979)

$$C = 2 \sum_{i=1}^{N} (e_i - n_i \ln e_i)$$

to find the best set of model parameters, where e_i is the expected model value in pixel i (Eq. (2)), n_i the measured number of counts in pixel i, and N is the total number of pixels over all images used.

Free parameters of the fit were source position, extent, and source count rate. Positions and extent were constrained to be the same in all energy bands and for all cameras while the count rates were fitted separately for each camera and energy band. The fitting process used the multi-band exposure maps to take account of various instrumental effects (cf. Sect. 4.3) in deriving the source counts c_s:

$$c_\mathrm{s}(x, y) = R_\mathrm{s}(x, y)\, t_\mathrm{map}(x, y),$$

where $R_\mathrm{s}(x, y)$ is the source count rate in each image pixel as predicted by the instrumental PSF and source extent model and $t_\mathrm{map}(x, y)$ is the corresponding value of the exposure map.

After arriving at those values of the source parameters which minimize C, the detection likelihood (formally, the probability of the null hypothesis) for those optimum values is then calculated. Cash's prescription for this is to form the difference

$$\Delta C = C_\mathrm{null} - C_\mathrm{best},$$

where C_null is the C-statistic of the null hypothesis model (i.e., with zero source flux) and C_best is the minimum result returned by the fitting routine. According to Cash, ΔC is distributed approximately as χ^2 for ν degrees of freedom, where ν is the number of fitted parameters. The probability $P(\chi^2 \geq \Delta C)$ of obtaining the calculated value of ΔC or greater by chance fluctuations of the detected background can therefore be obtained in terms of the incomplete Gamma function P_Γ as follows:

$$P(\chi^2 \geq \Delta C) = 1 - P_\Gamma\left(\frac{\nu}{2}, \frac{\Delta C}{2}\right).$$

Note that the values L which are stored in the source lists are log-likelihoods, formed from $L = -\ln(P)$[11].

Since the C values are simple sums over all image pixels included in the fit, one may calculate ΔC_i for each band i then add the results together to generate a total-band $\Delta C_{\rm total}$ without destroying the χ^2 equivalence: only the number of degrees of freedom changes. The source detection procedure thus calculates ΔC_i and hence L_i for each ith band, using $\nu = 3$ (=4 if source extent is also fitted), then sums the ΔC_i and calculates $L_{\rm total}$ using $\nu = N + 2$ $(= N + 3)$, where N is the number of bands.

The fitting of the input sources was performed in the order of descending box(map)-detect detection likelihood. After each fit the resulting source model was added to an internally maintained background map used for the fitting of subsequent sources. With this method the background caused by the PSF wings of brighter sources is taken into account when fitting the fainter sources. All sources (as detected by the sliding-box in map mode) with a total-band detection likelihood >6, as determined by the fitting process, were included in the output source list. Note that for individual cameras and energy bands, the fitted likelihood values can be as low as zero.

The calculation of the parameter errors made use of the fact that ΔC follows the χ^2-distribution. The 68% confidence intervals were determined by fixing the model to the best-fit parameters and then subsequently stepping one parameter at a time in both directions until $C = C_{\rm best} + 1$ is reached (while the other free parameters were kept fixed). The upper and lower bound errors were then averaged to define a symmetric error. Note that using $C_{\rm best} + 1$ to determine the 68% confidence intervals is only strictly correct in the case that there is one parameter of interest. In the case of the fitting performed here, this requires that the position and amplitude parameters are essentially independent (i.e. that the cross-correlation terms of the error matrix are negligible). This has been found through simulations to be an acceptable approximation in the present case (see also the discussion of the astrometric corrections in Sect. 4.5).

Four camera-specific X-ray colours, known as hardness ratios (HR1-HR4), were obtained for each camera by combining corrected count rates from energy bands n and $n + 1$:

$$\mathrm{HR}n = (R_{n+1} - R_n)/(R_{n+1} + R_n)$$

where R_n and R_{n+1} are the corrected count rates in energy bands n and $n + 1$ $(n = 1{-}4)$. Count rates, and therefore hardness ratios, are camera dependent. In addition, they depend on the filter used for the observation, especially for HR1. Note that HR1 is also a strong function of Galactic absorption, $N_{\rm H}$. This needs to be taken into account when comparing hardness ratios for different sources and cameras. It should be stressed that a large fraction of the hardness ratios were calculated from marginal or non-detections in at least one of the energy bands. Consequently, individual hardness ratios should only be deemed reliable if the source is detected in both energy bands, otherwise they have to be treated as upper or lower limits. Similarly, the errors on the hardness ratios will be affected for band-limited count rates in the Poisson regime (Park et al. 2006).

[11] Protassov et al. (2002) have highlighted the dangers of using the probabilities derived from likelihood ratio tests when the null hypothesis is close to the boundary of parameter space. In this regard it is clear that it is inappropriate to interpret the detection likelihoods, L, literally in terms of detection probabilities. Instead the relation between the likelihood and the detection probability requires calibration via simulations, as is discussed in Sect. 9.4.

4.4.4. Extended-source parameterisation

One of the enhancements incorporated in the 2XMM processing that was not available in 1XMM was information about the potential spatial extent of sources and, where detected, a measure of that extent.

The source extent characterisation was realised by fitting a convolution of the instrumental PSF and an extent model to each input source. The extent model was a β-model of the form

$$f(x,y) = \left(1 + \frac{(x-x_0)^2 + (y-y_0)^2}{r_{\rm c}^2}\right)^{-3\beta+1/2},$$

where β was fixed at the canonical value $\beta = 2/3$ for the surface brightness distribution of clusters of galaxies (Jones & Forman 1984; but see Sect. 9.9 for a discussion of problems arising from this assumption). The core radius, $r_{\rm c}$, the "extent" parameter of a source, was fitted with a constraint that $r_{\rm c} < 80''$. Cases with $r_{\rm c} \leq 6''$ were considered to be consistent with a point source and $r_{\rm c}$ was reset to zero.

An extent likelihood based on the C-statistic and the best-fit point source model as null hypothesis was calculated in an analogous way to that used in the detection likelihood described in Sect. 4.4.3. The extent likelihood $L_{\rm ext}$ is related to the probability P that the detected source is spuriously extended due to Poissonian fluctuation (i.e., the source is point-like) by

$$L_{\rm ext} = -\ln(P).$$

A source was classified as extended if $r_{\rm c} > 6''$ and if the extended model improved the likelihood with respect to the point source fit such that it exceeded a threshold of $L_{\rm ext,min} = 4$.

Since source extent can be spuriously detected by the confusion of two or more point sources, a second fitting stage tested whether a model including a second source further improved the fit. If the second stage found an improvement over the single-source fit, the result could be two point sources or a combination of one point source and one extended source. Note, however, that the previously fitted fainter sources (Sect. 4.4.3) are not recomputed in such cases.

4.5. Astrometric corrections

The positions of X-ray sources were determined during the maximum likelihood fitting of the source. These positions were placed into an astrometric frame determined from the XMM-Newton on-board Attitude & Orbit Control Subsystem (AOCS) which uses XMM-Newton's two star trackers and its "fine sun sensors". The overall accuracy of the XMM-Newton astrometric frame (i.e., the difference between the XMM-Newton frame and the celestial reference frame) is typically a few arcseconds although a few observations suffer rather poorer accuracy.

As the mean positions of bright X-ray sources can be determined to a statistical precision of $\ll 1''$ in the XMM-Newton images, and typical sources to a precision of $1''{-}2''$, it is clearly worthwhile to improve the astrometric precision of the positions. This was done on an observation by observation basis by cross-correlating the source list with the USNO B1.0 catalogue (Monet et al. 2003). This approach depends on the assumptions, usually valid, that a significant number of XMM-Newton detections will have an optical counterpart in the USNO catalogue and that the number of random (false) matches is low. The algorithm used a grid of trial position offsets (in RA and Dec) and rotations between the XMM-Newton frame and the true celestial frame (as defined by the USNO objects) and determined the

optimum combination of offset and rotation values which maximised a likelihood statistic related to the X-ray/optical object separations.

To determine whether the offset/rotation parameters so determined represented an acceptable solution, an empirically determined condition was used. This was based on a comparison of the likelihood statistic determined from the analysis with that calculated for purely coincidental X-ray/optical matches in a given observation, i.e., if there were no true counterparts.

In practice this approach worked very well at high Galactic latitudes, resulting in a high success rate (74% of fields with $|b| \geq 20°$), whilst at low Galactic latitudes (and other regions of high object density) the success rate was much lower (33% of fields with $|b| < 20°$). The typical derived RA, Dec offsets were a few arcseconds, and a few tenths of a degree in field rotation, values consistent with the expected accuracy of the nominal XMM-Newton astrometric frame as noted above.

The 2XMM catalogue contains equatorial RA and Dec coordinates with the above determined astrometric corrections applied and corresponding coordinates which are not corrected. Where the refined astrometric solution was not accepted, the corrected and uncorrected coordinates are identical.

The catalogue also reports the estimated residual component of the position errors, $\sigma_{\rm sys}$[12]. This has the value 0.″35 for all detections in a field for which an acceptable astrometric correction was found and 1.″0 otherwise. The values of $\sigma_{\rm sys}$ in the catalogue are a new determination of the residual error component based on further analysis undertaken after the initial compilation of the catalogue was completed. The details of this analysis are given in Sect. 9.5. Higher initial values of $\sigma_{\rm sys}$ (0.″5 and 1.″5, respectively) were used in earlier stages of the catalogue creation, for example in the external catalogue cross-correlation (see Sect. 6).

4.6. Flux computation

The fluxes, F_i, given in the 2XMM catalogue have been obtained for each energy band, i, as

$$F_i = R_i / f_i$$

where R_i is the corrected source count rate and f_i is the energy conversion factor (ECF) in units of 10^{11} ct cm^2 erg^{-1}. The ECFs depend on camera, filter, data mode, and source spectrum. Since the dependence on data mode is low (1–2%), ECF values were calculated only for the full window mode which is the most frequently used (cf. Table 2). To compute the ECF values, a broadband source spectrum was assumed, characterised by a power law spectral model with photon index $\Gamma = 1.7$ and observed X-ray absorption $N_{\rm H} = 3 \times 10^{20}$ cm^{-2}. As shown in Sect. 9.7 (cf. Fig. 12), this model provides a reasonable representation of the emission of the bulk of the sources in 2XMM. A single model cannot, of course, provide the correct flux conversion for different intrinsic spectra, and the effect of varying the shape of the assumed power-law spectrum on the measured fluxes has been investigated. For example, for $\Delta\Gamma = \pm 0.3$ the fluxes can change by ~6% and ~8% in bands 1 and 5, respectively. The effect is much less (<2%) for bands 2–4 (i.e., between 0.5 keV and 4.5 keV). Very soft or very hard spectra will, of course, produce much greater changes in the conversion factor, particularly in the softest and hardest energy bands.

[12] In the catalogue and associated documentation we refer to this as a "systematic" error. This nomenclature is somewhat misleading as the true nature of this component of the positional errors is far from clear.

Table 4. Energy conversion factors used to compute 2XMM catalogue fluxes (in units of 10^{11} ct cm^2 erg^{-1}).

Camera	Band	Thin	Medium	Thick
pn	1	8.95403	7.82028	4.71096
	2	8.09027	7.83782	6.02015
	3	5.88255	5.78272	5.00419
	4	1.92805	1.90529	1.80647
	5	0.555226	0.554529	0.547205
	9	4.53836	4.43953	3.74772
MOS1	1	1.80399	1.60150	1.06500
	2	1.88017	1.82853	1.48465
	3	2.05034	2.01594	1.79446
	4	0.746128	0.737800	0.707822
	5	0.143340	0.143131	0.141213
	9	1.42040	1.39361	1.23264
MOS2	1	1.81179	1.60670	1.06620
	2	1.88369	1.83088	1.48818
	3	2.05117	2.01594	1.79530
	4	0.750569	0.741687	0.711708
	5	0.150769	0.150560	0.148537
	9	1.42326	1.39647	1.23524

Note that the fluxes given in 2XMM have *not* been corrected for Galactic absorption along the line of sight. The ECF values used in the 2XMM catalogue are shown in Table 4.

Publicly available response matrices (RMFs) were used in the computation of the ECFs[13]. For the pn they were on-axis matrices for single-only events for band 1 and for single-plus-double events[14] for bands 2–5 (*epn_ff20_sY9_v6.7.rmf*, *epn_ff20_sdY9_v6.7.rmf*, respectively). For the MOS cameras there has been a significant change in the low energy redistribution characteristics with time, especially for sources close to the optical axis. In addition, during XMM-Newton revolution 534 the temperatures of both MOS focal plane CCDs were reduced (from −100 C to −120 C), resulting in an improved spectral response thereafter (mainly in the energy resolution). To account for these effects, epoch-dependent RMFs were produced. However, in the computation of MOS ECFs time averaged RMFs were used (for revolution 534). To be consistent with the event selection used to create MOS X-ray images, the standard MOS1 and MOS2 on-axis RMFs for patterns 0–12 were used (*m1_534_im_pall.rmf*, *m2_534_im_pall.rmf*).

Note that for the computation of the ECFs, the effective areas used in the spectral fitting were calculated without the corrections already applied to the source count rates (i.e., instrumental effects including vignetting and bad-pixel corrections, see Sect. 4.3), as well as for the PSF enclosed-energy fraction.

5. EPIC source-specific product generation

The 2XMM processing pipeline was configured to automatically extract source-specific products, i.e., individual time-series (including variability measures) and spectra for the brighter detections. Sources were selected when the following extraction criteria were satisfied: 1) they had ≥500 total-band EPIC counts[15]; 2) the detector coverage of the source, weighted by the PSF for the respective camera, was ≥0.5; and 3) the total-band

[13] EPIC RMFs are available at http://xmm.vilspa.esa.es/external/xmm_sw_cal/calib/epic_files.shtml

[14] Single-only events = pattern 0, single-plus-double events = patterns 1–4.

[15] Where the source was only observed with one or two cameras the equivalent EPIC counts were calculated for the absent camera(s) using the pn to MOS count ratio 3.5:1, representative of the typical source count ratios.

Table 5. Event selection for source products.

	pn	MOS
PATTERN[a]:	≤4	≤12
FLAG[a] for spectra:	FLAG = 0	(FLAG & 0xfffffeff) = 0
FLAG[a] for time-series:	(FLAG & 0xfffffef) = 0	(FLAG & 0x766ba000) = 0
energy range:	0.2[b]−12 keV	0.2[b]−12 keV
GTIs for spectra:	instrumental and background flare GTIs	instrumental and background flare GTIs
GTIs for time-series:	instrumental GTIs	instrumental GTIs
GTIs for variability test:	merged instrumental and background flare GTIs	merged instrumental and background flare GTIs

[a] Column in the event lists; [b] the range 0.2−0.35 keV is set to bad in the spectra.

detection likelihood for the respective camera was ≥15. The decision whether to extract products for a source was based solely on it meeting these extraction criteria in the (merged) exposures used in source detection (Sect. 4.4). However, products for qualifying sources were subsequently extracted for *all* exposures (i.e., imaging event lists) of an observation that adhered to the general exposure selection criteria given in Sect. 4.1 (i.e., items 1−7).

Table 5 shows the event selection criteria for the extraction of the source products. Instrumental GTIs (stored in the event list) are always applied, while GTIs for masking out high background flaring (see Sect. 4.3) were only applied to spectra and the variability tests. Source data were extracted from a circular region of radius $r = 28''$, centred on the detected source position, while the background extraction region was a co-centred annulus with $60'' \leq r \leq 180''$. Circular apertures of radius $r = 60''$ were masked from the background region for any contaminating detection with a likelihood >15 for that camera. These values represent a compromise choice for data extraction by avoiding the additional complexity required to implement a variable extraction radius optimised for each source. Note that the use of an aperture-photometry background subtraction procedure here differs from the use of the background maps applied at the detection stage.

5.1. Spectra

For each source meeting the extraction criteria, the pipeline created the following spectrum-related products: 1) a source+background spectrum (grouped to 20 ct/spectral-bin) and a corresponding background-subtracted XSPEC (Dorman & Arnaud 2001) generated plot; 2) a background spectrum; 3) an auxiliary response file (ARF). Energies below 0.35 keV are considered to be unreliable for the MOS due to low sensitivity and for the pn due to the low-energy noise (in particular at the edges of the detector) and, as such, were marked as "bad" in XSPEC terminology. Data around the Cu fluorescence line for the pn (7.875 keV ≤ E ≤ 8.225 keV) were also marked "bad". The publicly available "canned"[16] RMF associated with each spectrum is conveyed by a header keyword. Some examples of the diversity of source spectra contained amongst the source-specific spectral products are shown in Fig. 6.

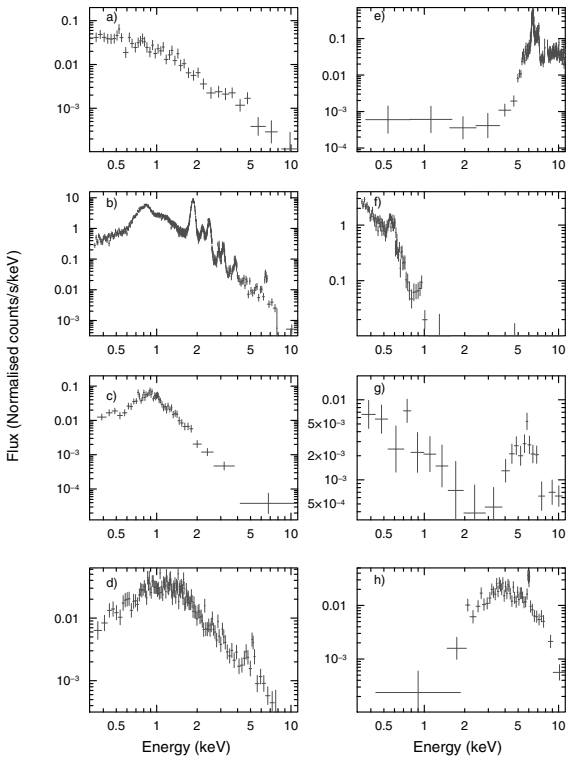

Fig. 6. Examples of auto-extracted 2XMM spectra. Sources are serendipitous objects and spectra are taken from the EPIC pn unless otherwise stated. Panels: **a)** a typical extragalactic source (Seyfert I galaxy); **b)** line-rich spectrum of a localised region in the Tycho supernova remnant (target); **c)** MOS2 spectrum of a stellar coronal source (target; H II 1384, Briggs & Pye 2003), described by two-component thermal spectrum; **d)** spectrum of the hot intra-cluster gas in a galaxy cluster at $z = 0.29$ (Kotov et al. 2006); **e)** heavily absorbed, hard X-ray spectrum of the Galactic binary IGR J16318-4848 (target; Ibarra et al. 2007); **f)** spectrum of a super-soft source with oxygen line emission at ~0.57 keV; **g)** a relatively faint source showing a two-component spectrum; **h)** source with power-law spectrum strongly attenuated at low energies and with a notable red-shifted iron line feature around 6 keV.

5.2. Time-series

Light curves for a given source were created with a common bin-width (per observation) that was an integer multiple of 10 s (minimum width 10 s), determined by the requirement to have at least 18 ct/bin for pn and at least 5 ct/bin for MOS for the exposures used in source detection. All light curves of a given source within an XMM-Newton observation are referenced to a common epoch for ease of comparison.

The light curves themselves can include data taken during periods of background flaring because background subtraction

[16] Pre-computed for the instrument, mode, event pattern selection and approximate detector location of the source.

usually successfully removes its effects. However, in testing for potential variability, to minimise the risk of false variability triggers, only data bins that lay wholly inside both instrument GTIs *and* GTIs reflecting periods of non-flaring background were used.

Two simple variability tests were applied to the separate light curves: 1) a Fast Fourier Transform and 2) a χ^2-test against a null hypothesis of constancy. While other approaches, e.g., the Kolmogorov-Smirnov test, maximum-likelihood methods, and Bayesian methods are potentially more sensitive, the χ^2-test was chosen here as being a simple, robust indicator of variability. The fundamental formula for χ^2 is

$$\chi^2 = \sum_i \frac{(y_i - Y_i)^2}{\sigma_i^2},$$

where y_i is the ith data value, Y_i the model at this point, and σ_i the uncertainty. In the present case, the model Y_i, which incorporates the null hypothesis that the source flux is constant over time, is constructed as follows:

$$Y_i = f_{\mathrm{src},i}\, A_{\mathrm{src}}\, \Delta t\, [\phi_{\mathrm{src}} + \phi_{\mathrm{bkg},i}], \tag{3}$$

where f_i are exposure values, A is the collecting area, Δt is the time-series bin duration, and ϕ is a (bin-averaged) "flux" in counts per unit time per unit area.

The problem now is that a priori the expectation values $\phi_{\mathrm{bkg},i}$ for the background time-series is not known – they must be estimated, with as low an uncertainty as possible, by forming a background time-series in an (ideally) fairly large area which is sufficiently far from the source to avoid cross-contamination. Also, the average source flux ϕ_{src} is not known, which must also be estimated from the (necessarily noisy) data at hand. After some algebra it can be shown that the best estimate for Y_i is given by

$$Y'_i = \frac{f_{\mathrm{src},i}}{\Sigma_j f_{\mathrm{src},j}} \sum_{j=1}^{N} \left(y_j - \frac{A_{\mathrm{src}}}{A_{\mathrm{bkg}}} \frac{f_{\mathrm{src},j}}{f_{\mathrm{bkg},j}}\, b_j \right) + \frac{A_{\mathrm{src}}}{A_{\mathrm{bkg}}} \frac{f_{\mathrm{src},i}}{f_{\mathrm{bkg},i}}\, b_i, \tag{4}$$

where b_i are the measured background counts. The first term of Eq. (3) represents a constant, unweighted time-average of the background-subtracted source counts, derived from the whole light curve, while the second term reflects the background expected in the source aperture for time-bin, i.

The σ values in the χ^2 sum present a problem. In the Pearson formula appropriate to Poissonian data, σ_i^2 is set to Y_i. If we simply substitute Y'_i for Y_i here, the resulting χ^2 values are found via Monte Carlo trials to be somewhat too large. This is because the use of the random background variate b_i in Eq. (4) introduces extra variance into the numerators of the sum. A formula for σ which takes this into account is

$$\sigma_i^2 = Y'_i + \left(\frac{A_{\mathrm{src}}}{A_{\mathrm{bkg}}} \frac{f_{\mathrm{src},i}}{f_{\mathrm{bkg},i}} \right)^2 b_i.$$

For each exposure used, the pipeline generated a background-subtracted source time-series and the corresponding background time-series (corrected for exposure, cosmic rays, and dead time), together with the graphical representations of the data and of its power spectrum. The χ^2-statistics and probabilities are conveyed by header keywords. Some example total-band time-series from these products that highlight the range of source variability present in the 2XMM catalogue are shown in Fig. 7.

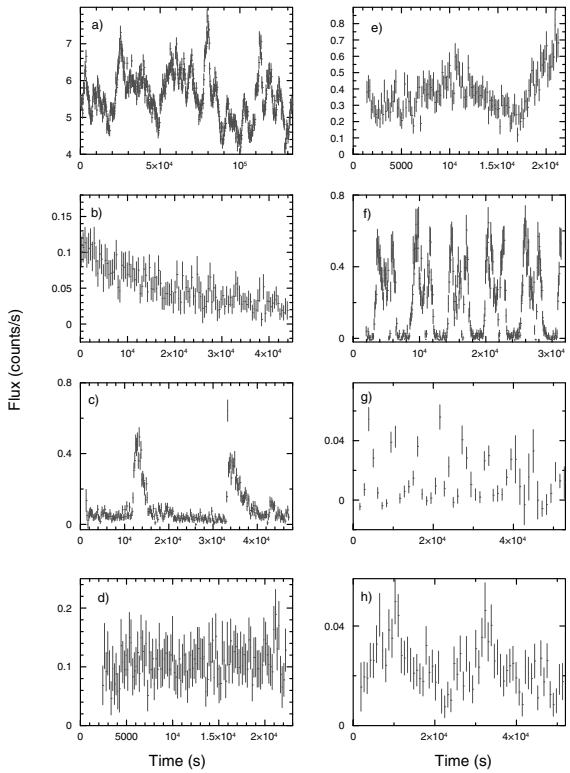

Fig. 7. Example auto-extracted 2XMM time-series. Sources are serendipitous objects and the data are taken from the pn unless otherwise stated. Panels: **a)** MOS1 data for Markarian 335 (Seyfert I – target); **b)** MOS1 data showing the decay curve of GRB 050326 (target); **c)** X-ray flares from a previously unknown coronally active star; **d)** time-series of the emission from a relatively faint cluster of galaxies, showing no significant variability (target); **e)** time-series of the obscured Galactic binary IGR 16318-4848 (target; Ibarra et al. 2007); **f)** previously unknown AM Her binary showing several phase-stable periodic features (Vogel et al. 2007); **g)** highly variable AND periodic object, likely to be a cataclysmic or X-ray binary (Farrell et al. 2008) – the binning results in poor sampling of the intrinsic periodic behaviour; **h)** source showing clear variability but not flagged as variable in the catalogue (the probability of variability falls below the threshold of 10^{-5}). These last two cases highlight the sensitivity of the variability characterisation on the time bin size.

5.3. Limitations of the automatic extraction

As with any automated extraction procedure, a few source products suffer from problems such as low photon statistics, low numbers of bins, background subtraction problems, and contamination.

Spectra with few bins can arise for very soft sources where the total-band counts meet the extraction criteria but the bulk of the flux occurs below the 0.35 keV cut-off (Sect. 5.1). This can also occur if the extraction is for an exposure with a shorter exposure time than those used in the detection stage, especially if the detection was already close to the extraction threshold. Similarly, background over-estimation in the exposure (or underestimation in the original detection exposure) can result in fewer source counts compared to those determined during the detection stage, yielding poorer statistics and low bin numbers for the time-series and spectra. This can occur when spatial gradients across the background region are imperfectly characterised, e.g., where the source lies near strong instrumental features such as OOT events, where there are marked steps in the count-rate levels between adjacent noisy and non-noisy CCDs,

or where contaminant source exclusions are biased to one side of a background region that overlaps the wings of a very bright source or bright extended emission. In many cases the automatic (Sect. 7.3) as well as manual flag settings (Sect. 7.4) indicate whether source products are likely to be reliable.

Contamination of the source extraction region (e.g., by another source, OOT events, or single reflections) can also cause problems if the contamination is brighter than or of comparable brightness to the extracted source. The nearest-neighbour column can act as an initial alert in such cases – 19% of the catalogue sources with spectra have neighbouring detections (of any brightness) within 28″ (i.e., the extraction radius).

The extraction process and exposure corrections are optimised for point sources. Absolute fluxes in source-specific products of extended sources, therefore, may not be reliable. However, relative measures such as variability and spectral line detection should still be indicative.

5.4. Known processing problems

A few products are affected by known processing problems:

(i) when the usable background region is very small, the background area calculation becomes imprecise and results in an inaccurate background-subtracted source spectrum. This can occur with bright sources in MOS W2 and W4 partial window modes where most of the background region lies outside the 110″ × 110″ window or in crowded areas where the source-free area is markedly reduced. In the former case the source is usually bright enough that background subtraction has negligible impact and so does not need to be performed;

(ii) attitude GTIs were not included in the extraction criteria, and occasionally the source was significantly displaced with respect to the aperture as defined by the detection image (in extreme cases, off the detector). This will affect the calculation of count rates in the spectra and the variability measurements for the time-series;

(iii) occasionally the light curve exposure correction failed (i.e., no time-series were produced) or light curves were inadequately corrected for strong background variations across CCDs (which can cause spurious variability detection). The latter cases are confined to very bright extended sources and are mostly associated with spurious detections;

(iv) neither spectra nor time-series are corrected for pileup (nor are the source count rates in the catalogue). Due to the difficulties in detecting and quantifying pileup no attempt has been made to flag this effect.

6. External catalogue cross-correlation

As part of the XMM-Newton pipeline, the Astronomical Catalogue Data Subsystem (ACDS) generated products holding information on the immediate surrounding of each EPIC source and on the known astrophysical content of the EPIC FOV, highlighting the possible non-detection of formerly known bright X-ray sources as well as indicating the presence of particularly important astrophysical objects in the area covered by the XMM-Newton observation.

In addition to Simbad[17] and NED[18], 202 archival catalogues and article tables were queried from Vizier[19]. They were selected on the basis of their assumed high probability to contain the actual counterpart of the X-ray source. Basically all large area "high density" astronomical catalogues were considered, namely the SDSS-DR3 (Abazajian et al. 2005), USNO-A2.0 (Monet et al. 1998), USNO-B1.0 (Monet et al. 2003), GSC 2.2 (STScI 2001), and APM-North (McMahon et al. 2000) catalogues in the optical, the IRAS (Joint Science WG 1988; Moshir et al. 1990), 2MASS (Cutri et al. 2003), and DENIS (DENIS consortium 2005) catalogues in the infrared, the NVSS (Condon et al. 1998), WISH (de Breuck et al. 2002), and FIRST (Becker et al. 1997) catalogues at radio wavelengths, and the main X-ray catalogues produced by Einstein (2E; Harris et al. 1994), ROSAT: RASS bright and faint source lists (Voges et al. 1999, 2000), RBS (Schwope et al. 2000), HRI (ROSAT Team 2000), PSPC (ROSAT 2000), and WGACAT (White et al. 2000) catalogues of pointed observations), and XMM-Newton (1XMM; XMM-SSC 2003). Also included were large lists of homogeneous objects (e.g., catalogues of bright stars, cataclysmic variables, LMXBs, Be stars, galaxies, etc.). The full list of archival catalogues queried is included as one of the pipeline products.

The XMM-Newton detections were cross-correlated with the archival entries taking into account positional errors in both the EPIC and the archival entries. The list of possible counterparts did not provide additional information on the relative merits of the cross-correlation or on the probability that the given archival entry was found by chance in the error circle of the X-ray source.

The cross-correlation was based on the dimensionless variable:

$$r^2 = \frac{\Delta\alpha^2}{\sigma_\alpha^2} + \frac{\Delta\delta^2}{\sigma_\delta^2}$$

with $\sigma_\alpha^2 = \sigma_{\alpha_x}^2 + \sigma_{\alpha_o}^2$ and $\sigma_\delta^2 = \sigma_{\delta_x}^2 + \sigma_{\delta_o}^2$, where σ_{α_x} and σ_{δ_x} are the standard deviations in RA and Dec of the X-ray source position and σ_{α_o} and σ_{δ_o} the corresponding errors on the position of the archival catalogued object. The error on the X-ray position is the quadratic sum of the statistical error with the additional error which depends on the effectiveness of the astrometric correction (cf. Sect. 4.5). Positional errors of the archival entries were either read from the respective catalogue or fixed according to guidance in the relevant catalogue literature. In all cases, the significance of the error was rescaled to the 1σ-level.

The probability density distribution of position differences between the X-ray source and its catalogue counterpart due to measurement errors is a Rayleigh distribution. Hence, the probability of finding the X-ray source at a distance between r and $r + \delta r$ from its archival counterpart is:

$$\delta p(r|id) = r \cdot \mathrm{e}^{(-r^2/2)}\, \delta r,$$

with a cumulative distribution function:

$$\int_0^r \delta p(r|id) = \left(1 - \mathrm{e}^{(-r^2/2)}\right).$$

Thus, lists of counterparts with $r(\sigma) < 2.146, 3.035$, and 3.439 are 90%, 99%, and 99.73% complete, respectively. Computing the actual reliability of the identification requires a careful calibration of the density of catalogue sources and of the likelihood ratio method applied; in the near future, such reliabilities will be provided for candidates found in the main archival catalogues. However, in the absence of such information at the pipeline level, it was decided, for completeness to list all possible identifications having positions consistent with that of the X-ray source at the 99.73% confidence level, corresponding to 3σ.

[17] The SIMBAD astronomical database (Wenger et al. 2000).
[18] The NASA/IPAC extragalactic database.
[19] The VizieR Service at CDS (Ochsenbein et al. 2000).

The ACDS results are presented in several interconnected HTML files (together with copies in FITS format). Graphical products are 1) a plot with the position of all quoted archival entries on the EPIC merged image; 2) an overlay of the position of the X-ray sources detected in the EPIC camera and contours of the EPIC merged image on a ROSAT all-sky survey image; and 3) finding charts based on sky pixel data provided by the CDS Aladin image server (Bonnarel et al. 2000).

7. Quality evaluation

As part of the quality assurance for the data processing, a number of procedures, both automated and manual, were performed on many of the data products to take note of intrinsic problems with the data as well as to detect software issues. Particular emphasis was given to potential problems with the source detection and characterisation, and quality flags were set accordingly.

7.1. Visual screening of data products

The overall visual screening included data products from all three instrument groups (EPIC, RGS, OM) as well as those from the external catalogue cross-correlation (cf. Sect. 6). Only products that could be conveniently assessed were inspected using a dedicated screening script, that is, most HTML pages, all PNG images and all PDF plots (as representatives of data from the FITS files), all EPIC FITS images and maps (including source-location overlays), and the mosaiced OM FITS images with source overlay. For each observation a screening report with standardised comments was created, recording data and processing problems (see, for example, Sect. 5.4), and made available via the XSA.

As a result of the visual screening, two otherwise eligible observations (obtained for experimental mode tests) were excluded from the catalogue since the tested mode was not properly supported by the processing system and the source parametrisation was considered to be unreliable.

7.2. Potential source detection problems

Intrinsic features of the XMM-Newton instrumentation combined with some shortcomings of the detection process have given rise to detections that are obviously spurious[20]. Possible causes range from bright pixels and segments to OOT events (in the case of pileup), RGA scattered light, single reflections from the mirrors, and optical loading (cf. Appendix A and Fig. 4a). In cases where the spatial background varied rapidly (e.g., PSF "spikes", filamentary extended emission, edges of noisy CCDs), the spline background map may deviate from the true background. This could potentially have given rise to spurious source detections and could also have affected the measured parameters (including time-series and spectra) of real sources.

Extended sources were particularly difficult to detect and parametrise due to their (often) filamentary or non-symmetric structure as well as the maximum allowed extent in fitting (80″, Sect. 4.4.4). This often led to multiple detections of a large or irregular extended emission region. On the other hand, multiple point sources (e.g., in a crowded field) might also be detected as extended (due to computational restrictions no attempt was made to distinguish more than two overlapping/confused point sources). See Sect. 9.9 and Fig. 14 for a discussion of extended sources and some examples.

[20] Spurious detections caused by the background noise (as characterised by their likelihood) are not discussed in this section, see Sects. 4.4 and 9.4.

7.3. Automated quality-warning flags for detections

Some of the source detection problems could be identified and quantified so that the processing software could set automated quality warning flags in the source lists. For each detection, four sets of flags (one per camera plus a summary set covering all cameras), each containing twelve entries, were written into the observation source list. Nine of the flags in each set were populated based on other key quantities available in the same source list. The meaning of these flags is summarised in Table 6. The default value of every flag was False; when a flag was set it means it has been changed to True. For each detection, Flags 2–7 were set in a common fashion across all four sets. Flags 1, 8, and 9 are camera-specific, but any set to True were also reflected in the summary set.

The criteria used to set the flags were determined largely empirically from tests on appropriate sample data-sets (cf. Fig. 4b, for some examples). Flags set to True should be understood mainly as a warning: they identify possible problematic issues for a detection such as proximity to a bright source, a location within an extended source emission, insufficient detector coverage of the PSF of the detection, and known pixels or clustering of pixels that tend to be intrinsically bright at low energies. In all these cases the parameters of a real source may be compromised and there is a possibility that the source is spurious.

Extended sources near bright sources and within larger extended emission are most likely to be spurious and have been flagged as such. In addition, extended detections triggered by hot pixels or bright columns can be identified since their likelihood in one band (of one camera) is disproportionally higher than in the other bands and cameras. However, no attempt has been made to flag spurious extended detections in the general case, that is, in areas where the background changes considerably on a small spatial scale and the spline maps cannot adequately represent this. At the same time, no point sources have been specifically flagged as spurious (see Sect. 7.4 regarding manual flagging) though they are often caused by the same features as the spurious extended detections. The spatial density of real point sources is, in general, much higher than for extended sources and the reliability of such a "spurious" flag would be low. Instead, Flags 2, 3, and 9 can be used as a warning that such a source could be spurious.

7.4. Manual flag settings for detections

In addition to the automated quality flags, a more rigorous visual screening of the source detection was performed for the EPIC fields to be used in the catalogue. The outcome of this process was reflected in two flags (11 and 12) as described below and summarised in Table 6.

Images of each field, with source overlay, were inspected visually and areas with likely spurious detections were recorded (as ds9-regions; Joye & Mandel 2003). Such regions could be regular (circle, ellipse, box) or irregular (polygon); in cases where only a single detection was apparently spurious a small circle of 10″ radius was used, centred on this detection. It should be stressed that these regions, except for the latter case, could include both suspected spurious and real detections. In many cases (especially at fainter fluxes) it was impossible to visually distinguish between a real source and a spurious detection that

Table 6. Description of the automated (Flags 1−9) and manual (Flags 11−12) quality warning flags.

Flag	Description	Definition for flag to be set True (cf. Notes)
1	Low detector coverage	$m_{\rm camera} < 0.5$
2	Near other source	$r \le 65 \cdot \sqrt{R_{\rm epic}}$ AND $r_{\rm min} = 10''$ AND $r_{\rm max} = 400''$
3	Within extended emission	$r \le 3 \cdot E$ AND $r_{\rm max} = 200''$
4	Possible spurious extended detection near bright source	Detection is extended AND Flag 2 is set AND $c_{\rm epic} \ge 1000$
5	Possible spurious extended detection within extended emission	Detection is extended AND $r \le 160''$ AND fraction of rate compared with originating source is ≤0.4
6	Possible spurious extended detection due to unusual large single-band detection likelihood	Detection is extended AND fraction of detection likelihood per camera and band compared with the sum of all is ≥0.9
7	Possible spurious extended detection	At least one of the flags 4, 5, 6 is set
8	On bright MOS1 corner or bright low-gain pn column	Source position is located on one of the affected pixels
9	Near bright MOS1 corner	Source position within $r_f = 60''$ of a bright corner pixel
10	Not used	
11	Within region where spurious detections occur	Set manually
12	Bright ("originating") point source in region where spurious detections occur	Set manually

Notes: m is the detector coverage of the detection weighted by the PSF; r is a radial distance in arcseconds from the "originating" source within which all detections receive this flag; $R_{\rm epic}$ is the EPIC source count rate in ct/s of the "originating" source; E is the extent parameter (core radius) of the "originating source" in arcseconds (cf. Sect. 4.4.4); $c_{\rm epic}$ is the EPIC source counts of the "originating" source; r_f is the radius used for source PSF fitting in arcseconds.

was caused by artefacts on the detector or by insufficient background subtraction. In addition, the effect of such features on the parameters of a nearby real source has not been investigated in detail. For example, single reflections or the RGA scattered-light features were not included in the background maps and may therefore have affected the source parameters. On the other hand, as the source parameters are derived by the fitting process in order of decreasing source brightness, the parameters of fainter sources take the PSF of nearby bright sources into account (Sect. 4.4).

The ds9-regions were converted to EPIC image masks where the bad areas have the value zero and the rest of the field has the value one. These masks are available as catalogue products (Sect. 10); they can be combined with the camera detection masks to study, for example, the sky coverage.

The masks were used to flag sources within the masked areas with Flag 11. In many cases, the so-called "originating" source (a bright point source, cf. Flag 2, or a large or irregular extended source, cf. Flag 3) was located within the masked region. Though the brightest source was fitted before the fainter ones, the contribution of the faint sources to the fit of the bright source is considered to be negligible (Sect. 4.4.3). Hence, the "originating" point source was identified by setting its Flag 12[21] to distinguish it from the other detections with Flag 11 in that particular ds9-region, the parameters of which may be affected by the presence of the indicated bright source due to imperfections in the PSF used. In the case of bright extended sources, however, the situation was different: the extent parameter was obviously affected by nearby spurious detections, and consequently the brightness was underestimated. Flag 12 was therefore only set for point sources.

7.5. Quality summary flag

For easier use of the quality-flag information, the catalogue gives a summary flag which combines the flags described above (11 per camera per detection) to give a single, overall quality indication for each detection. Its five possible values are as follows (in order of increasing severity):

0: there are no indications of problems for this detection; none of the flags [1−12] for the three cameras [pn, M1, M2] are set to True. This value can be used to obtain the cleanest possible samples (but possibly at the expense of omitting some otherwise acceptable detections); (71% of all detections.)

1: the source parameters are considered to be possibly compromised; at least one of the warning flags [1, 2, 3, 9] for any of the cameras [pn, M1, M2] is True. This value can be used to accept detections for further potential use, but they should be subjected to careful scrutiny dependent on the specific application; (9% of all detections.)

2: the detection may be spurious but was not recognised as such during visual inspection; at least one of the automated "spurious detection" flags [7, 8] for any of the cameras [pn, M1, M2] is True but the manual flag [11] is False. This value can be used to accept detections for further potential use, but they should be subjected to careful scrutiny dependent on the specific application; (1% of all detections.)

3: the detection lies in a region where spurious detections occur but which could not be dealt with in an automated way; the manual flag [11] is True but the automated "spurious detection" flags [7, 8] of all the cameras [pn,M1,M2] are False. Detections with this value should be used only after very careful scrutiny, as they may well be spurious, *unless* flag 12 is True, in which case the detection (and possibly its parameters) may well be valid, as it is likely to be a strong source; (15% of all detections, where Flag 12 was set for 600 detections.)

4: the detection lies in a region where spurious detections occur and is flagged as likely spurious; the manual flag [11] is True and any of the automated "spurious detection" flags [7, 8] for any of the cameras [pn, M1, M2] is also True. It is recommended that detections with this value should not normally be used. (4% of all detections.)

Flag 12 was not included in the summary flag, selecting by Flag 12 as well can provide a clean as well as a more complete sample, as noted above, since this flag is usually given to reasonably bright point sources.

[21] Note that Flag 12 was not set when the source appeared to be split into two, cf. Sect. 4.4.4, or when a close-by fainter detection appeared to be of comparable brightness.

Table 7. Observation class definitions.

Class	%age of 2XMM obs	Definition	Comment
0	38%	bad area = 0%	no region has been identified for flagging
1	12%	0% < bad area < 0.1%	≲3 single detections
2	10%	0.1% ≤ bad area < 1%	circular region with $40'' \lesssim r \lesssim 60''$
3	25%	1% ≤ bad area < 10%	circular region with $60'' \lesssim r \lesssim 200''$
4	10%	10% ≤ bad area < 100%	circular region with $r \gtrsim 200''$
5	5%	bad area = 100%	the whole field is flagged as bad

The screening flags also offer a means of avoiding source-specific data products with possible problems, noting that of all detections with products a significant fraction have summary flag ≥3 indicating potential issues with the spectra and/or time series.

7.6. Overall observation classification

The summary flag assigned to each detection in the catalogue provides an overall classification of each detection included in the catalogue. On the other hand, since about half of all observations in the catalogue are little affected by artefacts and background subtraction problems, an *observation classification* offers the possibility of selecting good quality *fields* rather than good quality detections. This classification is based on the fraction of area masked out in the flag mask (Sect. 7.4) as compared to the total area used in the source detection (from the combined EPIC detection mask) for that observation. Six classes of observations were identified. They are listed in Table 7 together with the percentage of observations affected, the fractional area, and the approximate size of the excluded region (note that the flag mask may comprise several regions in various shapes).

8. Catalogue compilation

The 2XMM catalogue is a catalogue of detections. As such, every row in the 2XMM catalogue represents a single detection of an object from a separate XMM-Newton observation. The construction of the 2XMM catalogue consists of two main steps. The first involves the aggregation of the data of individual detections from the separate observation source lists into a single list of detected objects, adding additional information about each detection and meta-data relating to the observation in which the detection was made. The second step consists of cross-matching detections, identifying resulting unique celestial objects and combining or averaging key quantities from the detections into corresponding unique-source values. Ultimately, the ensemble of data for both detections and unique sources becomes the catalogue.

The primary source of data for the catalogue was the set of 3491 EPIC summary source list files from the maximum-likelihood source-fitting processes (Sect. 4.4.3). Additional information incorporated into the catalogue for each detection includes the detection background levels, the variability information (from the EPIC source time-series files; see below) and the detection flags from the automatic flagging augmented by the manual data screening process (see Sects. 7.4, and 7.5). Ancillary information added to the catalogue entries also includes various observation meta-data parameters (e.g., observation ID, filters and modes used) and the observation classification determined as part of the data screening process (Sect. 7.6). In the final catalogue table each detection is also assigned a unique detection number.

The measured and derived parameters of the detections taken from the pipeline product files are reflected in the 2XMM catalogue by a number of columns described in Appendix D.1–D.6. For the variability information for detections (Appendix D.6), the variability identifier was set to True for a detection if at least one of the time-series for this detection (derived from all appropriate exposures) had a χ^2-probability $\leq 10^{-5}$ based on the null hypothesis that the source was constant (cf. Sect. 5.2). The probability threshold was chosen to yield less than one false trigger over the entire set of time-series. Where the flag was set, the camera and exposure ID with the lowest χ^2-probability were also provided for convenience. No assessment of potential variability has been made between observations for those sources detected more than once.

8.1. Unique celestial sources

XMM-Newton observations can yield multiple detections of the same object on the sky where a particular field is the subject of repeat pointings or because of partial overlaps from dedicated mosaic observations or fortuitous overlaps from unrelated pointings. As such, the catalogue production process also sought to identify and collate data for all detections pertaining to unique sources on the sky, providing a unique-source indexing system within the catalogue. In parallel, the catalogue provides a number of derived quantities relating to the unique sources computed from the constituent detections.

To identify unique sources from multiple detections, reliable estimates of the position error, $\sigma_{\rm pos}$, of each detection are essential. The best estimate of the position error was found to be

$$\sigma_{\rm pos} = \sqrt{\sigma_{\rm sys}^2 + \sigma_{\rm stat}^2}, \quad (5)$$

where $\sigma_{\rm sys}$ is the additional error (Sect. 4.5, see also footnote 12) and $\sigma_{\rm stat}$ is the statistical centroid uncertainty measured from the source-fitting stage (Sect. 4.4.3).

Two detections from different observations with respective position errors of σ_1 and σ_2 were assumed to be potentially associated with the same celestial source if their separation is

$$r_{\rm sep} < 3(\sigma_1 + \sigma_2),$$

with 7″ as an upper-limit. The 7″ limit to position offsets in the matching process was determined empirically as the best value to prevent spurious matches (dominated by a few weak extended sources with large position errors) without having a significant effect on the number of genuine matches. A match was, however, rejected if $r_{\rm sep} > 0.9\ d_1$ or $r_{\rm sep} > 0.9\ d_2$ where d_1 and d_2 are the distances from the detection to its nearest neighbour in the same observation. This latter provision means that no two distinct sources from the same image should be matched. No quality flag information was used in the matching process.

Using these constraints, the detection table was cross-correlated with itself to find all possible pairs of detections having error-circle overlaps. Some detections were found to have as

many as 31 such overlaps, since a few areas of sky were observed this many times (generally calibration observations). Resolving this list into a set of unique celestial sources required some experimentation because of potential ambiguity in a few crowded or complex fields. The extreme scenarios were 1) to assume a set of detections was associated with a unique source only if they all overlapped each other – this was considered too conservative; 2) to assume that a set of detections constituted a unique source if each member overlapped at least one other member – this was deemed overly generous, i.e., it would have included a few pairs of detections whose mutual separations would be incompatible with coming from a single source. The algorithm adopted gave priority to those detections with the highest number of overlaps (because they were likely to be near the true source centre) and, this number being equal, to count-rate agreement. The list of overlapping detections was therefore sorted in descending order of the number of overlaps and the EPIC total-band count rate and then processed in that order. Each detection was associated with all its overlapping detections, except those which had already been removed from the list by having been associated with another (better connected or stronger) detection. In the final catalogue the number of detections which might have been associated with a source different from the one actually assigned to them, given a different order of processing, was about one hundred, which was significantly lower than the figure from various alternative algorithms. These ambiguous detections were almost all from observations which the screening process flagged as unreliable, suggesting that further refinements to the algorithm would have been of little practical value.

The algorithm adopted for the identification of unique sources appears to be reliable in the great majority of cases, but there are known to be a few confused areas where the results are likely to be imperfect. The most common cause is where real diffuse or bright objects give rise to (generally spurious) additional detections which happen to approximately coincide spatially in different observations. In most cases it is likely that the sources will have received a manual flag. Incorrect matching can also potentially occur where centroiding is adversely affected by pileup or optical loading, where one or more contributing observations have significant attitude errors which could not be astrometrically rectified (Sect. 4.5), or where a real source is located close to another detection associated with an artefact such as residual OOT events from a strongly piled-up source elsewhere in the image. Where pileup or artefacts are involved, affected sources may have been assigned automatic or manual flags anyway. It should be emphasised, however, that flag information is not used in the source matching process. Based on the extensive visual inspection, incorrect detection matching is believed to be extremely rare (<200 detections affected). Inevitably, in a few cases, the matching process fails to match some detections that belong together.

A number of quantities for unique sources are included in the 2XMM catalogue, based on error-weighted merging of the constituent detection values (see Appendix D.7). The IAU name of each unique source was constructed from its coordinates. Note that an individual detection is completely specified by its IAU name *and* its detection identifier. The unique-source data were augmented with five quantities that were not based on error-weighted merging: 1) the unique-source detection likelihood was set to the highest EPIC total-band detection likelihood, i.e., it reflects the strongest constituent detection of a unique source; 2) a unique-source extent likelihood was computed as the simple average of the corresponding EPIC detection values; 3) the reduced χ^2-probability for the variability of a unique source was taken as the lowest of the detection values, indicative of the detection with the highest likelihood of being variable, where variability information was available; 4) where variability information existed for any of the constituent detections, a unique-source variability identifier was set to True if any were True and to False if none were True. Where no variability information was available, the unique-source flag was set to Undefined; 5) a unique-source summary flag took the maximum of the detection summary flag values (Sect. 7.5), i.e., reflecting the worst-case flag from any of the detections of the source.

The 2XMM catalogue was also cross-correlated against the 1XMM and 2XMMp catalogues during the construction process. For each unique 2XMM source, the most probable matching 1XMM counterpart and 2XMMp counterpart were identified and listed in the 2XMM catalogue. The matching algorithm employed was similar to the one described for identifying unique sources but the maximum positional offset between the new catalogue and the older ones was set at 3″. This was a rather conservative value but since a number of sources in 1XMM, especially, have positional errors greater than this, it ensures that there are very few incorrect matches or ambiguous cases.

This resulted in ~88% of all 2XMMp sources having a match with 2XMM sources. Apart from those lying outside the 3″ matching circle, non-matched sources are found to be either spurious, at the detection limit, or the observation was not included in 2XMM. Comparison with 1XMM is not straight forward due to the differences in the detection scheme (e.g., the source detection in 1XMM was done per camera) and likelihood cutoffs. Note, though, that 1XMM comprises only 585 of the 2XMM fields.

9. Catalogue characterisation and results

9.1. Overall properties

The catalogue contains 246 897 detections drawn from 3491 public XMM-Newton observations (Fig. 1). These detections relate to 191 870 unique sources. Of these, 27 522 X-ray sources were observed more than once; some were observed up to 31 times in total due to the fact that many sky regions are covered by more than one observation. Of the 246 897 X-ray detections, 20 837 are classified as extended. Table 8 shows the number of detections and unique sources per camera and energy band (split into point sources and extended sources); a likelihood threshold $L \geq 10$ has been applied but no selection of detection flags has been made.

The catalogue contains detections down to an EPIC likelihood of 6. Around 90% of the detections have $L > 8$ and ~82% have $L > 10$. Simulations demonstrate that the false detection rate for typical high Galactic latitude fields is $\sim[2, 1, 0.5]$% for detections with $L > [6, 8, 10]$ respectively (Sect. 9.4). We note that the source detection in 2XMM has a low degree of incompleteness for $L \lesssim 10$. This arises from the fact that the first stage of the source detection (Sect. 4.4.2) requires that each detection have $L \geq 5$. As this first stage of the processing is relatively crude, the incompleteness primarily arises from this preselection of low significance detections.

The 2XMM catalogue is intended to be a catalogue of serendipitous sources. The observations from which it has been compiled, however, are of course pointed observations which typically contain one or more target objects chosen by the original observers, so the catalogue contains a small fraction of targets which are by definition not serendipitous. Appendix C provides details of the target identification and classification. From

Table 8. Numbers of detections with likelihood $L \geq 10$ in the 2XMM catalogue.

Camera	Energy band (keV)	Point source	Ext'd source	Unique point source	Unique ext'd source
pn	0.2–0.5	38 074	4319	30 811	3843
pn	0.5–1.0	63 248	7457	50 639	6714
pn	1.0–2.0	68 197	6217	55 035	5555
pn	2.0–4.5	37 511	3604	30 702	3167
pn	4.5–12.0	11 144	1586	8682	1337
M1	0.2–0.5	20 841	3392	15 887	2958
M1	0.5–1.0	40 965	6734	30 998	5892
M1	1.0–2.0	52 569	6754	40 062	5882
M1	2.0–4.5	34 230	4452	26 710	3858
M1	4.5–12.0	7818	1825	5776	1547
M2	0.2–0.5	20 626	3485	15 718	3012
M2	0.5–1.0	42 488	7045	32 055	6149
M2	1.0–2.0	56 060	6997	42 624	6107
M2	2.0–4.5	36 760	4703	28 538	4080
M2	4.5–12.0	8546	2008	6265	1716

this analysis we find that around 2/3 of the intended targets are unambiguously identified in their XMM-Newton observations but, allowing for multiple detections, only ~1400 targets are plausibly associated with 2XMM catalogue sources. This means that <1% of 2XMM sources are the target of the observation, although in a few observations (e.g., nearby galaxies) the number of sources *associated* with the target can clearly be much greater.

More generally the fields from which the 2XMM catalogue is compiled may also not be representative of the overall X-ray sky. The classification of the XMM-Newton observations (Appendix C and Table D.2) is relevant to avoiding potential selection bias in the use of the catalogue.

9.2. Sky coverage and survey sensitivity

To compute the effective sky coverage, the sky was notionally covered by a grid of pixels using the HEALPix projection (Gorski et al. 2005). Adequate resolution was obtained using pixels ~13″ across. For each observation included in 2XMM the exposure times were computed for each HEALPix pixel taking into account the exposure map for each observation (i.e., the actual coverage taking into account observing mode, CCD gaps, telescope vignetting, etc.). From this analysis we find that in total the catalogue fields cover a sky area of more than 500 deg^2. The non-overlapping sky area is ~360 deg^2 (~1% of the sky).

The sensitivity of the 2XMM survey catalogue was estimated empirically using the method of Carrera et al. (2007). The algorithm presented in their Appendix A was used to compute sensitivity maps for each instrument and energy band, using data from the exposure maps and background maps from each observation. Using a grid of HEALPix pixels in a similar way to that outlined above, the limiting flux of the *most sensitive* observation of each part of the sky was estimated. Figure 8 shows the sky area against limiting flux for each EPIC camera and energy band separately. This analysis provides a relatively robust estimate of the total sky area of the 2XMM catalogue for each of the three EPIC cameras, although it does not take into account those sky regions which are effectively useless for serendipitous source detection due to the presence of bright objects or certain instrumental artefacts (see discussion in Sect. 3.1 and Fig. 4b and c)[22]. These area-flux plots computed for $L > 10$ show that

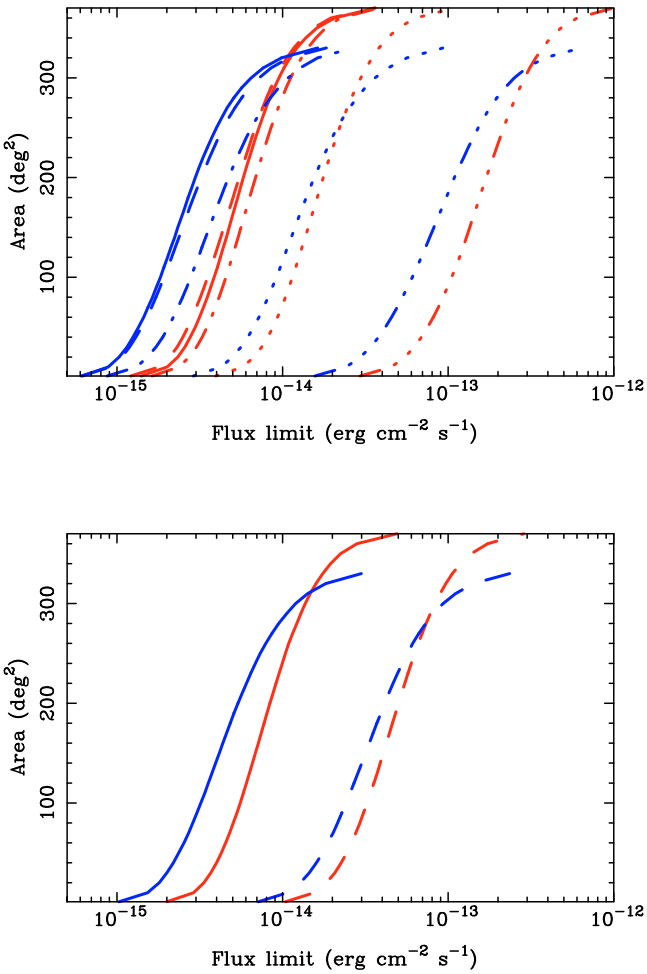

Fig. 8. Sky area as a function of flux limit for the 2XMM catalogue computed for sources with a detection likelihood limit $L \geq 10$ in the respective energy band. Red curves are for MOS2; blue curves are for pn. (MOS1 is not shown but is very similar to MOS 2). *Top panel*: energy bands 1, 2, 3, 4, and 5 for each camera are shown with solid, long-dash, dash-dot, dotted, and dot-dot-dot-dashed line styles, respectively. *Bottom panel*: energy bands 6 and 7 for each camera are shown with solid and long-dash styles, respectively.

the effective sky coverage for the MOS2 camera is ~370 deg^2 (for the MOS1 camera it is ~360 deg^2 due to the loss of one of the MOS1 CCDs in March 2005), whilst for the pn camera the area is ~330 deg^2, due primarily to reduced or zero imaging sky area provided by some of the pn observing modes. The limiting fluxes vary between camera and energy band. For the pn camera which provides the highest sensitivity, the minimum detectable fluxes in the soft (0.5–2 keV), hard (2–12 keV) and hardest (4.5 – 12 keV) bands at 10% sky coverage are ~[2, 15, 35] × 10^{-15} erg cm^{-2} s^{-1}, respectively. The fluxes for >90% sky coverage (i.e., close to complete coverage) in these bands are ~[1, 9, 25] × 10^{-14} erg cm^{-2} s^{-1} respectively.

9.3. Flux and count distributions

The distribution of fluxes for the 2XMM catalogue detections is shown in Fig. 9. This figure illustrates that the typical soft-band flux for the catalogue sources is ~5×10^{-15} erg cm^{-2} s^{-1} and

[22] Figure 8 also does not take into account the effects of Poisson noise which produces a probability distribution for source detectability about the sensitivity limit. These effects are only important at the low count limit, i.e. essentially only at faint fluxes, cf. Georgakakis et al. (2008).

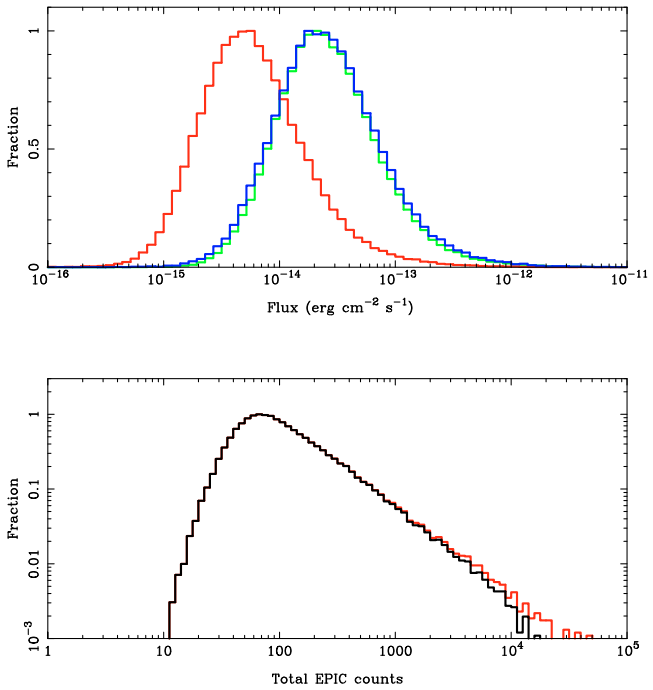

Fig. 9. *Top*: distribution of point source fluxes for the 2XMM catalogue in the soft (red), hard (blue), and total band (green) energy bands. The targets of the individual XMM-Newton observations are excluded from these distributions (see Sect. C.1). Detections selected for these distributions have likelihood $L \geq 10$ in the relevant bands. Only sources with summary flag 0 are included. *Bottom*: distribution of total EPIC counts for the same sample of 2XMM detections.The red histogram shows the distribution if the XMM-Newton targets are included.

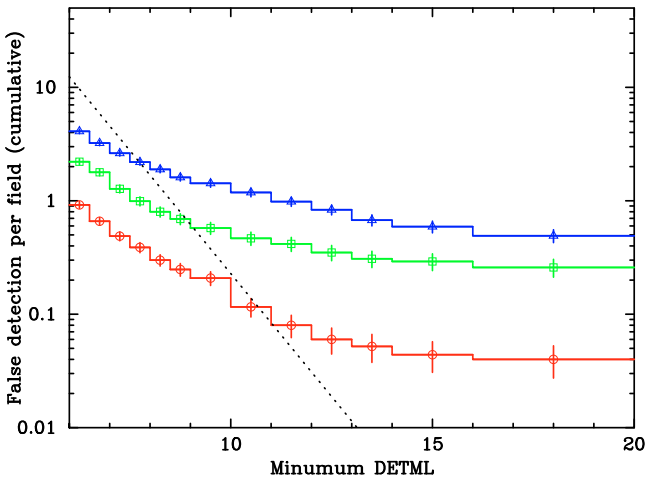

Fig. 10. The number of false detections per field estimated via simulations for typical high Galactic latitude fields as a function of $L_{\rm min}$ for various exposure times. The red circles show the results for exposures of 12 ks for MOS and 8 ks for pn (~70% of the median values), whereas the green squares and blue triangles show those with the exposures of 3 and 10 times higher respectively. The dotted line represents the theoretical false detection number assuming 5000 independent detection cells per field (see text).

is $\sim 2 \times 10^{-14}$ erg cm^{-2} s^{-1} in the hard and total bands. These values correspond quite closely to the fluxes of the sources which dominate the cosmic X-ray background (where the slope of the extragalactic source counts breaks), demonstrating the importance of 2XMM in providing large samples at these fluxes.

Also shown in Fig. 9 is the distribution of total counts in the combined EPIC images for the same sample of 2XMM detections. As expected the distribution is dominated by low count sources, with the peak lying at ~70 counts. This plot also illustrates the effect of the targets of the XMM-Newton fields themselves which only contribute significantly, not surprisingly, above ~2000 EPIC counts.

We note that it would be possible to combine the survey sensitivity curves discussed in Sect. 9.2 and the flux distributions discussed here to construct the source counts (i.e., the $\log N - \log S$ relationship) for the 2XMM catalogue. In practice, however, the results of this exercise would have limited value due to the large uncertainties in the correct area-sensitivity corrections for the substantial number of fields included in 2XMM which contain, for example, bright objects or are subject to problematic instrumental effects. A separate paper, Mateos et al. (2008), presents the $\log N - \log S$ relationship and results for a carefully selected subset of the 2XMM fields at high Galactic latitudes.

9.4. False detection rate and likelihood calibration

The significance of the source detection in the 2XMM catalogue is characterised by the maximum likelihood parameter for the detection, L (cf. Sect. 4.4.3). Although the detection likelihood values are formally defined in terms of the probability of the detection occurring by chance, the complexity of the data processing implies that the computed likelihoods need to be carefully assessed. To investigate the calibration of the likelihood values and the expected false detection rate, we thus carried out realistic Monte-Carlo simulations of the 2XMM catalogue source detection and parameterisation process. The simulations performed were chosen to represent typical high-latitude fields without bright sources or extended X-ray emission apart from the unresolved cosmic X-ray background. The simulations include a particle background component and a distribution of X-ray point sources with uniform spectral shape drawn from a representative extragalactic $\log N - \log S$ relationship (e.g. Hasinger et al. 2001). The source spectrum assumed is a power law characterised by $\Gamma = 1.7$ with a Galactic column density $N_{\rm H} = 3 \times 10^{20}$ cm^{-2}.

The simulation creates images (and exposure maps etc.) in the five standard energy bands using the appropriate calibration information (i.e., energy- and position-dependent PSFs, vignetting, detection efficiency, etc.). The simulated data are then processed with exactly the same steps used in the actual 2XMM pipeline (Sect. 4) and the derived source parameters, such as likelihoods, were compared with the input (i.e., simulated) parameters.

Figure 10 shows the number of false detections per field derived from the simulations as a function of the minimum L for three different exposure times: 12 ks for MOS and 8 ks for pn, corresponding to around 70% of the median exposure, and three and ten times higher exposure values. Also shown is the expected false detection number n for an assumed $N_{\rm c} = 5000$ independent detection cells per field, calculated simply as $n = N_{\rm c} \,.\exp(-L)$. The value of $N_{\rm c}$ of course depends on the effective "beam-size" for EPIC observations. The value $N_{\rm c} = 5000$ we adopt is based on the area of the search box ($20'' \times 20''$, Sect. 4.4.1), corrected downwards to take into account the degradation and change of shape of the PSF off-axis. This value is a factor ~ 4 times less than would be derived from assuming the beam-size is of the order the PSF width (e.g. 15″ HEW), highlighting that this is a poorly defined quantity.

The results shown in Fig. 10 demonstrate: (i) the number of false detections per field is low even for $L \geq 6$; (ii) the dependence of the number of false detections on L is much flatter than simple expectations; (iii) the number of false detections depends on the exposure time.

For typical observations included in the catalogue (represented by the red curve in Fig. 10), the number of false detections is $\sim[1, 0.3, 0.1]$ per field at likelihood limits of $L \geq [6, 8, 10]$ respectively. These values increase to $\sim[4, 2, 1.5]$ for the longest exposure time represented in Fig. 10. For each of the three exposure times adopted, we also compared the numbers of false detections with the average number of sources detected in corresponding exposures of typical XMM-Newton high Galactic latitude fields, i.e. $\sim[60, 100, 200]$ sources per field, to derive false detection *rates*. We find that these rates have only a small dependence on the exposure time, i.e. the false detection *rate* is approximately constant at $\sim[2, 1, 0.5]$% for likelihood limits $L \geq [6, 8, 10]$ over the range of exposures investigated.

Our simulation results can be compared with the analysis presented by Brunner et al. (2008), carried out in the context of the very deep XMM-Newton observation of the Lockman Hole. Their simulations are for a detection approach similar to that presented here and their results are also broadly similar (cf. their Fig. 4 which shows a qualitatively similar dependence of false number with likelihood), albeit they are presented for different energy bands. The number of false detections in their simulations is higher, but of course corresponds to an observation with an exposure time ~100 times longer. Brunner et al. comment that the significant difference between the simulation results and simple expectations primarily originates in the multi-step detection procedure (which introduces two effective detection thresholds) and the simultaneous multi-band fitting of source positions and fluxes, both of which result in a reduction of the effective number of independent trials. The fact that the number of false detections depends on the exposure time is not in line with simple expectations, but is probably a reflection of a combination of Eddington bias and source confusion effects. The much larger than expected false detection numbers at $L > 12$ may arise from a too stringent matching criterion between the input and output sources in the simulations. Other similar studies of the false detection rate in XMM-Newton observations include Loaring et al. (2005) for the relatively deep XMM-Newton 13^{H} field and Cappelluti et al. (2007) for the COSMOS field. Both studies determined false detection rates which are somewhat higher than our estimates for 2XMM, but these can be reconciled with detailed differences in the assumptions made in these studies.

We also investigated the sensitivity of the false detection number to the background and to the assumed spectral shape. The largest differences are an increase by a factor ~2 at the lowest likelihoods ($L < 8$) for background conditions 3 times higher than typical. Assuming much softer or harder spectral shapes produces a similar increase in the false detection number, again restricted to the lowest likelihood bins.

In addition to the false detection rate and calibration of the likelihood values, these simulations also provide a means to address the issue of catalogue completeness, i.e. the effects of Poisson noise which produces a probability distribution for source detectability about the sensitivity limit. This study is beyond the scope of the current paper, but we note that completeness corrections relating to these source detection biases are expected to be small except at the lowest fluxes, cf. Georgakakis et al. (2008).

The simulation work also allows us to address the astrometric performance of the processing. Comparison of the input and output positions shows that: (i) there is no measurable average offset; (ii) the distribution of position offsets closely follows the expected statistical form (cf. Sect. 9.5), validating the statistical position error estimates. This distribution does, however, show offsets that are statistically too large for simulated sources with position errors $\leq 0.5''$. The origin of this effect is unclear, although it may be related to the discrete sampling of the PSF representation in the XMM-Newton calibration data.

Full details of the evaluation of the 2XMM catalogue with the simulations will be presented elsewhere (Sakano et al., in preparation).

9.5. Astrometric properties

In order to investigate the overall astrometric accuracy of the 2XMM catalogue, in particular the extent to which the position error estimates correctly describe the true positional uncertainty, we tested the catalogue positions against the Sloan Digital Sky Survey (SDSS) DR5 Quasar Catalog (Schneider et al. 2007) which contains 77 429 objects classified as quasars by their SDSS optical spectra. The sky density of the Sloan quasars is ~10 per square degree, and their positional accuracy is better than $0.''1$, making this an excellent astrometric reference set. This approach has the advantage that XMM-Newton is expected to detect a large fraction of all Sloan quasars in X-rays (especially at the bright magnitude limit for SDSS spectroscopy) and thus, a priori, it seems safe to assume that essentially all positional matches are actually real associations and that the SDSS provides the true celestial position of the object.

To carry out the analysis, the 2XMM catalogue was cross-correlated with the DR5 Quasar Catalog, keeping all matches within $20''$. This produced around 1600 matches, corresponding to 1121 unique 2XMM sources. The total sky area for the matches (out to $20''$ radius) was $\sim 0.2\,\mathrm{deg}^2$. Given the sky density of Sloan quasars this translates to ~2 false matches overall, or ~0.5 false matches if we use just the inner $10''$ of the distributions. We can thus be confident that the false match rate is negligible for this investigation. This is the real advantage of using Sloan quasars over other comparison catalogues.

For the astrometry evaluation a subset of these matches was used with detection likelihood $L \geq 8$, summary flag 0, off-axis angle $<13'$, and excluding extended sources. These selections reduce the total number of detection matches to 1007 (corresponding to 656 unique sources).

Figure 11 shows the distribution of the X-ray/optical position separations for each match for both the corrected and uncorrected 2XMM coordinates. As can be seen, the uncorrected separations peak at $\sim 1.''5$ and show a broad distribution out to $4''-5''$, whereas the corrected separations peak at $<1''$ and show a narrower spread. This result of course reflects the overall success of the astrometric rectification carried out as part of the processing (Sect. 4.5).

To make a more detailed comparison of the observed and expected distributions, we consider the separations normalised by the position errors. If we define $x = \Delta r/\sigma_{\mathrm{pos}}$ where Δr is the angular separation and σ_{pos} is the total position error, the expected distribution function $N(x)$ takes the form

$$N(x)\mathrm{d}x \propto x\,\mathrm{e}^{-x^2/2}\mathrm{d}x.$$

Thus comparing the empirical $N(x)$ distribution with the expected form provides a means to determine the correct σ_{pos} value. We expect σ_{pos} to have two components: σ_{stat}, the statistical error already determined in the maximum likelihood

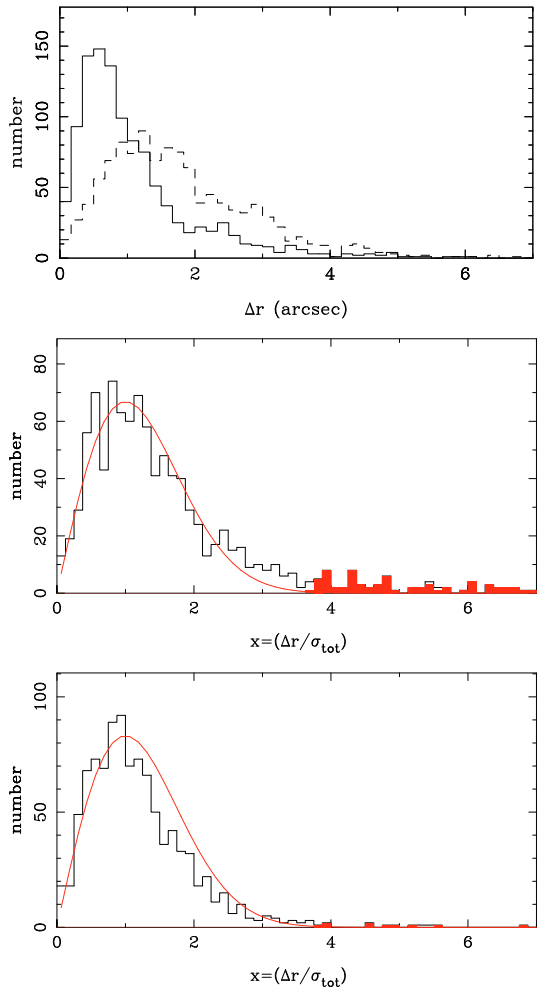

Fig. 11. *Top*: X-ray/optical position separation for each match for the corrected (solid histogram) and uncorrected (dashed histogram) XMM-Newton coordinates. *Centre*: distribution of separation sigma (x) for $\sigma_{\rm sys} = 0$. *Bottom*: distribution of separation sigma (x) for $\sigma_{\rm sys} = 0\farcs35$. For the centre and bottom plots – histogram: separation sigmas; filled histogram: outliers with $x > 3.7$ (and $\Delta r < 10''$); smooth curve: expected distribution $N(x)$ normalised to fit the peak of the distribution.

fit (Sect. 4.4.3) and a possible additional, residual component, $\sigma_{\rm sys}$ (see comment on nomenclature: footnote 12), to take into account any residual errors in the position determination and correction process, cf. Sect. 4.5. Although it is not completely obvious how $\sigma_{\rm stat}$ and $\sigma_{\rm sys}$ should be combined because the nature of the residual error is formally not known, the analysis reported here assumes Eq. (5), cf. Sect. 8.1 (other assumptions such as the linear combination of the errors provide worse fits to the distributions).

Figure 11 (centre) shows the distribution, for corrected XMM-Newton coordinates only, of the X-ray/optical position separation sigmas (i.e., $x = \Delta r/\sigma_{\rm pos}$) for the matched detection sample assuming $\sigma_{\rm sys} = 0$. Although the observed distribution is reasonably close to the expected form at low x-values, there is a long tail of outliers at $x > 3.7$ amounting to ~8% of the total sample, whereas we would expect <0.1% to lie at $x > 3.7$. More detailed investigation of these outliers shows that they are dominated by sources with low $\sigma_{\rm stat}$-values (mostly $<0\farcs5$), clearly indicating the need for an additional component, $\sigma_{\rm sys}$, of the order $0\farcs5$.

We investigated a range of possible values of $\sigma_{\rm sys}$ and found that $\sigma_{\rm sys} = 0\farcs35$ provides the best overall fit between the observed and expected distributions, as is shown in Fig. 11 (bottom). For this choice of $\sigma_{\rm sys}$ there are still more outliers at large x-values than expected if the position errors were perfectly described, but we find that at least some of these can be explained on astrophysical grounds (e.g., source confusion, lensed objects), so regard our choice as the best overall value to represent the global additional error estimate for the catalogue.

A detailed comparison between the observed and expected distributions (Fig. 11) shows that there is a deficit of points at low x-values and indeed this is true for any $\sigma_{\rm sys} > 0$. This indicates that the true value of the statistical position error, $\sigma_{\rm stat}$, is slightly overestimated by the fitting routine. Attempts to model this effect with a simple rescaling of the $\sigma_{\rm stat}$-value were not successful. We note that the typical error estimate of the rectification of the XMM coordinates is ~$0\farcs6$ with a spread from $0\farcs3$ to $>1''$. This suggests that most of the additional error component needed is related to the rectification residuals, with other effects being at a lower level. An obvious alternative approach is thus to use the explicit values of the errors determined by the rectification algorithm for $\sigma_{\rm sys}$ (which thus vary from field to field and indeed from source to source if the error in the field rotation is taken into account) instead of the empirically determined – and fixed value – described above. Overall this approach gives similar results, but gives x-values which are systematically significantly too low, implying the uncertainties derived by the rectification algorithm may also be significantly over-estimated (by up to 50%). We conclude that using a fixed value of the additional error provides the best empirical description of the data. On this basis the value $\sigma_{\rm sys} = 0\farcs35$ was adopted for the 2XMM catalogue. The total position error given in the catalogue, $\sigma_{\rm pos}$, combines the statistical and additional errors in quadrature, see Eq. (5). We note that the effect described here may be identical to that discovered through the simulation work described in Sect. 9.4. If this is the case it would imply that the residual errors associated with the rectification must indeed be rather lower than the formal estimated values overall.

We repeated the analysis described above for the *uncorrected* XMM coordinates to determine the $\sigma_{\rm sys}$-value appropriate to those XMM-Newton fields for which astrometric rectification was not possible (see Sect. 4.5). For the uncorrected XMM-Newton coordinates we determine a good fit between the observed and expected distributions for $\sigma_{\rm sys} = 1\farcs0$. This value is adopted in the catalogue for sources in those fields for which astrometric rectification was not possible.

For completeness we looked for possible correlations between outliers and the obvious XMM-Newton detection parameters (e.g., detection likelihoods, off-axis angle). Rather surprisingly no clear correlations were found, except with off-axis angle where it was noted that detections at very high off-axis values ($>15'$) were somewhat more likely to have statistically too large separations. By no means all high off-axis detections are affected in this way, however. Essentially this means that the statistical position error estimates are robust over a very wide range of detection parameters and a single additional error component provides a very adequate representation of the data. Finally we note that properties of the 2XMM/Sloan DR5 Quasar sample are reasonably representative of the whole 2XMM catalogue. There is a bias towards higher X-ray fluxes and thus lower statistical position errors, but a significant number of lower flux objects are included and the full range of total counts and likelihoods is sampled.

Table 9. Summary of the statistical comparison of the 2XMM fluxes from the EPIC cameras.

Energy band [keV] (1)	pn−M1 [%] (2)	$N_{\rm pn-M1}$ (3)	pn−M2 [%] (4)	$N_{\rm pn-M2}$ (5)	M2−M1 [%] (6)	$N_{\rm M2-M1}$ (7)
0.2–0.5	4.9 ± 1.2	785	8.4 ± 0.9	771	-0.9 ± 0.6	987
0.5–1.0	-2.4 ± 0.3	1906	-2.7 ± 0.2	1957	1.0 ± 0.3	2384
1.0–2.0	-7.6 ± 0.3	2394	-8.6 ± 0.3	2461	0.6 ± 0.2	2932
2.0–4.5	-6.1 ± 0.3	1311	-5.4 ± 0.3	1342	-0.8 ± 0.2	1552
4.5–12.0	-12.4 ± 0.7	387	-9.5 ± 0.6	408	-3.2 ± 0.4	441

(1): energy band definition in keV; (2) and (3): difference (in %) in the measured flux in pn and M1 and number of sources used in the comparison; (4) and (5): same as Cols. (2) and (3) but for pn and M2; (6) and (7): same as Cols. (2) and (3) but for M2 and M1.

9.6. Photometric properties

We have evaluated the flux cross-calibration of the XMM-Newton EPIC cameras based on the calibration used to compute 2XMM fluxes (see Sect. 4.6). To do this we performed a statistical analysis, comparing the fluxes between cameras for sources common to both, selected from the entire FOV. The parameter used to quantify the difference in flux was defined as $(S_i - S_j)/S_j$, where S_i and S_j are the fluxes of the sources in each pair of cameras (i,j).

To minimise the impact of other effects, we performed the following filtering on the comparison samples:

1. we used only point sources, as the uncertainties in the measured flux for extended sources are much higher;
2. we used only sources having at least 250 counts in the energy band and for each camera. This requirement was used to avoid Eddington bias effects (an increase in the measured flux due to statistical fluctuations);
3. we did not use sources with a 2–12 keV flux $\gtrsim 6 \times 10^{-12}$ erg cm^{-2} s^{-1} as these objects suffer from pileup and therefore their measured flux is underestimated.

The distributions obtained were fitted with a Gaussian profile, which in all cases provided a good representation of the data. The best-fit mean values obtained from each distribution are listed in Table 9.

There is an excellent agreement in the measured fluxes between the two MOS cameras, better that 5% in all 2XMM energy bands. The agreement between pn-MOS fluxes is also good, better than 10% at energies below 4.5 keV and ∼10–12% above 4.5 keV. These flux differences are in broad agreement with the results of Stuhlinger et al. (2008) who find a small excess, 5–10%, of the MOS cameras with respect to pn, using a sample of very bright on-axis sources. A more detailed analysis will be presented in Mateos et al. (2008).

9.7. X-ray hardness (colour) distributions

For each 2XMM source there are four X-ray hardness ratios (X-ray "colours") which provide a crude representation of the X-ray spectrum (cf. Sect. 4.4.3 for hardness ratio definition). In Fig. 12 we show the hardness ratio density plots for 2XMM catalogue sources at high and low Galactic latitudes. These plots are for the pn camera hardness ratios only, as they typically are better constrained. Density plots are constructed for sources which have detection likelihood $L > 8$ in the energy bands comprising each pair of hardness ratios: this means that the subsample included in each plot differs and there is an inevitable bias towards softer sources for the HR1-HR2 plot and to harder sources for the HR3-HR4 plot. Imposing the same likelihood threshold for *all* bands would produce a bias towards higher flux sources and in fact would restrict this exercise to relatively small samples from the whole catalogue. We also exclude sources with summary flag 4; a more severe restriction on the flag produces relatively small changes to the overall distributions. Overlaid on these hardness ratio density plots are spectral tracks for representative simple power law and thermal spectral models with a range of absorbing column densities.

These density plots provide an excellent statistical characterisation of the spectral properties of the catalogue sources, thus potentially providing constraints on the overall X-ray population. Although a detailed analysis is beyond the scope of the present paper, we comment here on how these match simple expectations about the underlying source populations.

For the high latitude regions of the sky, the density plot is dominated by sources with power-law spectra and column densities $N_{\rm H} \lesssim 10^{22}$ cm^{-2}, as expected from the dominant population of AGN. The fraction of AGN in 2XMM with $N_{\rm H} > 10^{22}$ cm^{-2} can be seen from these plots to be quite low. The high latitude plots also show an extension to much softer hardness ratios. The main contributors to this are likely to be coronally active stars and non-active galaxies (see comment below about the thermal spectra). Due to the bias towards softer (harder) sources in the HR1-HR2 (HR3-HR4) plots noted above, the power-law tracks overlaid have different indices to approximately match the observed density distributions.

At low Galactic latitudes, in contrast, the plots show a more complex structure (albeit the sample sizes are smaller). The overall low latitude density pattern is consistent with a large population of coronally active stars (particularly evident in the HR1-HR2 plot) with relatively soft thermal spectra together with a significant population of much more absorbed objects: background AGN together with distant accreting binaries in the Galactic plane (e.g., Hands et al. 2004). Sources with very low-temperature thermal spectra (i.e., $kT \sim 0.3$ keV) are only evident as a small component in the HR1-HR2 plot. We note that the density peak in the low latitude density plots is *not* consistent with what is expected for a distribution of single-temperature thermal spectra with a range of intrinsic temperatures. Instead the peak is much better matched by a *multi-temperature* spectrum which we have here characterised empirically as a composite three-component model with $kT = [0.3, 1, 3]$ keV with equal weighting (emission measure) of the three components. This finding is broadly consistent with the spectral properties of X-ray selected active star samples (e.g., Lopez-Santiago et al. 2007, and references therein) in which such objects typically are best-fit with two-temperature models with $kT \sim [0.3, 1]$ keV. The fact that our hardness density plots are better characterised with the ad hoc addition of a third higher temperature component

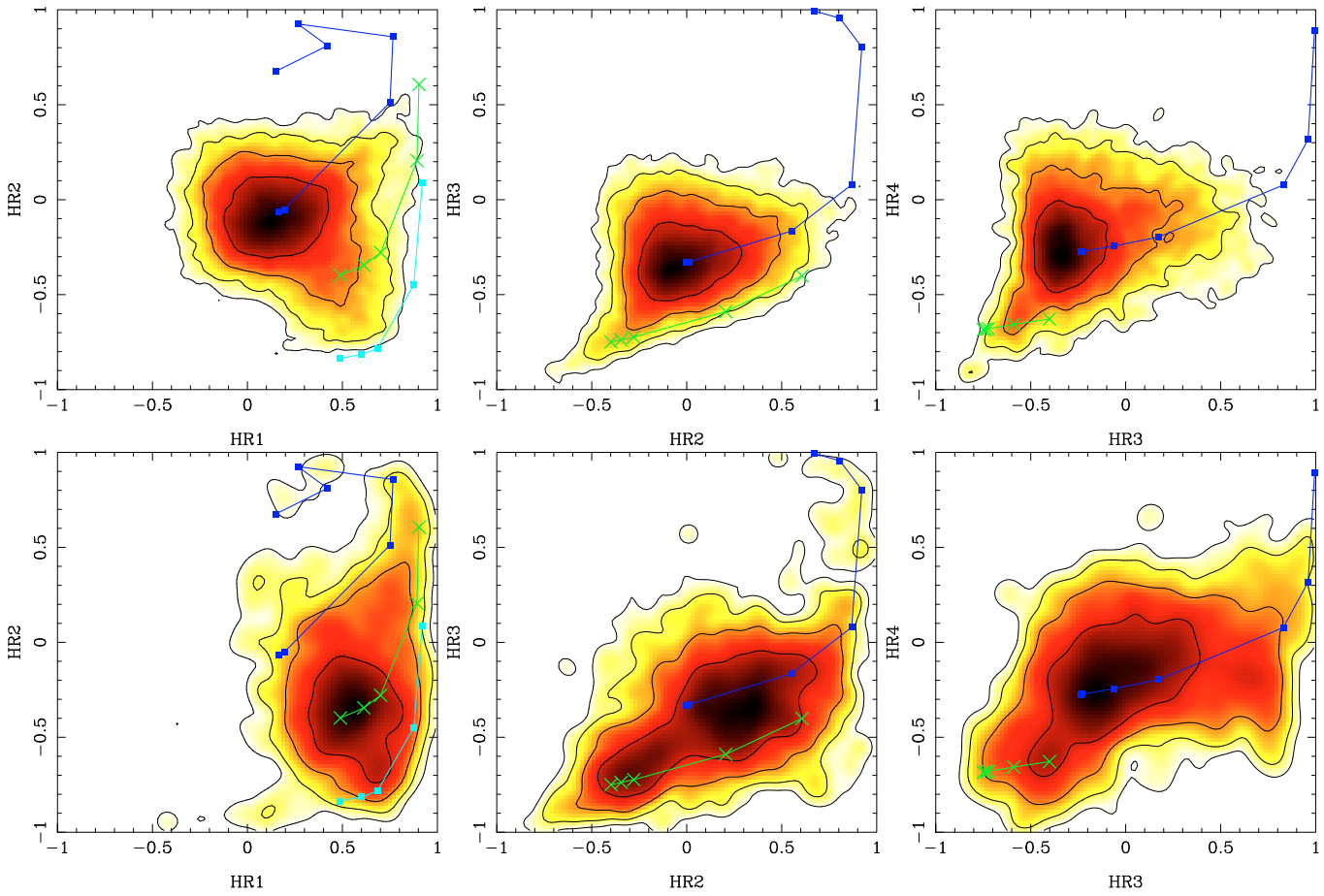

Fig. 12. *Top row*: EPIC pn X-ray hardness ratio density plots for high Galactic latitude ($|b| > 10°$) 2XMM sample. *Bottom row*: X-ray hardness ratio density plots for low Galactic latitude ($|b| < 10°$) 2XMM sample. Density is displayed on a logarithmic scale with a dynamic range of 100. The spectral tracks overlaid are for (i) power-law spectra with $\Gamma = 1.9, 1.7, 1.4$ (blue) *for the left, middle, and right panels*, respectively; (ii) thermal spectrum (APEC model) with $kT = 0.3$ keV (cyan; HR1-HR2 plot only); (iii) a composite thermal model with three components with $kT = [0.3, 1, 3]$ keV (green). In each case hardness values are shown for $N_{\rm H} = [0.03, 0.4, 1, 5, 10, 50] \times 10^{22}$ cm^{-2} (power-law model) and $N_{\rm H} = [0.01, 0.05, 0.1, 0.5, 1] \times 10^{22}$ cm^{-2} (thermal models). For each spectral track the left-most point marked corresponds to the lowest $N_{\rm H}$ value, i.e. $N_{\rm H}$ increases towards the *top right*.

clearly points to a harder component being present in a significant number of the objects contributing to the hardness density plots.

9.8. Variability characterisation

In the whole 2XMM catalogue there are 2307 detections indicated as variable (cf. Sect. 8), which relate to 2001 unique sources. Evaluation of the frequency distributions of the χ^2-probability, $P(\chi^2)$, from the time-series analysis reveals no significant systematic effects and shows the expected behaviour for the parts of the distributions dominated by random noise. For example, the frequency distribution of $P(\chi^2)$, as shown in Figs. 13b and c for the pn (the distributions for MOS1 and MOS2 are very similar), is almost constant per unit interval of probability down to low probabilities ($\lesssim$0.1). Obviously, a non-variable set of time-series would have this property across the whole probability range 0.0−1.0.

Figure 13a shows the observed frequency distribution of $P(\chi^2)_{\rm EPIC}$ compared with a simulated distribution for a non-variable set of time-series. As there are many detections with less than the full set of [pn, M1, M2] time-series, it was necessary to reproduce this incompleteness in the simulation. The numbers of detections with 3, 2, 1, or 0 $P(\chi^2)$-values are: 14 917, 11 330, 11 917, 156, respectively. The simulation was conducted by generating three vectors representing pn, M1, M2, with each element containing a uniform, random number in the range 0.0−1.0. For each element, a check was performed to see if there was a valid $P(\chi^2)$-value for the associated, real camera data; if not, the random value was set to NULL (so that the correct 'run' of valid values was mimicked in the simulations). These values simulate the expected distribution of [pn, M1, M2]-probabilities for the case of no real variability (see Fig. 13a). As expected, the resulting distributions are "flat" (on a linear scale), as discussed above. A fourth vector was then computed with the minimum simulated $P(\chi^2)$, i.e., a simulated set of $P(\chi^2)_{\rm EPIC} = \min(P(\chi^2)_{\rm pn}, P(\chi^2)_{\rm M1}, P(\chi^2)_{\rm M2})$ over all available values for each detection.

Visual inspection of samples of time-series flagged as not variable, indicated a number of cases and types of variability that were likely to have been "missed" by the 2XMM variability test, implying that the catalogue is conservative in this respect. These included relatively short-duration increases or decreases, and low-level trends/ramps.

We have compared the fraction of variable sources (or detections) to all sources (or detections) having time-series as a function of various other parameters of the catalogue. As a function of flux (specifically EPIC total-band flux), we find this

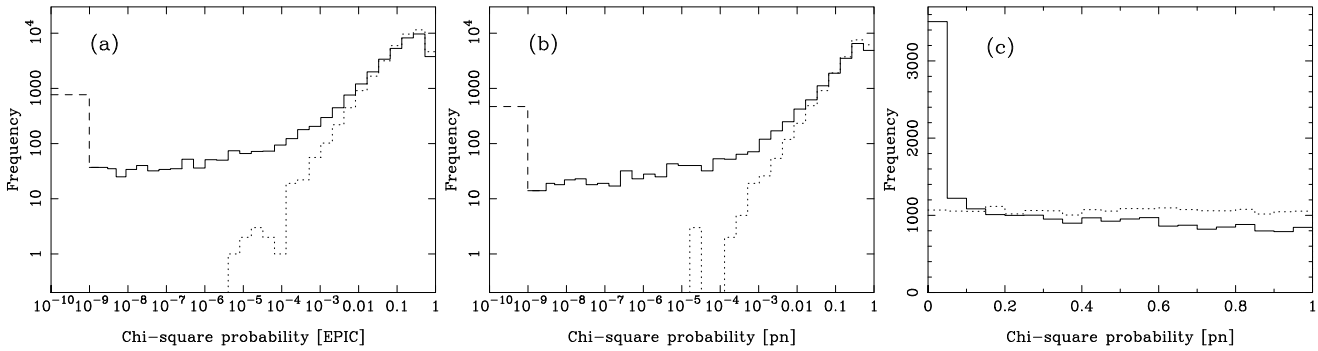

Fig. 13. **a)** Frequency distribution of $P(\chi^2)_{\rm EPIC}$, with log scales on both axes: solid line – observed; dotted line – simulation for random noise, taking into account that there is not always a complete set of 3 camera values for each detection. **b)** Frequency distribution of $P(\chi^2)_{\rm pn}$, with log scales on both axes: solid line – observed; dotted line – simulation for random noise. **c)** As **b)** but with linear scales on both axes.

fraction to be ∼25%, 10%, and 5% for fluxes $\gtrsim 10^{-10}$, $\sim 10^{-11}$, and $\lesssim 10^{-12}$, respectively. This is broadly as expected as the ability to detect variability falls towards lower fluxes.

We have also carried out an initial evaluation of the variable 2XMM sources using secure positional matches with objects in the Simbad database. From this study we estimate that, for serendipitous (i.e., non-target) sources, ∼40% are "normal" (i.e., non-degenerate) stars, ∼5% are X-ray binaries, ∼3% are cataclysmic variables and ∼5% are AGNs, plus lower percentages of objects such as GRBs. Of order 45% could not be identified from Simbad. The above figures relate primarily to the ∼1000 sources with quality summary flag values 0−2. Although this is not a definitive study as the completeness of Simbad for different object types is highly non-uniform, it does nevertheless provide confirmation of the utility of the catalogue variability characterisation to select known types of variable objects efficiently.

9.9. Extended sources

The 2XMM catalogue contains more than 20 000 entries of extended detections. The reliable detection and parameterisation of extended sources is significantly more demanding than for point-like sources because there are many more degrees of freedom in the parameter space. The relatively simple analysis approach used in the creation of the catalogue (Sect. 4.4.4) means that the catalogue contains a significant number of extended object detections that are either spurious or at least uncertain (cf. Sects. 7.2 and 7.3). The most common causes of problems with extended sources are summarised below and illustrated in Fig. 14.

Spurious detections near bright point sources: these are mostly due to inaccuracies of the PSF models, leading to inaccurate modelling of the internal background by the source fitting routine.

Confusion of point sources: pairs or multiples of point sources can be detected as one extended source since only up to two point sources are modelled simultaneously by the fitting algorithm.

Insufficient background subtraction: some spatial variations of the intrinsic background are poorly modelled by the spline map. In regions where the background is underestimated, spurious detections of extended sources are possible. (In many cases the extent parameter of these sources is at or near the maximum of the allowed range, 80″.)

Multiple detections of extended sources: the surface brightness distribution of extended sources is generally more complex than the fitted β-model. This can lead to additional detections in the wings of extended sources. The most extreme cases are observations of complex, bright extended sources (e.g., Galactic supernova remnants), leading to the detection of numerous extended sources in one field. Also, extended emission following the fitted β-model, but with an extent greater than the maximum allowed in the fit, tends to be broken up into multiple detections.

Instrumental artefacts: OOT events of piled-up sources, single reflections arcs, and scattered light from the RGA (cf. Fig. 4c) can cause both point-like and extended spurious detections.

The catalogue contains extensive detection flags (Sect. 7) which can be used to produce much cleaner extended-source samples, albeit at the expense of removing some genuine extended objects. (This is the case as the flagging scheme only provides warnings about generic problems with the analysis or the data rather than a specific assessment of the reality of each detection.) In particular the automated quality Flags 4, 5, and 6 (see Table 6) are set to warn about possible spurious detections of extended sources. The combined Flag 7 for extended sources is set if one of the Flags 4−6 is set. This flag is set for 9882 out of 20 837 detections, indicating a potential spurious fraction of about 50%. However, the rate of spurious detections is distributed very unevenly over the catalogue observations as is discussed below.

Figure 15 illustrates some of the main features of the extended source detections in the catalogue. The plot shows that there is, as expected, an overall correlation of extent likelihood with EPIC flux. The considerable scatter in the plot has three origins: (i) the observations from which the detections are drawn have a considerable range of exposure times and background values; (ii) source extent: sources with larger spatial extent have lower likelihoods at the same integrated flux; (iii) the presence of significant numbers of spurious detections. The detections with Flag 7 set show, as expected, a broader distribution than those without this flag, and a much broader distribution than for the detections with "best" summary flags (i.e., summary flag <2). This is, of course, due to the fact that spurious detections will often have implausible likelihoods for the fitted flux or correspond to very large source extent which is rare in genuine detections.

Based on the sample with "best" summary flags it is clear that there are very few reliable extended source detections with extent likelihood above ∼1000 or flux above $\sim 4 \times 10^{-13}$ erg cm^{-2} s^{-2}, highlighting the problems that the detection

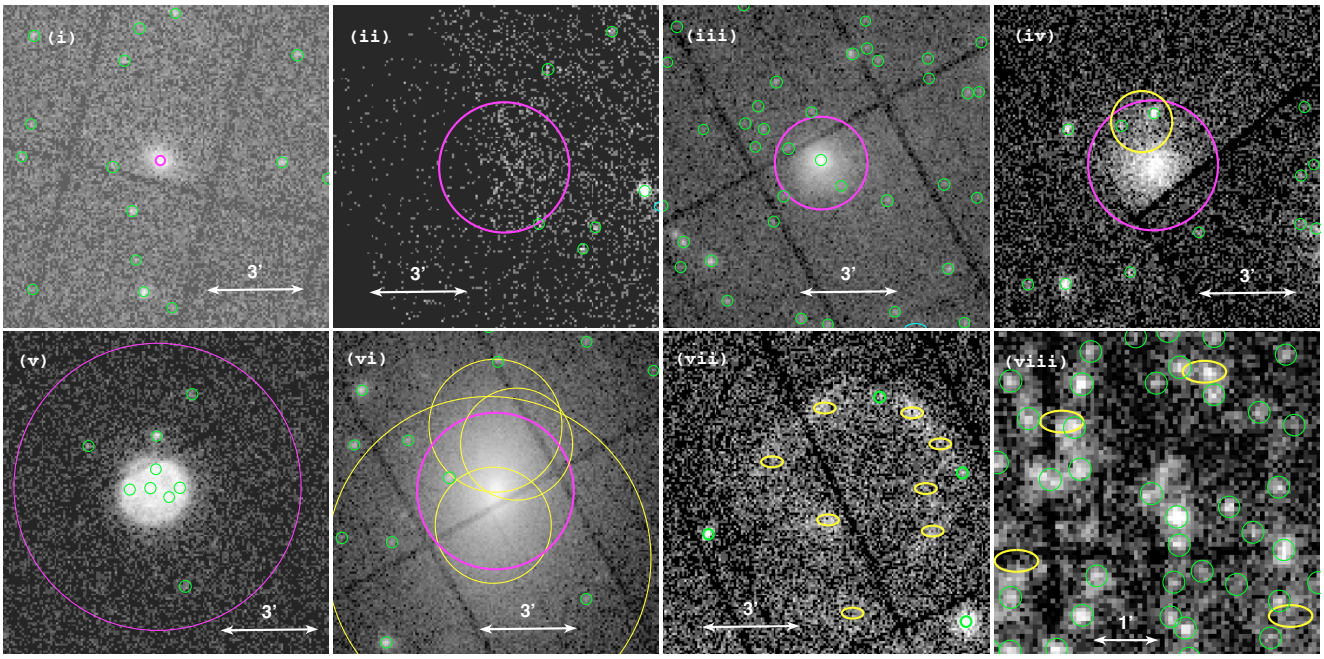

Fig. 14. Examples of extended source detections. Green circles mark point source detections. In panels (i)–(vi) the magenta and yellow circles mark real and spurious extended detections respectively, plotted with their fitted extent (i.e., core radius, see Sect. 4.4.4). In panels (vii) and (viii) the yellow ellipses indicate the position of spurious extended source detections. *Top row*: (i) a compact extended source with a small core radius; (ii) a large, low surface brightness extended source at the edge of the FOV with low likelihood but high flux (see Fig. 15); (iii) an object with a point-like core detected both as a point source as well as an extended source; (iv) a clearly extended source with a spurious detection nearby (yellow circle) which is smaller and fainter (by a factor of 45) and which therefore does not significantly affect the parameters of the real source. *Bottom row*: (v) a SNR in the LMC where intrinsic structure is detected as point sources (note that the core radius is not representative as the extended emission does not follow the β-model fitted); (vi) a bright extended source with multiple spurious detections around the centre: the core radii of these spurious detections are comparable to or greater than the extent of the real source and will thus significantly affect the parameters of the real source (note that the maximum core radius allowed in the fitting is 80″); (vii) a faint filamentary structure broken up into several extended detections where the parameters have little meaning (due to the circularly symmetric nature of the fit); (viii) a crowded region where several point sources are detected as extended due to source confusion (the algorithm is restricted to fitting at most two confused sources simultaneously).

algorithm has with bright objects[23]. Indeed the majority of reliable extended objects in this region of the diagram are the XMM-Newton targets themselves (but note that many of these have Flag 7 set which would otherwise indicate potentially spurious detections). At the highest fluxes a large fraction of the detections relate to very bright point-like targets that are incorrectly parameterised as being extended due the deficiencies of the fitting algorithm noted above.

We have investigated a small subset of the extended detections at high Galactic latitudes covered by SDSS DR6 (excluding targets). We selected detections with extent likelihood >100 and no warning flags set (i.e., summary flag 0) and evaluated their validity by examining the X-ray images visually and by searching for matches with catalogued objects. We find that less than 5% of these may be spurious extended source detections, around 40% are clearly associated with catalogued clusters or groups of galaxies and a few percent are associated with single nearby galaxies. For a further ~30% of the detections we find convincing evidence of a previously uncatalogued cluster or group of galaxies at the X-ray source location from visual inspection of the SDSS DR6 images. These results demonstrate that the overall reliability of the "best" extended source sample is high, at least at higher likelihoods, and that, as expected, the extended source sample is dominated by groups and clusters of galaxies. We have not carried out a similar exercise systematically at low Galactic latitudes but checks of selected detections demonstrate the expected associations with SNRs, HII regions, and discrete extended features in the Galactic Centre region.

[23] We also note that this is what is expected from the source counts of clusters of galaxies which are expected to dominate the extended detections, at least at high Galactic latitudes.

10. Availability of the catalogue and catalogue products

The 2XMM catalogue table itself is essentially a flat file with 246 897 rows and 297 columns (described in Appendix D). Access to the catalogue file in various formats (FITS and comma-separated-variable [CSV]) is available from the XMM-SSC catalogues web-page: http://xmmssc-www.star.le.ac.uk/Catalogue/. This XMM-SSC web-page is the primary location for information about the 2XMM catalogue. It provides links to the other hosting sites and the documentation for the catalogue. It also provides a "slimline", reduced volume version of the 2XMM catalogue, which is based on the 191 870 unique sources and contains just 39 columns. The columns in this version are restricted to just the merged source quantities, together with the 1XMM and 2XMMp cross-correlation counterparts.

Ancillary tables to the catalogue also available from the XMM-SSC web-page include the table of observations incorporated in the catalogue (Appendix B) and the target identification and classification table (Appendix C).

Associated with the 2XMM catalogue itself is an extensive range of data products such as the EPIC images from each observation and the spectra and time-series data described in Sect. 5.

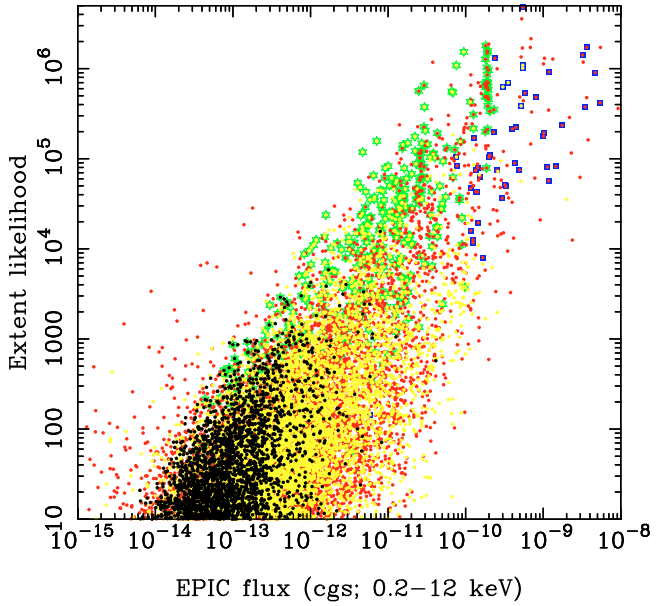

Fig. 15. Distribution of extent likelihood as a function of total-band EPIC flux for the extended source detections in the 2XMM catalogue. Red dots are potentially spurious detections with Flag 7 = T, yellow dots are detections with Flag 7 = F, black dots are the "best" sample detections with summary flag <2. Green stars mark the targets of the XMM-Newton observations classified as extended object types and blue squares targets which are object types classified as point-like. The vertical concentrations of target points at flux $\sim 3 \times 10^{-11}$ and $\sim 2 \times 10^{-10}$ erg cm^{-2} s^{-1} are real, being due to multiple detections of two different SNRs used as XMM-Newton calibration targets.

Table 10. Summary of 2XMM catalogue characteristics.

Energy range (keV; set by EPIC cameras)		0.2−12.0
Observations	*total*	3491
	pn data	2674
	MOS1 data	3384
	MOS2 data	3394
Time interval		Feb. 2000−Mar. 2007
Detections	*total*	246 897
	total $L \geq 10$	201 275
	total sum flag 0	199 359
	point-like	226 060
	extended	20 837
	with products	38 320
Unique sources	*total*	191 870
	point-like	173 066
	extended	18 804
Sky area (deg^2)	*total*[a]	~560
	net MOS1/2	~355
	net pn	~330
Median exposure time	MOS1/2	~16 000 s
(per observation)	pn	~12 500 s
Flux limit (pn) at ~10% sky	0.5−2.0 keV	~2
coverage (10^{-15} erg cm^{-2} s^{-1})	2.0−12 keV	~15
	4.5−12 keV	~35
Flux limit (pn) at ~90% sky	0.5−2.0 keV	~10
coverage (10^{-15} erg cm^{-2} s^{-1})	2.0−12 keV	~90
	4.5−12 keV	~250
Astrometric accuracy (1σ)	typical	1.5″
	best[b]	0.35″
Photometric accuracy	MOS1/2 comparison	≤5%
	pn/MOS comparison	≤10%

[a] Overlaps included; [b] limited by systematics.

These products are accessible, along with the catalogue itself, from ESA's XMM Science Archive (XSA[24]), the LEDAS[25] (LEicester Database and Archive Service) system and are being made available through the Virtual Observatory via LEDAS using AstroGrid[26] infrastructure.

LEDAS also provides access to a single HTML summary page for each detected source in the catalogue. These summary pages provide the key detection parameters and parameters of the corresponding unique source, links to other detections of the same source, thumbnail X-ray images and graphical summaries of the X-ray time-series and spectral data where these exist.

The results of the external catalogue cross-correlation carried out for the 2XMM catalogue (Sect. 6) are available as data products within the XSA and LEDAS or through a dedicated on-line database system hosted by the Observatoire de Astrophysique, Strasbourg[27].

11. Summary

We have presented the 2XMM catalogue, described how the catalogue was produced and discussed the main characteristics of the catalogue. Table 10 provides a summary of its main properties, bringing together information presented elsewhere in this paper.

2XMM is the largest X-ray source catalogue ever produced, containing almost twice as many discrete sources as either the ROSAT survey or ROSAT pointed catalogues. The catalogue complements deeper Chandra and XMM-Newton small area surveys, and probes a large sky area at the flux limit where the bulk of the objects that contribute to the X-ray background lie. The catalogue has very considerable potential, a detailed account of which lies outside the scope of this paper. In particular the catalogue provides a rich resource for generating sizeable, well-defined samples for specific studies, utilising the fact that X-ray selection is a highly efficient (arguably the most efficient) way of selecting certain types of object, notably active galaxies (AGN), clusters of galaxies, interacting compact binaries and active stellar coronae. The large sky area covered by the serendipitous survey, or equivalently the large size of the catalogue, also means that 2XMM is a major resource for exploring the variety of the X-ray source population and identifying rare source types. Although the 2XMM catalogue alone provides a powerful way of studying the X-ray source population, matching the X-ray data with, e.g., optical catalogues can offer an even more effective way to generate considerable samples of particular object types. Projects that exploit some of these characteristics are already underway.

Finally we note that, since the XMM-Newton spacecraft and instruments remain in good operational health, we can anticipate a substantial growth in the pool of serendipitous X-ray sources detected, increasing at a rate of ~35 000 sources/year. With this backdrop, further XMM-Newton catalogue releases are planned at regular intervals. The first such incremental release is planned for August 2008.

Acknowledgements. We gratefully acknowledge the contributions to this project made by our colleagues at the XMM-Newton Science Operations Centre at ESA's European Space Astronomy Centre (ESAC) in Spain. We thank Steve Sembay for useful comments and the CDS team for their active contribution and support.

[24] http://xmm.esac.esa.int/xsa/
[25] http://www.ledas.ac.uk/xmm/2xmmlink.html
[26] http://www.astrogrid.org
[27] http://amwdb.u-strasbg.fr/2xmm/home

M. Ceballos, F. Carrera and X. Barcons acknowledge financial support by the Spanish Ministerio de Educacion y Ciencia under projects ESP2003-00812 and ESP2006-13608-C02-01. The French teams are grateful to CNES for supporting this activity. In Germany the XMM-Newton project is supported by the Bundesministerium für Wirtschaft und Technologie/Deutsches Zentrum für Luft und Raumfahrt e.V. (DLR) and the Max Planck Society. Part of this work was supported by the DLR project numbers 50 OX 0201, 50 OX 0001, and 50 OG 0502. The Italian team acknowledges financial support from the Agenzia Spaziale Italiana (ASI), the Ministero dell' Istruzione, Università e Ricerca (MIUR) and the Istituto Nazionale di Astrofisica (INAF) over the last years; they are currently supported by the grant PRIN-MIUR 2006-02-5203 and by the ASI grants n.I/088/06/0 and n.I/023/05/0. UK authors thank STFC for financial support.
This research has made use of the NASA/IPAC Extragalactic Database (NED), which is operated by the Jet Propulsion Laboratory, California Institute of Technology, under contract with the National Aeronautics and Space Administration. This research has also made use of the SIMBAD database, of the VizieR catalogue access tool, and of Aladin, operated at CDS, Strasbourg, France, and of the Digitized Sky Surveys (produced at the Space Telescope Science Institute under U.S. Government grant NAG W-2166).

Appendix A: Summary of XMM-Newton and EPIC camera terminology

On-axis position: the telescope optical axes, defined by the geometry of each of the three X-ray mirror modules, is not coincident with geometrical centres of the EPIC detectors. The target of the observation is preferentially placed close to, but slightly offset from, the optical axis.

Point-Spread-Function (PSF): the telescope optics spread X-ray photons from a point source into a centrally-peaked distribution which is oversampled by the EPIC cameras. The PSF is energy-dependent and becomes broader with increasing (off-axis) angle from the telescope optical axis but also suffers a distortion which elongates the profile in the azimuthal direction.

Event patterns: an X-ray photon incident in a given CCD location causes charge deposition in several surrounding CCD pixels, often not symmetrically distributed around the central pixel. Several distinct charge distributions (patterns) are recognised as real events by the on-board processing electronics for the MOS cameras, whilst this processing takes place on the ground for the pn camera.

Out-Of-Time (OOT) events: EPIC camera exposures are composed of many short-duration frames during which the recorded events are rapidly read out and processed by the on-board electronics. The total time between frames (frame-time) depends on the observing mode but is a maximum of 73 ms for the pn and 2.6 s for the MOS. The cameras are shutterless and record data during the readout ("out-of-time") as well as the processing ("imaging"') period, leading to a faint trail of the "out-of-time" events along the readout direction which becomes obvious for bright sources (see Fig. 4c). The percentage of OOT events is a function of the ratio of the frame readout time to the frame integration time for a given mode. The highest percentage of OOT events at 6.3% is for the pn full frame mode, while it never exceeds 0.5% for the MOS.

Pileup: for bright sources, pixels in the core of the PSF can receive multiple X-ray photons during an integration frame. The on-board processing electronics cannot recognise them as distinct events within that frame and either treats them as a single event with higher energy or rejects them entirely if the resultant pixel pattern of the combined event lies outside the pre-defined X-ray pattern library. As a result the recorded counts are lower in the core of the source profile, producing a flattening or even depression of the source profile (see Fig. 4c). In addition, it has an impact on the spectral profile (i.e., a hardening of the spectrum).

Optical loading: the EPIC cameras (more so the MOS detectors) are also sensitive to optical photons so that optically bright objects generate recordable events in EPIC images (Lumb 2000, and references therein). The level of contamination depends on the filters used and the optical brightness of the object. In most observations the filter used is conservatively selected to minimise this effect. Note that in the case of the pn some apparently very soft sources are affected by optical loading.

RGA scattered light: scattering of incident X-rays by the RGAs in the two telescope modules that feed the MOS cameras causes a diffuse bright narrow band in the X-ray images which is detectable for bright X-ray sources (see Fig. 4c).

Good-Time-Interval (GTI): data from EPIC camera frames can be accepted or rejected according to the state of various housekeeping and science parameters, e.g., spacecraft attitude stability and particle background level. The 'GTI's are the time periods during which the parameter(s) being monitored are within the acceptable thresholds.

A more detailed description of the instruments can be found in the on-line version of the XMM User Handbook (Ehle et al. 2007) and on the ESAC documentation web-pages for calibration[28].

Appendix B: Observation summary table

Table D.1 presents the observations and exposures included in 2XMM and is available at the CDS as well as at the XMM-SSC catalogue web-page (cf. Sect. 10). The columns in this table are as follows.

Column 1: satellite revolution number (consecutive in time).

Column 2: observation number (10 digit ID).

Column 3: ODF version number.

Columns 4 and 5: nominal field right ascension and declination (J2000) in degrees.

Column 6: target name (20 characters).

Column 7: quality classification of the whole observation based on the area flagged as bad in the manual flagging process as compared to the whole detection area, see Sect. 7.4. 0 means nothing has been flagged; 1 indicates that 0% < area < 0.1% of the total detection mask has been flagged; 2 indicates that 0.1% ≤ area < 1% has been flagged; 3 indicates that 1% ≤ area < 10% has been flagged; 4 indicates that 10% ≤ area < 100% has been flagged; and 5 means that the whole field was flagged as bad.

Column 8: number of detections in this field.

Column 9: number of detections in this field that have not received manual Flag 11 and are considered to be "good".

Column 10: number of the pn exposures merged for the source detection (cf. Sect. 4.1).

Column 11: filter of the pn exposures: Tn1 stands for Thin1, Tn2 for Thin2, Med for Medium, and Tck for Thick.

Column 12: observing mode (cf. Table 1) of the pn exposures.

Column 13: total exposure time of the pn exposures in seconds.

Columns 14–17: same as Cols. 10−13 but for MOS1.

Columns 18–21: same as Cols. 10−13 but for MOS2.

[28] http://xmm2.esac.esa.int/external/xmm_sw_cal/calib/documentation/index.shtml

Appendix C: Target identification and classification procedures

In the following are described the procedures adopted to identify and classify the targets of each XMM-Newton observation included in the 2XMM catalogue. The results of this exercise, summarised in Table D.2, are available at the CDS as well as at the XMM-SSC catalogue web-page (cf. Sect. 10).

As any attempt to identify and classify a target is subjective and likely to be incomplete (only the investigators of that observation know all the details), two different approaches were chosen to give the user a choice regarding detail and reliability: on the one hand some formal information associated with an observation is provided; on the other hand, a manual classification scheme tries to supply interpretation of sometimes ambiguous target names and to directly identify associated 2XMM detections.

C.1. Formal target identification

There are three kinds of coordinates associated with each observation:

1. the median of the spacecraft attitude ("pointing direction", independent of the instrument) usually points to approximately the same position on the detectors and defines best the centre of the FOV (this is given in Table D.1);
2. the proposal position refers to the position given by the observer; this position is placed at a specified detector location which depends on the prime instrument (EPIC or RGS) as indicated by the observer and which avoids chip gaps, dead spots etc., unless an offset is indicated by the investigator;
3. the XSA gives the coordinates of the prime instrument viewing direction which are corrected for the star tracker mis-alignment.

In most cases, the proposal position is the best representative of the target object as chosen by the investigators. However, there are cases where the actual target object is deliberately off-set from the proposal position, or the proposal position is not very accurate. The latter can be due to catalogue errors, positions with large uncertainties (e.g., gamma ray sources), or an error by the observer. In cases where more than one object is the target the proposal position can either be located on one of the objects or between them. In a few cases, the image was not obtained at the proposed position due to a slew failure or a "Target of Opportunity" (ToO) observation that was not properly registered in the ODF.

The XSA coordinates are usually near the centre of the field and/or the target but do not represent the target position as well as the proposal position.

The target identification table (Appendix C.5) lists the proposal and XSA positions together with the proposal category and proposal program information as given in the XSA. The latter provide a coarse classification of the target as determined by the observer. Note though, that the proposal category of calibration observations are often meaningless since they are often instrument related for which there is no particular proposal category.

C.2. Manual target identification

In many ways the target name as given in the proposal gives a better indication of the field content than the coordinates since a target can comprise more than one object or it may be diffuse emission that can only be detected in the spectra of background objects. In other words, if a target name can be resolved by online data bases like Simbad and NED one can easily derive more information about that object, e.g., object type, other names, or references.

On the other hand, an XMM-Newton target name can be descriptive or refer to a personal choice of the observer, it can be abbreviated, or additional information is added. It was therefore necessary to "interpret" many of the target names before Simbad could recognise them.

The target identification table lists therefore, next to the XMM-Newton target name, the best estimate of the Simbad-recognisable name where possible (usually very close to the given target name), together with the Simbad coordinates[29] and Simbad object type for classification purposes. In cases where Simbad gives more than one object type, the one closest to the proposal category was given. Where no Simbad name could be identified a NED identification may be given instead, and where possible an estimated object type based on the proposal information was given.

For the use of the catalogue, however, it is most helpful to know which and how many sources are "targets" and therefore not serendipitous. The observations are thus classified by their field content (i.e., target classification; see Fig. 4 for some examples), using the following categorisation:

- a point or point-like source, that is, a single detection in the catalogue (excluding spurious detections);
- an extended source (the target can be the detection of the extended emission as well as point sources associated with it, e.g., galaxies in a cluster);
- a field, that is, all detections are potential targets (e.g., distant AGNs);
- diffuse emission; the detections in such a field are considered to be all serendipitous but the *location* of the field was chosen specifically by the observer because of the presence of the – often large-scale – diffuse emission.

or a combination of these. Occasionally the field is totally serendipitous due to operational issues. For fields that could not be easily classified, the content is "unknown". The class of extended targets was further divided as follows:

- small extended source (i.e., well within the FOV) with a radius of $<3'$ (covering roughly 3% of the full FOV);
- large extended source with a radius of $>3'$ and often extending beyond the FOV;
- extended source of undetermined radius: these are either not detected, not identifiable (more than one object fitted the description), or offset and beyond the edge of the FOV.

In cases where one or two point sources are the target, the catalogue detection IDs (for a match within $\sim 10''$) are given as well. In cases of extended targets a catalogue detection ID is only given if the match is unambiguous and the centre of the extended emission well represented by the XMM-Newton detection (the parameters of the detection, however, may be unreliable). In a few cases a positive identification could be achieved through another but deeper observation of the same target.

Because neither the formal nor the manual classification can be perfect in every case, the table also lists, for quick reference, an indicator for the positions (proposal or Simbad) which best represents the target (subject to changes and improvements in Simbad). In some cases both positions were deemed to be

[29] Note that Simbad frequently up-dates its information and the coordinates given here may be out of date.

equally viable (e.g., in field observations or large offsets of extended objects) and no preference is given in the table.

C.3. Problem cases

Not all targets fit unambiguously into the field content classes. In a few cases where no decision could be made the target was classified as "unknown". Otherwise the following guidelines were used.

Galaxies: a galaxy was classified as "point source" when the emission from the (active) nucleus was dominant. It was classified as "extended" when either diffuse emission was apparent or if the galaxy was large enough for discrete X-ray sources in the galaxy to be resolved (in case of doubt a comparison was made with an optical image downloaded from the DSS[30]) or if the galaxy was detected as a single point source in the catalogue but it clearly consisted of several (unresolved) sources.
In two cases, a "field" classification was preferred: observations of the M31 halo and offset pointings of M 33. In both cases the galaxy is considerably larger than the FOV. Note that the observations of the centre of M 31 (often called M 31 core) are classified as "large extended" instead since the field includes diffuse emission.

Galaxy clusters: galaxy clusters usually show X-ray emission from the intracluster gas as well as emission from some of the galaxies within that cluster. Most galaxy clusters were classified as "large". Exceptions are distant clusters which are significantly smaller than $r = 3'$ and where no point sources could be discerned within the diffuse emission.

Galaxy groups: galaxy groups have fewer members than galaxy clusters. In many cases there is no detectable intracluster emission and the X-ray images show only emission from some of the members. In some cases there is a prominent galaxy in the centre with a large X-ray halo. Despite this diversity it was preferred to classify all groups in the same way as galaxy clusters, that is, as extended emission, mixed with point or other extended sources.

Extragalactic point sources: in a few cases a bright X-ray source within a galaxy was the target (e.g., "super Eddington" sources); these were treated like AGNs, that is, if no galaxy emission could be discerned the target was classified as "point source", otherwise as "extended".

Mixed targets: examples for mixed targets are a particular galaxy within a galaxy cluster or a Central Compact Object in a SNR. These were classified by the "larger" target, that is, in the examples given the class would be "extended", while the Simbad object type is likely to refer to the point(-like) source. There are a number of cases where such a connection was not obvious or could not be easily determined (e.g., a connection between a quasar and a galaxy cluster which may be hosting the quasar or simply be superimposed in the line-of-sight) and the class refers to the quoted object only. In case of a calibration observation the object is more likely to be chosen for its own properties and not for its possible connection/interaction with the environment.

Solar system objects: there are a number of observations of planets or comets in our solar system. A special object type, "com" for "comet" and "plt" for "planet", is listed for these. The field classification depended on what was visible in the image, e.g., if there was visible (and detected) diffuse emission in case of a comet, or if a planet was observed long enough to produce a elongated trace on the image (the pipeline processing corrects for any attitude shift so that a fixed point in the sky is always at the same location in the image).

[30] The STScI Digitized Sky Survey.

Table C.1. Proposal category given by the XSA.

Class	Description	Percentage
I	Stars, White Dwarfs and Solar System	16%
II	White Dwarf Binaries, Neutron Star Binaries, Cataclysmic Variables, ULXs and Black Holes	15%
III	Supernovae, Supernova Remnants, Diffuse Emission, and Isolated Neutron Stars	14%
IV	Galaxies and Galactic Surveys	9%
V	Groups of Galaxies, Clusters of Galaxies, and Superclusters	14%
VI	Active Galactic Nuclei, Quasars, BL Lac Objects, and X-ray Background	23%
VII	X-ray Background and Surveys	8%

Table C.2. Target / field content classification.

Class	Description	Percentage
p	point or point-like source	50%
s	small extended ($r < 3'$)	10%
l	large extended ($r > 3'$)	22%
e	extended source of unknown extent	0.7%
f	"field" (all detections are potential targets)	12%
x	"X-ray shadow experiment" and similar, that is, only the spectra of fore- and background objects are of interest (though the location of the field should be considered as "target")	2.5%
t	two clearly identified targets (e.g., a double star)	0.4%
n	there is no target associated with the field	0.2%
u	unknown target, i.e., the target could not be classified or is of unknown nature	2%

C.4. Target classification

There are 3491 fields in total in the 2XMM catalogue. For 3044 fields (87%) a Simbad name could be found, and in 53 cases (1.5%) a NED identification is given. Of the remaining 394 fields only 56 (1.6%) do not have an estimated object type.

About 10% of the observations were obtained for calibration purposes, and 3% are ToO observations. Table C.1 lists the distribution of the proposal category for 2XMM observations, and Table C.2 gives the same for the field content classes. The ratio of point source to extended source to field observation is roughly 5:3:1.

For best results on identifying target objects in the catalogue, it is recommended to use both the field content class as well as the Simbad object type.

C.5. Target table

The columns in Table D.2, which is available at the CDS as well as at the XMM-SSC catalogue web-page (cf. Sect. 10), are as follows.

Column 1: satellite revolution number (consecutive in time).
Column 2: observation number (10 digit ID).

Column 3: a star indicates if there is a note for this observation or for this proposal-ID (first 6 digits of an observation, referring to several observations for this proposal) as detailed below.

Column 4: the source number per observation of the identified target taken from the column SRC_NUM in the catalogue.

Column 5: the detection ID of the identified target taken from the column DETID in the catalogue.

Column 6: field classification as described in Table C.2.

Column 7: coordinate preference between proposal position and Simbad position, depending on which defined the target better; in case of offset positions (usually indicated in the field name from the proposal, Col. 12) no preference is given.

Column 8: proposal category as taken from the XSA as described in Table C.1 (note that some of the calibration observations are not properly classified).

Column 9: proposal program as taken from the XSA: GO stands for Guest Observer, Cal for Calibration, ToO for Targets of Opportunity, Cha for Co-Chandra, ESO for Co-ESO, Trig for Triggered, and Large.

Columns 10 and 11: right ascension and declination (J2000) in degrees as given in the proposal (taken from the RA_OBJ and DEC_OBJ keywords in the attitude time-series file).

Column 12: field name as given in the proposal (taken from the OBJECT keyword in the calibration index file).

Columns 13 and 14: right ascension and declination (J2000) in degrees as extracted from Simbad using the Simbad name given in Col. 16.

Column 15: object type as given by Simbad. If no Simbad object is given a type was estimated. Additional types not recognised by Simbad are: XRN for X-ray reflection nebula, sfr for star forming region, plt for planet, and com for comet.

Column 16: modified field name which Simbad recognises (and can be used in a script), except for 53 cases that have a name recognised by NED (indicated with "[ned]" after the name). Modifications include dropping offset indicators, completing coordinates, and adjusting the prefix to a recognised convention as described in Simbad's dictionary of nomenclature.

Columns 17 and 18: right ascension and declination (J2000) in degrees as given in the XSA; they represent the prime instrument viewing direction (median value) and are corrected for the star tracker mis-alignment.

A list of observations (10 digits) or proposal-IDs (6 digits) in numerical order with special remarks as indicated in Col. 3 of the table follows.

0002740101: CFHT-Pl-12 appears to be the name of a CFHT plate, and the proposal abstract suggests that this is a field observation.

0002970401: the coordinates of the proposal position and image do not agree. The Observation Log Browser web-page at ESAC refers to an "earth limb test". The field of the observation is therefore as a whole serendipitous.

0008820401: the observation of HD 168112 was replaced by a ToO observation of GRB 020321 which, however, was not registered in the ODF.

004534: this is a double star but the X-ray detection is not at the Simbad position, and the field classification is ambiguous.

0075940101: Simbad recognises the field name "30 Ari" but returns two objects (30 Ari A and 30 Ari B). Due to the ambiguity no Simbad name and coordinates are given.

0093550401: this observation was intended to have Z And as a target but due to an operational issue a different position was observed. The field of the observation is therefore as a whole serendipitous.

0094360201: there seems to be an error in the proposal coordinates in the proposal; the field of the observation is therefore as a whole serendipitous.

0094380101: the observation of 1ES1255+244 was replaced by a ToO observation of GRB 011211 which, however, was not registered in the ODF.

0094530401: the observation has a large offset observation from 3C192.

0106860101: there is a source at the proposal position, however, it is possibly only a spurious extended detection, and therefore no source ID is given.

010806: the field name is AXAF Ultra Deep Field; this appears to be the same as the Hubble Ultra Deep Field with very similar coordinates (53.1625, −27.7914).

0109060201: ambiguous because target name is not precise enough.

010986: the target name is A 189 but the proposal abstract indicates that NGC 533 group is the object. It is not obvious whether both are target.

0111520301: this is a ToO observation of GRB 010220, the field name as given in the proposal is wrong.

0112200601: unclear whether the extended emission around the pulsar is connected to it, the field classification is therefore "unknown".

0112200701: unclear whether the extended emission around the pulsar is connected to it, the field classification is therefore "unknown".

0112201101: pulsar is located in SNR W44 (cf. proposal-ID 008327), and extended emission is detected; the field classification is taken to be the same as for proposal-ID 008327.

011226: the target is a merging galaxy cluster, A399/A401. There are four observations in different offset positions. The Simbad column lists for each observation the cluster that is nearer to the centre of the FOV, where possible.

011305: the proposal abstract mentions clumpy sources in the neighbourhood of pulsars, and the field classification is somewhat ambiguous (with respect to actual detections).

0135960101: the proposal abstract describes the object as X-ray reflection nebula. There is no Simbad type for that but it seems appropriate to use.

0141610601: the Simbad position appears to be wrong (the coordinates in the name were assumed to be B1950 and converted to J2000 coordinates).

014363: this is a double star but the X-ray detection is not at the Simbad position, and the field classification is ambiguous.

0149630301: the proposal refers to LMC1 as supergiant shell, while Simbad knows only a symbiotic star named LMC1. Instead Simbad knows the supergiant shell as LMC-SGS 1.

0154750401: both the proposal position and the Simbad position are offset from the identified source. The correct identification of this source comes from other observations of the same object (proposal-ID 020100).

0154750301: though the proposal position and Simbad position are not centred on the source identification given, the identification seems unambiguous (note that the Simbad position is not very precise which would explain the offset).

0201270101: the Simbad position appears to be wrong (the coordinates in the name were assumed to be B1950 and converted to J2000 coordinates).

0202940201: the declination is wrong, the field of the observation is therefore as a whole serendipitous.

0203540901: from the field name and proposal abstract it is not clear whether this is a field or point-source observation.
0204010101: the target is three point sources.
020422: the field name is a composite of several target names.
020619: according to the proposal abstract the target type is an X-ray compact source.
021047: this is an observation of a super-bubble; the field classification is ambiguous ("x" or "l").
0303670101: the proposal abstract indicates that this is an observation of two galaxy groups, the Simbad name is given for the first name only.
0304050101: it is not clear if this is a point source or a small extended source.

Appendix D: Catalogue columns

The catalogue contains 297 columns. Each detection was observed with up to three cameras. For the source detection, the total energy range (0.2−12 keV) was split into five sub-bands as well as the XID wide-band (0.5−4.5 keV), see Table 3. As a result, some of the source parameters (like count rates or fluxes) are given for each camera and band as well as for the combined cameras (EPIC) and total band. The column names reflect this by using a two-letter prefix to indicate the camera [ca = EP, PN, M1, M2]; in case of parameters that refer to a unique source rather than an individual detection (Sect. 8.1) the prefix [SC] is used (it stands for "source"). Following the prefix comes an energy band indicator where applicable (b = 1, 2, 3, 4, 5, 8, 9). Entries are NULL when there is no detection with the respective camera (that is, the detector coverage of the detection weighted by the PSF, MASKFRAC, <0.15).

In the following, a description for each column is given. The name is given in capital letters, the FITS data format in brackets, and the unit in square brackets. If the column originates from a SAS task[31], the name of the task follows.

For easier reference the columns are grouped into seven sections.

D.1. Identification of the detection

Next to the various identifications, cross matches with the 1XMM and 2XMMp catalogues are given here. There are 9 columns in this section.

DETID (J): a consecutive number which identifies each entry (detection) in the catalogue.

SRCID (J): a unique number assigned to a group of catalogue entries which are assumed to be the same source. To identify members of the same group the distance in arcseconds between each pair of sources was compared on the 3σ-level of both positional errors. A maximum distance of 7″ was assumed, which was reduced to 0.9 · DIST_NN (distance to the nearest neighbour) where necessary. See Sect. 8.1 for a more detailed description. The combined parameters for the unique sources are described in Sect. D.7.

IAUNAME (21A): the IAU name assigned to the unique SRCID.

SRC_NUM (J), SAS task `srcmatch`: the (decimal) source number in the individual source list for this observation as determined during the source fitting stage; in the hexadecimal system it identifies the source-specific product files belonging to this detection.

MATCH_1XMM (21A): the IAU name of the closest 1XMM source within r = 3″, cf. Sect. 8.1.

SEP_1XMM (E) [arcsec]: the distance between this source and the matched 1XMM source, MATCH_1XMM.

SRCID_2XMMP (J): the unique source ID of the closest 2XMMp source within r = 3″, cf. Sect. 8.1.

MATCH_2XMMP (22A): the IAU name of the closest 2XMMp source, cf. Sect. 8.1.

SEP_2XMMP (E) [arcsec]: the distance between this source and the matched 2XMMp source, MATCH_2XMMp.

D.2. Details of the observation and exposures

There are 11 columns in this section which covers the meta-data of a detection. Details on XMM-Newton filters and modes can be found in the XMM User Handbook (Ehle et al. 2007).

OBS_ID (10A): the XMM-Newton observation identification.

REVOLUT (4A) [orbit]: the XMM-Newton revolution number.

MJD_START (D) [d]: modified Julian Date (i.e., JD−2 400 000.5) of the start of the observation.

MJD_STOP (D) [d]: modified Julian Date (i.e., JD−2 400 000.5) of the end of the observation.

OBS_CLASS (J): quality classification of the whole observation based on the area flagged as bad in the manual flagging process as compared to the whole detection area, see Sect. 7.4. 0 means nothing has been flagged; 1 indicates that 0% < area < 0.1% of the total detection mask has been flagged; 2 indicates that 0.1% ≤ area < 1% has been flagged; 3 indicates that 1% ≤ area < 10% has been flagged; 4 indicates that 10% ≤ area < 100% has been flagged; and 5 means that the whole field was flagged as bad.

PN_FILTER (6A): PN filter. The options are Thick, Medium, Thin1, and Thin2, indicating the degree of the optical blocking desired.

M1_FILTER (6A): M1 filter. The options are Thick, Medium, and Thin1, indicating the degree of the optical blocking desired.

M2_FILTER (6A): same as M1_FILTER but for M2.

PN_SUBMODE (23A): PN observing mode. The options are full frame mode with the full FOV exposed (in two sub-modes), and large window mode with only parts of the FOV exposed (Sect. 3.1).

M1_SUBMODE (16A): M1 observing mode. The options are full frame mode with the full FOV exposed, partial window mode with only parts of the central CCD exposed (in different sub-modes), and timing mode where the central CCD was not exposed ("Fast Uncompressed"), see Sect. 3.1.

M2_SUBMODE (16A): same as M1_SUBMODE but for M2.

D.3. Coordinates

The catalogue lists rectified ("external") equatorial and Galactic coordinates as well as uncorrected ("internal") equatorial coordinates. Two independent error estimates are combined into a third error column. There are 9 columns in this section.

RA (D) [deg], SAS task `evalcorr`: corrected right ascension of the detection (J2000) after statistical correlation of the `emldetect` coordinates, RA_UNC and DEC_UNC, with the USNO B1.0 optical source catalogue. In cases where the cross-correlation is determined to be unreliable no correction

[31] The documentation on SAS tasks are available through the public XMM-SAS distribution from the ESAC web pages.

is applied and this value is therefore the same as RA_UNC (Sect. 4.5).

Dec (D) [deg], SAS task `evalcorr`: corrected declination of the detection (J2000) after statistical correlation of the `emldetect` coordinates, RA_UNC and DEC_UNC, with the USNO B1.0 optical source catalogue. In cases where the cross-correlation is determined to be unreliable no correction is applied and this value is therefore the same as DEC_UNC (Sect. 4.5).

POSERR (E) [arcsec]: total position uncertainty calculated by combining the statistical error, RADEC_ERR, and the "systematic" error, SYSERR, as follows:

$$\mathrm{POSERR} = \sqrt{\mathrm{RADEC\_ERR}^2 + \mathrm{SYSERR}^2}.$$

LII (D) [deg], SAS task `evalcorr`: galactic longitude of the detection corresponding to the (corrected) coordinates RA and Dec.

BII (D) [deg], SAS task `evalcorr`: galactic latitude of the detection corresponding to the (corrected) coordinates RA and Dec.

RADEC_ERR (E) [arcsec], SAS task `emldetect`: statistical 1σ-error on the detection position (RA_UNC and DEC_UNC).

SYSERR (E) [arcsec]: the estimated "systematic" 1σ-error on the detection position. It is set to be $0\farcs35$ if the SAS task `eposcorr` resulted in a statistically reliable cross-correlation with the USNO B1.0 optical catalogue, otherwise the error is $1\farcs0$ (Sect. 4.5).

RA_UNC (D) [deg], SAS task `emldetect`: right ascension of the source (J2000) as determined by the SAS task `emldetect` by fitting a detection simultaneously in all cameras and energy bands (Sect. 4.4.3).

DEC_UNC (D) [deg], SAS task `emldetect`: declination of the source (J2000) as determined by the SAS task `emldetect` by fitting a detection simultaneously in all cameras and energy bands (Sect. 4.4.3).

D.4. Detection parameters

This section lists 223 columns. The fitted and combined detection parameters as well as auxiliary information are taken directly from the source lists created by the SAS tasks `emldetect` and `srcmatch`.

Instead of listing *each* column, descriptions of the general parameter (and their errors) are given followed by an indicator for which bands and camera combinations this parameter is available. Most parameters were determined by the SAS task `emldetect` which is described in detail in Sect. 4.4, while some others were derived by the SAS task `srcmatch`. XID-band parameters are derived in a separate `emldetect` run and are therefore single-band values which ensures a better handling of the error values.

ca_b_FLUX and *ca_b_FLUX_ERR*: (E) [erg cm^{-2} s^{-1}], SAS tasks `emldetect, srcmatch`: Fluxes are given for all combinations of ca = [EP, PN, M1, M2] and b = [1, 2, 3, 4, 5, 8, 9]; they correspond to the flux in the entire PSF and do not need any further corrections for PSF losses.

For the individual cameras, single-band fluxes are calculated from the respective band count rate using the filter- and camera-dependent energy conversion factors given in Table 4 and corrected for the dead time due to the read-out phase. These can be 0.0 if the detection has no counts. The errors are calculated from the respective band count rate error using the respective energy conversion factors.

Total-band fluxes and errors for the individual cameras are the root-sum-squared values of the fluxes and errors, respectively, from the bands 1−5.

The EPIC flux in each band is the mean of the band-specific detections in all cameras weighted by the errors, with the error on the weighted mean given by

$$\mathrm{EP\_b\_FLUX\_ERR} = \sqrt{1.0/\sum 1/\mathrm{ca\_b\_FLUX\_ERR}^2},$$

where ca = [PN,M1,M2].

ca_b_RATE and *ca_b_RATE_ERR* (E) [count/s], SAS task `emldetect`: Count rates and errors are given for all combinations of ca = [PN, M1, M2] and b = [1, 2, 3, 4, 5, 8, 9] as well for ca = [EP] and b = [8, 9].

The single-band count rate is the band-dependent source counts (see ca_b_CTS) divided by the exposure map, which combines the mirror vignetting, detector efficiency, bad pixels and CCD gaps, and an OOT-factor (Out Of Time) depending on the PN modes. The source counts and with it the count rates were implicitly background subtracted during the fitting process. They correspond to the count rate in the entire PSF and do not need any further corrections for PSF losses. Note that rates can be 0.0 (but not negative) if the source is too faint in the respective band to be detectable.

Total-band count rate for each camera is calculated as the sum of the count rates in the individual bands 1−5.

The EPIC rates are the sum of the camera-specific count rates in the respective band.

ca_b_CTS and *ca_b_CTS_ERR* (E) [count], SAS task `emldetect`: Source counts and errors are given for ca = [EP, PN, M1, M2] and b = [8].

The single-band source counts (not given in the catalogue) are derived under the total PSF (point spread function) and corrected for background. The PSF is fitted on sub-images of $r = 60''$ in each band, which means that in most cases at least 90% of the PSF (if covered by the detector) was effectively used in the fit.

Combined band source counts for each camera are calculated as the sum of the source counts in the individual bands 1−5.

The EPIC counts are the sum of the camera-specific counts.

The error is the statistical 1σ-error on the total source counts of the detection.

ca_b_DET_ML (E), SAS task `emldetect`: maximum likelihoods are derived for all combinations of ca = [PN, M1, M2] and b = [1, 2, 3, 4, 5, 8, 9] as well for ca = [EP] and b = [8, 9].

The single-band maximum likelihood values stand for the detection likelihood of the source, $L = -\ln P$, where P is the probability the detection is spurious due to a Poissonian fluctuation. While the detection likelihood of an extended source is computed in the same way, systematic effects such as deviations between the real background and the model, have a greater effect on extended sources and thus detection likelihoods of extended sources are more uncertain.

To calculate the maximum likelihood values for the total band and EPIC the sum of the individual likelihoods is normalised to two degrees of freedom using the function

$$L = -\ln\left(1 - P_\Gamma\left(\frac{\nu}{2}, L'\right)\right) \quad \text{with} \quad L' = \sum_{i=1}^{N} L_i,$$

where P_Γ is the incomplete Gamma function, N is the number of energy bands involved, ν is the number of degrees of freedom of the fit ($\nu = 3 + N$, if the source extent is a fitted parameter, see Sect. 4.4.4, and $\nu = 2 + N$ otherwise).

Table D.1. XMM-Newton observations and exposures included in the 2XMM catalogue.

Rev	Obsid	ODF	RA [J2000] [deg]	Dec [deg]	Target	Obsclass	#det	#good	PN_exp [s]	PN_ft	PN_md	PN_tm	M1_exp [s]	M1_ft	M1_md	M1_tm	M2_exp [s]	M2_ft	M2_md	M2_tm
0088	0125310101	004	0.098292	–25.101528	Abell 2690	1	94	93	PN[1]	Med	PFW	21596	M1[1]	Med	PFW	19642	M2[1]	Med	PFW	19 203
...																				
1009	0302580501	002	359.870708	–32.169417	RXJ2359.5-3211	3	134	128	PN[1]	Tn1	PFWE	36742	M1[1]	Tn1	PFW	40047	M2[1]	Tn1	PFW	40 250

Table D.2. 2XMM catalogue fields and targets identifications.

Rev	Obsid	N src#	DETID	Fld	Crd	Categ	Prog	RA (prop) [deg]	Dec (prop) [deg]	Target (prop)	RA (Simb) [deg]	Dec (Simb) [deg]	Type (Simb)	Name (Simb)	RA (XSA) [deg]	Dec (XSA) [deg]
0088	0125310101	–	–	1	s	IV	Cal	0.124999	–25.125000	Abell 2690	0.05729	–25.18653	ClG	Abell 2690	0.122750	–25.122639
...																
1009	0302580501	4	246847	s	s	V	Large	359.899999	–32.185083	RXJ2359.5-3211	359.8987	–32.1853	ClG	RX J2359.5-3211	359.913147	–32.170193

EP_EXTENT and *EP_EXTENT_ERR* (E) [arcsec], SAS task `emldetect`: the extent radius (i.e., core radius) and error of a source detected as extended is determined fitting a beta-model profile to the source PSF (Sect. 4.4.4). Anything below 6″ is considered to be a point source and the extent is re-set to zero. To avoid non-converging fitting an upper limit of 80″ has been introduced.

EP_EXTENT_ML (E), SAS task `emldetect`: the extent likelihood is the likelihood of the detection being extended as given by $L_{\rm ext} = -\ln p$, where p is the probability of the extent occurring by chance.

ca_HRn and *ca_HRn_ERR* (E), SAS tasks `emldetect, srcmatch`: the hardness ratios are given for ca = [EP, PN, M1, M2] and n = [1, 2, 3, 4]. They are defined as the ratio between the count rates R in bands n and $n + 1$:

$$\mathrm{HR}n = (R_{n+1} - R_n)/(R_{n+1} + R_n).$$

In the case where the rate in one band is 0.0 (i.e., too faint to be detected in this band) the hardness ratio will be −1 or +1 which is only a lower or upper limit, respectively. In cases where the rate in both bands is zero, the hardness ratio is undefined (NULL).

Errors are the 1σ-error on the hardness ratio.

EPIC hardness ratios are calculated by the SAS task `srcmatch` and are averaged over all three cameras [PN, M1, M2]. Note that no energy conversion factor was used and that the EPIC hardness ratios are de facto not hardness ratios but an equivalent parameter helpful to characterise the hardness of a source.

ca_b_EXP (E) [s], SAS task `emldetect`: the exposure map values are given for combinations of ca = [PN, M1, M2] and b = [1, 2, 3, 4, 5]. They are the PSF-weighted mean of the area of the sub-images (r = 60″) in the individual-band exposure maps (cf. Sect. 4.4).

ca_b_BG (E) [count/pixel], SAS task `emldetect`: the background map values are given for combinations of ca = [PN, M1, M2] and b = [1, 2, 3, 4, 5]; they are derived from the background maps at the given detection position. Note that the source fitting routine uses the background map itself rather than the single value given here. The value is (nearly) zero if the detection position lies outside the FOV.

ca_b_VIG (E), SAS task `emldetect`: the vignetting values are given for combinations of ca = [PN, M1, M2] and b = [1, 2, 3, 4, 5]. They are a function of energy band and off-axis angle. Note that the source parametrisation uses the vignetted exposure maps instead.

ca_ONTIME (E) [s]: the ontime values, given for ca = [PN, M1, M2], are the total good exposure time (after GTI filtering) of the CCD where the detection is positioned. Note that some source positions fall into CCD gaps or outside of the detector and will have therefore a NULL given.

ca_OFFAX (E) [arcmin], SAS task `emldetect`: the off-axis angles, given for ca = [PN, M1, M2], are the distance between the detection position and the on-axis[32] position on the respective detector; the off-axis angle for a camera can be greater than 15′ when the detection is located outside the FOV of that camera.

ca_MASKFRAC (E), SAS task `emldetect`: the maskfrac values, given for ca = [PN, M1, M2], are the PSF weighted mean of the detector coverage of the detection. It depends slightly on energy; only band 8 values are given here which are the minimum of the energy-dependent maskfrac values. Sources which have less than 0.15 of their PSF covered by the detector are considered as being not detected.

DIST_NN (E) [arcsec], SAS task `emldetect`: the distance to the nearest neighbouring detection; note that there is an internal threshold of 6″ (before positional fitting) for splitting a source into two.

D.5. Detection flags

This section lists quality flags as well as flags for the presence of time-series or spectra for a detection. There are 7 columns in this section.

SUM_FLAG (J): The summary flag of the source is derived from the EPIC flag EP_FLAG as explained in detail in Sect. 7.5. They are:

0 = good;
1 = source parameters may be affected;
2 = possibly spurious;
3 = located in an area where spurious detection may occur;
4 = located in an area where spurious detection may occur and possibly spurious.

EP_FLAG (12A), SAS task `dpssflag`: EPIC flag that combines the flags in each camera [PN_FLAG, M1_FLAG, M2_FLAG], that is, a flag is set in EP_FLAG if at least one of the camera-dependent flags is set.

PN_FLAG (12A), SAS task `dpssflag`: PN flag made of the flags [1−12] (counted from left to right) for the PN source detection. A flag is set to True according to the conditions summarised in Sect. 7.3 for the automatic flags and Sect. 7.4 for the manual flags. In cases where the camera was not used in the source detection a dash is given. In cases where a source was not detected

[32] This is the optical axis which is close to but not the same as the geometrical centre of the detector.

by this camera the flags are all set to False (default). Flag [10] is not used.

M1_FLAG (12A), SAS task `dpssflag`: same as PN_FLAG but for M1.

M2_FLAG (12A), SAS task `dpssflag`: same as PN_FLAG but for M2.

TSERIES (L): the flag is set to True if this source has a time-series made in at least one exposure (Sect. 5).

SPECTRA (L): the flag is set to True if this source has a spectrum made in at least one exposure (Sect. 5).

D.6. Variability information

This section lists 7 columns with variability information for those detections for which time-series were extracted.

EP_CHI2PROB (E): the minimum value of the available camera probabilities [PN_CHI2PROB, M1_CHI2PROB, M2_CHI2PROB].

PN_CHI2PROB (E), SAS task `ekstest`: the χ^2-probability (based on the null hypothesis) that the source as detected by the PN camera is constant. The Pearson's approximation to χ^2 for Poissonian data was used, in which the model is used as the estimator of its own variance (Sect. 5.2). If more than one exposure (that is, time-series) is available for this source the lowest value of probability was used.

M1_CHI2PROB (E), SAS task `ekstest`: same as PN_CHI2PROB but for M1.

M2_CHI2PROB (E), SAS task `ekstest`: same as PN_CHI2PROB but for M2.

VAR_FLAG (L): the flag is set to True if this source was detected as variable, that is, EPIC χ^2-probability $<10^{-5}$ (see EP_CHI2PROB).

VAR_EXP_ID (4A): if the source was detected as variable (that is, if VAR_FLAG is set to True), the exposure ID ("S" or "U" followed by a three-digit number) of the exposure with the lowest χ^2-probability is given here.

VAR_INST_ID (2A): if the source was detected as variable (that is, if VAR_FLAG is set to True), the instrument ID [PN, M1, M2] of the exposure given in VAR_EXP_ID is listed here.

D.7. Unique source parameters

This section lists 31 columns with combined parameters for the unique sources (using the prefix "SC") together with the total number of detections per source. For a detailed description on how the detections are matched see Sect. 8.1.

SC_RA (D) [deg]: the mean right ascension in degrees (J2000) of all the detections of the source SRCID (see RA) weighted by the positional errors POSERR.

SC_DEC (D) [deg]: the mean declination in degrees (J2000) of all the detections of the source SRCID (see Dec) weighted by the positional errors POSERR.

SC_POSERR (E) [arcsec]: the error of the weighted mean position given in SC_RA and SC_DEC in arcseconds.

SC_EP_b_FLUX and (E) [erg cm^{-2} s^{-1}]: the mean band b flux of all the detections of the source SRCID (see EP_b_FLUX) weighted by the errors (EP_b_FLUX_ERR), where b = [1, 2, 3, 4, 5, 8, 9].

SC_EP_b_FLUX_ERR (E) [erg cm^{-2} s^{-1}]: error on the weighted mean band b flux in SC_EP_b_FLUX, where b = [1, 2, 3, 4, 5, 8, 9].

SC_HRn (E): the mean hardness ratio of the bands n and $n + 1$ of all the detections of the source SRCID (see EP_HRn) weighted by the errors (see EP_HRn_ERR), where n = [1, 2, 3, 4].

SC_HRn_ERR (E): error on the weighted mean hardness ratio in SC_HRn.

SC_DET_ML (E): the total-band detection likelihood of the source SRCID is the maximum of the likelihoods of all detections of this source (see EP_8_DET_ML).

SC_EXT_ML (E): the total-band detection likelihood of the extended source SRCID is the average of the extent likelihoods of all detections of this source (see EP_EXTENT_ML).

SC_CHI2PROB (E): the χ^2-probability (based on the null hypothesis) that the unique source SRCID as detected by any of the observations is constant, that is, the minimum value of the EPIC probabilities in each detection (see EP_CHI2PROB) is given.

SC_VAR_FLAG (L): the variability flag for the unique source SRCID is set to VAR_FLAG of the most variable detection of this source.

SC_SUM_FLAG (J): the summary flag for the unique source SRCID is taken to be the maximum flag of all detections of this source (see SUM_FLAG).

N_DETECTIONS (J): the number of detections of the unique source SRCID used to derive the combined values.

References

Abazajian, K., Adelman-McCarthy, J. K., Agüeros, M. A., et al. 2005, AJ, 129, 1755 (SDSS-DR3)

Arviset, C., Barbarisi, I., Bini, G., et al. 2007, in Astronomical Data Analysis Software and Systems XVI, ESA Science Archives, 703

Baldi, A., Molendi, S., Comastri, A., et al. 2002, ApJ, 564, 190

Barcons, X., Carrera, F. J., Watson, M. G., et al. 2002, A&A, 382, 522

Barcons, X., Carrera, F. J., Ceballos, M. T., et al. 2007, A&A, 476, 1191

Becker, R. H., Helfand, D. J., White, R. L., Gregg, M. D., & Laurent-Muehleisen, S. A. 1997, ApJ, 475, 479 (FIRST)

Bonnarel, F., Fernique, P., Bienaymé, O., et al. 2000, A&AS, 143, 33

Briggs, K. R., & Pye, J. P. 2003, MNRAS, 345, 714

Brunner, H., Cappelluti, N., Hasinger, G., et al. 2008, A&A, 479, 283

Caccianiga, A., Severgnini, P., Della Ceca, R., et al. 2007, A&A, 470, 557

Caccianiga, A., Severgnini, P., Della Ceca, R., et al. 2008, A&A, 477, 735

Cappelluti, N., Hasinger, G., Brusa, M., et al. 2007, ApJS, 172, 341

Carrera, F. J., Ebrero, J., Mateos, S., et al. 2007, A&A, 469, 27

Cash, W. 1979, ApJ, 228, 939

Cocchia, F., Fiore, F., Vignali, C., et al. 2007, A&A, 466, 31

Condon, J. J., Cotton, W. D., Greisen, E. W., et al. 1998, AJ, 115, 1693 (NVSS)

Cutri, R. M., Skrutskie, M. F., Van Dyk, S., et al. 2003, University of Massachusetts and Infrared Processing and Analysis Center (IPAC/California Institute of Technology), The 2MASS All-Sky Catalog of Point Sources (2MASS)

De Breuck, C., Tang, Y., de Bruyn, A. G., Rottgering, H., & van Breugel, W. 2002, A&A, 394, 59 (WISH)

Della Ceca, R., Maccacaro, T., Caccianiga, A., et al. 2004, A&A, 428, 383

Della Ceca, R., Caccianiga, A., Severgnini, P., et al. 2008, A&A, in press [arXiv:0805.1919]

den Herder, J. W., Brinkman, A. C., Kahn, S. M., et al. 2001, A&A, 365, L7

The DENIS consortium 2005, Third release of DENIS data (DENIS)

Dietrich, J. P., Miralles, J.-M., Olsen, L. F., et al. 2006, A&A, 449, 837

Dorman, B., & Arnaud, K. A. 2001, Astronomical Data Analysis Software and Systems X, ed. F. R. Harnden, Jr., F. A. Primini, & H. E. Payne, 238, 415

Ebrero, J., Carrera, F. J., Page, M. J., et al. 2008, A&A, 493, 55

Ehle, M., Breitfellner, M., Díaz Trigo, M., et al. 2007, XMM-Newton Users' Handbook, http://xmm.esac.esa.int/external/xmm_user_support/documentation/uhb/XMM_UHB.html

Fabbiano, G., Evans, I., Evans, J., et al. 2007, in Astronomical Data Analysis Software and Systems XVI, ed. R. A. Shaw, F. H., & D. J. Bell, ASP Conf. Ser., 376 (San Francisco: ASP), 172

Farrell, S., Villa-Pascual, D., Rodriguez, J., Webb, N., & Barret, D. 2008, A&A, in preparation

Georgakakis, A., Nandra, K., Laird, E. S., Aird, J., & Trichas, M. 2008, MNRAS, 388, 1205

Gioia, I. M., Maccacaro, T., Schild, R. E., et al. 1990, ApJS, 72, 567

Gorski, K. M., Hivon, E., Banday, A. J., et al. 2005, ApJ, 622, 759
Harris, D. E., Forman, W, Gioa, I. M., et al. 1994, EINSTEIN Observatory catalog of IPC X-ray sources, SAO HEAD CD-ROM Series I (Einstein), Nos 18−36, (2E)
Hasinger, G., Altieri, B., Arnaud, M., et al. 2001, A&A, 365, L45
Hasinger, G., Cappelluti, N., Brunner, H., et al. 2007, ApJS, 172, 29
Ibarra, I., Matt, G., Guainazzi, M., et al. 2007, A&A, 465, 501
Jansen, F., Lumb, D., Altieri, B., et al. 2001, A&A, 365, L1
Joint *IRAS* Science Working Group 1988, *IRAS* Point Source Catalog, Version 2 (Washington: US Govt. Printing Office) (IRAS PSC)
Jones, C., & Forman, W. 1984, ApJ, 276, 38
Joye, W. A., & Mandel, E. 2003, in Astronomical Data Analysis Software and Systems XII, ed. H. E. Payne, R. I. Jedrzejewski, & R. N. Hook, ASP Conf. Ser., 295 (San Francisco: ASP), 489
Kim, D.-W., Cameron, R. A., Drake, J. J., et al. 2004, ApJS, 150, 19
Kotov, O., Trudolyubov, S., & Vestrand, W. T. 2006, ApJ, 641, 756
Krumpe, M., Lamer, G., Schwope, A. D., et al. 2007, A&A466, 41
Loaring, N. S., Dwelly, T., Page, M. J., et al. 2005, MNRAS, 362, 1371
Lopez-Santiago, J., Micela, G., Sciortino, S., et al. 2007, A&A463, L165
Lumb, D. 2000, XMM-PS-TN-40, http://xmm2.esac.esa.int/docs/documents/CAL-TN-0001-1-0.ps.gz
Mason, K. O., Breeveld, A., Much, R., et al. 2001, å, 365, L36
Mateos, S., Barcons, X., Carrera, F. J., et al. 2005, A&A, 433, 855
Mateos, S., Warwick, R. S, Carrera, F. J., et al. 2008, A&A, in press
McMahon, R. G., Irwin, M. J., & Maddox, S. J. 2000, The APM-North Catalogue, (Cambridge: Institute of Astronomy) (APM-North)
Monet, D., Bird, A., Canzian, B., et al. 1998, U.S. Naval Observatory Flagstaff Station (USNOFS) and Universities Space Research Association (USRA) stationed at USNOFS (USNO-A2.0)
Monet, D. G., Levine, S. E., Casian, B., et al. 2003, AJ, 125, 984 (USNO-B1.0)
Moshir, M., Copan, G., Conrow, T., et al. 1990, IRAS Faint Source Catalog, $|b| > 10$ Degrees, Version 2.0, Infrared Processing and Analysis Center (IRAS FSC)
Motch, C., Barcons, X., Carrera, F., et al. 2002, in New Visions of the X-ray Universe in the XMM-Newton and Chandra Era [arXiv:astro-ph/0203025]
Ochsenbein, F., Bauer, P., & Marcout, J. 2000, A&AS, 143, 221 (VizieR)
Page, M. J., Lehmann, I., Boller, T., et al. 2007, MNRAS, 378, 1335
Park, T., Kashyap, V. L., Siemiginowska, A., et al. 2006, ApJ, 652, 610
Pierre, M., Chiappetti, L., Pacaud, F., et al. 2007, MNRAS, 382, 279
Protassov, R., van Dyk, D. A., Connors, A., Kashyap, V. L., & Siemiginowska, A. 2002, ApJ, 571, 545
ROSAT Scientific Team 2000, The ROSAT Source Catalog of Pointed Observations with the High Resolution Imager (1RXH) (3rd Release), ROSAT NEWS No. 71 (HRI)
ROSAT Consortium 2000, The Second ROSAT Source Catalog of Pointed Observations, ROSAT News 72, 25-May-2000 (PSPC)
Schneider, D. P., Hall, P. B., Richards, G. T., et al. 2007, AJ, 134, 102
Schwope, A., Hasinger, G., Lehmann, I., et al. 2000, Astron. Nachr., 321, 1 (RBS)
Schwope, A. D., Lamer, G., Burke, D., et al. 2004, Adv. Space Res., 34, 2604
Severgnini, P., Caccianiga, A., Braito, V., et al. 2003, A&A406, 483
Space Telescope Science Institute (STScI) and Osservatorio Astronomico di Torino 2001, The Guide Star Catalogue, Version 2.2.01 (GSC 2.2)
Stocke, J. T., Morris, S. L., Gioia, I. M., et al. 1991, ApJS, 76, 813
Streblyanska, A., Bergeron, J., Brunner, H., et al. 2004, Nucl. Phys. B Proc. Suppl., 132, 232
Strüder, L., Briel, U., Dennerl, K., et al. 2001, A&A, 365, L18
Stuhlinger, M., Altieri, B., Esquej, M. P., et al. 2006, XMM-SOC-CAL-TN-0052 (issue 5.0)
Turner, M. J. L., Abbey, A., Arnaud, M., et al. 2001, A&A, 365, L27
Ueda, Y., Ishisaki, Y., Takahashi, T., Makishima, K., & Ohashi, T. 2005, ApJS, 161, 185
Ueda, Y., Watson, M. G., Stewart, I. M., et al. 2008, ApJS, in press [arXiv:0806.2846]
Vogel, J., Byckling, K., Schwope, A., et al. 2008, A&A, in press
Voges, W., Aschenbach, B., Boller, T., et al. 1999, A&A, 349, 389 (RASS)
Voges, W., Aschenbach, B., Boller, T., et al. 2000, IAU Circ., 7432, 1 (RASS-FSC)
Watson, M. G. 2003, Astronomical Data Analysis Software and Systems XII, 295, 107
Watson, M. G., Auguères, J.-L., Ballet, J., et al. 2001, A&A, 365, L51
Watson, M. G., Pye, J. P., Denby, M., et al. 2003, Astron. Nachr., 324, 89
Wenger, M., Ochsenbein, F., Egret, D., et al. 2000, A&AS, 143, 9
White, N. E., Giommi, P., & Angelini, L. 1994, IAUC, 6100
White, N. E., Giommi, P., & Angelini, L. 2000, The WGACAT version of the ROSAT PSPC Catalogue, Rev. 1 (Greenbelt: LHEA/NASA) (WGACAT)
XMM-Newton Survey Science Centre Consortium 2003, The XMM-Newton Serendipitous Source Catalogue, Version 1.0.1 (Leicester: XMM-SSC) (1XMM)
XMM-Newton Survey Science Centre Consortium 2006, The Second XMM-Newton Serendipitous Source Pre-release Catalogue, (Leicester: XMM-SSC) (2XMMp)
Yuan, W., McMahon, R. G., Watson, M., et al. 2003, Astron. Nachr., 324, 178